Impact of Compressive Force on Macrophages and Cementoblasts and the Possible Interrelation with Orthodontically Induced Inflammatory Root Resorption

Inaugural Dissertation

submitted to the

Faculty of Medicine

in partial fulfillment of the requirements

for the Ph.D. degree

of the Faculties of Veterinary Medicine and Medicine

of the Justus Liebig University Giessen

by

Yao Wang

Giessen (2025)

From the Medical Center for Dentistry and Oro-Maxillofacial Medicine,

Department of Orthodontics

Director: Univ.-Prof. Dr. Sabine Ruf

of the Faculty of Medicine of the Justus Liebig University Giessen

First Supervisor and Committee Member: Prof. Dr. Sabine Ruf

Co-Supervisor: Priv.-Doz. Dr. Sabine Groeger

Second Supervisor and Committee Member: Prof. Dr. Carsten Staszyk

Committee Member (Chair): Prof. Dr. Ross G. Douglas

Committee Member: Prof. Dr. Ross G. Douglas, Prof. Dr. Sabine Ruf,
Prof. Dr. Carsten Staszyk, Prof. Dr. Dr. Till Köhne

Date of Doctoral Defense: 02. Dec. 2025

Lists of Contents

1. List of Tables

2. List of Figures

3. Abbreviations

ALP	Alkaline Phosphatase
AMB	Ameloblastin
AMG	Amelogenin
ANGPT1; *Angpt1*	Angiopoietin1
ANGPTL4; *Angptl4*	Angiopoietin-like 4
APOE; *ApoE*	Apolipoprotein E
ARG1; *Arg1*	Arginase 1
BET	Bromodomain and Extraterminal Domain
BRD	Bromodomain
BSP	Bone Sialoprotein
CCK-8	Cell Counting Kit-8
CF	Compressive Force
Cq	Cycle Threshold Value
CTS	Cyclic Tensile Strain
DC	Degree Centrality
DEGs	Differentially Expressed Genes
DMSO	Dimethyl Sulfoxide
DNA	Deoxyribonucleic Acid
DSP	Dentin sialoprotein
EARR	External Apical Root Resorption
EIR	External Inflammatory Resorption
FBS	Fetal Bovine Serum
GEO	Gene Expression Omnibus
GO	Gene Ontology
GPCR	G protein-coupled receptor
GSEA	Gene Set Enrichment Analysis
H3ac	H3 Acetylation
HBSS	Hanks' Balanced Salt Solution
HRP	Horseradish Peroxidase
IF	Immunofluorescence
IFN	Interferon
IL-10; *Il10*	Interleukin-10
IL-1A	Interleukin 1-alpha
IL-1α	Interleukin-1α
IL-1β; *Il1b*	Interleukin-1β
IL-6; *Il6*	Interleukin 6
IL1RN	Interleukin 1 Receptor Antagonist
INM	Inner Nuclear Membrane
iNOS; *Nos2*	Inducible Nitric Oxide Synthase
IRF4	Interferon Regulatory Factor 4
KASH	Klarsicht/ANC-1/Syne-1 Homology

KEGG	Kyoto Encyclopedia of Genes and Genomes
LATS1/2	Large Tumor Suppressor Kinase 1/2
limma	Linear Models for Microarray
LINC	Linker of Nucleoskeleton and Cytoskeleton
LMCD1	LIM and Cysteine-rich Domains 1
NC	Negative Control
NE	Nuclear Envelope
NGS	Next Generation Sequencing
NL	Nucleolus
NLS	Nuclear Localization Signal
NP	Nucleoplasm
NPC	Nuclear Pore Complex
ns	Not Significant
OIIRR	Orthodontically Induced Inflammatory Root Resorption
OPG	Osteoprotegerin
OPN	Osteopontin
OTM	Orthodontic Tooth Movement
PBS	phosphate-buffered saline
PDL	Periodontal Ligament
PDLCs	Periodontal Ligament Cells
POSTN	Periostin
PPIs	Protein-Protein Interactions
PTMs	Post-Translational Modifications
qRT-PCR	Quantitative Real-Time Reverse Transcriptase-Polymerase Chain Reaction
RANKL	Receptor Activator for Nuclear Factor κ B Ligand
RNA	Ribonucleic Acid
ROI	Region of Interest
RT	Room Temperature
SAA3; *Saa3*	Serum Amyloid A3
SBS	Sequencing Technology by Synthesis
SD	Standard Deviation
SOD	Superoxide Dismutase
sR LMNA	siRNA-resistant *LMNA* Mutant
SUN	Sad1/UNC-84
SV40	Simian Virus 40
TBE	Tris/Borate/EDTA
TEA	Tetraethylammonium
TEM	Transmission Electron Microscopy

TGF-β	Transforming Growth Factor-β
TMA	Tetramethylammonium
TNF-α	Tumor Necrosis Factor-α
TRAP	Tartrate-resistant Acid Phosphatase
TRPM2	Transient Receptor Potential Melastatin 2
YAP1	Yes-associated Protein 1
γH2Ax	Phosphorylated H2A Histone Family Member X

4. Introduction

4.1 Orthodontic Tooth Movement (OTM)

Orthodontic tooth movement (OTM) refers to a complicated remodeling of biological tissue in the dentoalveolar complex [1]. This process is fundamentally based on the bone's ability to remodel in response to mechanical forces. Specifically, when an orthodontic force is applied to a tooth, the side opposite to the direction of the force—referred to as the 'compressive side'—experiences compression against the alveolar bone, leading to bone resorption. In contrast, the 'tensile side', located opposite to the compressive side, experiences tension that stimulates bone formation. This dynamic remodeling enables teeth to gradually shift within the alveolar bone.

In force-induced bone remodeling, inflammation plays a crucial role [2]. The periodontal ligament (PDL), a fibrous structure connecting the cementum to the alveolar bone, anchors the tooth within its socket. When orthodontic force is applied, the PDL and capillaries on the compressive side are compressed [3]. This reduces oxygen tension, triggering increased anaerobic respiration within periodontal ligament cells (PDLCs). These changes in the chemical microenvironment trigger the production of inflammatory mediators—including cytokines, prostaglandins, and leukotrienes—which subsequently drive osteoclast differentiation and bone resorption [4, 5]. Research indicates that modulation of these inflammatory cytokines can significantly impact the distance and rate of OTM [6]. Hence, a deeper understanding of this molecular process is crucial to optimize orthodontic outcomes and minimize potential complications.

4.2 Orthodontically Induced Inflammatory Root Resorption (OIIRR)

The cementum-covered tooth root is less susceptible to mechanical stress than the alveolar bone, which helps protect the tooth root from remodeling under pressure.

However, when excessive orthodontic force leads to complete capillary occlusion and ischemic necrosis in the periodontal ligament, it can subsequently cause cementum resorption. Severe loss of cementum may then expose the underlying dentin to clastic cells. This triggers a common orthodontic complication known as OIIRR [7]. Severe cases of OIIRR may cause significant tooth root shortening or even tooth loss. Since a severe OIIRR is irreversible, the primary clinical approach is to focus on prevention and halting disease progression.

Notably, slight OIIRR is inevitable for all orthodontic patients [1, 8]. Generally, minor cementum resorption typically does not lead to any radiological or clinical symptoms and can only be detected through high resolution imaging or histopathological examination [8, 9]. Unlike enamel and dentin, cementum has an active repair capacity and cementoblasts are able to continuously repair the cementum to maintain a dynamic equilibrium (Figure 1), limiting the progression of root resorption [10]. Thus, cementoblasts are regarded as the first line of defense against OIIRR. However, in some cases, the rate of cementum destruction can exceed the rate of repair, disrupting the dynamic equilibrium of cementum and ultimately leading to severe OIIRR.

The mechanisms underlying the cementum hemostasis in OIIRR remain poorly understood. One possible contributing factor is an excessive inflammatory response. For example, necrotic root canals can induce periapical periodontitis, leading to a similar form of root resorption known as external inflammatory resorption (EIR) [11]. Mechanistically, the presence of pro-inflammatory cells has been shown to correlate positively with OIIRR severity in a rat model [12]. Additionally, polymorphisms in specific inflammatory genes, such as interleukin 1 receptor antagonist (IL1RN), interleukin-1α (IL-1α), interleukin-1β (IL-1β), and interleukin 6 (IL-6), have been associated with variations in OIIRR severity [13].

Another important factor is mechanical compressive force. Excessive or prolonged orthodontic force significantly increases the risk for OIIRR [14]. Multiple studies have shown that mechanical force influences various cellular functions in cementoblasts, including migration, autophagy, and mineralization [15, 16]. However, comprehensive insights into the effects of orthodontic force on cementoblasts are still scarce. Furthermore, effective therapeutic targets to reverse the functional damage caused by mechanical force on cementoblasts—especially with respect to their mineralization function—have yet to be identified.

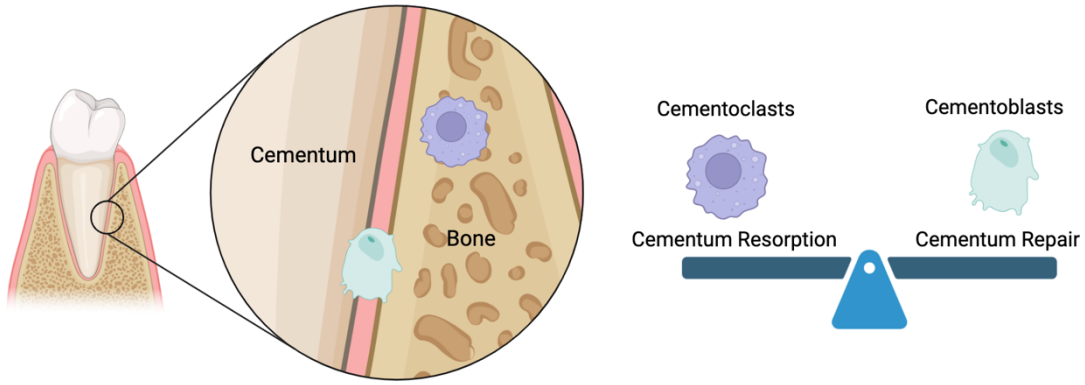

Figure 1. *Schematic diagram displays cementum homeostasis in a physiological state. Cementoblasts maintain a dynamic equilibrium of cementum. Disruption of this equilibrium can lead to irreversible cementum destruction, exposing the underlying fragile dentin to clastic cells, ultimately resulting in OIIRR.*

4.3 Macrophages in OIIRR

Conventional theory regarded PDLCs as the primary mechanical effectors of orthodontic force, converting mechanical stimuli into an inflammatory microenvironment that regulates alveolar bone and cementum resorption [17-19].

However, the behaviours of immune cells under orthodontic compressive forces have long been neglected.

Macrophages, a critical component of the innate immune system, are found in nearly every tissue of the body [20]. Initially identified and characterized by Elie Metchnikoff in the 19th century for their roles in phagocytosis and microbial killing, macrophages are now recognized for their diverse, context-dependent functions across various physiological and pathophysiological conditions [21]. Macrophages are recognized as mechanically sensitive cells and have been shown to respond to various mechanical stimuli, including cyclic tensile force [22], compression[23], spatial confinement [24], and matrix stiffness [25]. This mechanical activation of macrophages is crucial in a range of physiological and pathological processes, such as cancer [26], steatohepatitis [27], orthodontic tooth movement [28], osteogenesis [29], pulmonary inflammation [30], and atherosclerosis [31]. In OTM, macrophages play a central role in regulating inflammation, contributing to local pH reduction and bone demineralization to create attachment sites for osteoclasts [32]. Additionally, inflammatory cytokines secreted by macrophages modulate the microenvironment, influencing osteoclast and osteoblast activity and thus impacting bone remodeling [33]. However, the role of macrophages in cementogenesis and OIIRR remains unclear.

Macrophages can differentiate into distinct phenotypes in response to various stimuli, including pathogenic microorganisms, inflammatory signals, cytokines, and certain physicochemical factors. The phenotypes, mechanisms, and roles associated with macrophage polarization are summarized in Table 1 [34]. This heterogeneity allows macrophages to play diverse roles in bone remodeling. Broadly, macrophage polarization is categorized into two main phenotypes: the classically activated M1 and the alternatively activated M2 [35]. M1 macrophages, often termed pro-inflammatory, secrete high levels of cytokines such as IL-1β, inducible nitric oxide synthase (iNOS),

and tumor necrosis factor-α (TNF-α), which support M1's role in osteoclast activation and bone resorption [36-38]. In contrast, M2 macrophages, known for their anti-inflammatory function, produce mediators including interleukin-10 (IL-10), transforming growth factor-β (TGF-β), and arginase 1 (ARG1), which promote osteoclast differentiation and inhibit osteogenesis [36, 37, 39, 40].

When OIIRR occurs, an increased proportion of M1 to M2 macrophages in periodontal tissue has been observed [12, 41]. The positive correlation between pro-inflammatory polarization and OIIRR indicates that macrophage-targeted immune regulation may serve as a therapeutic approach.

Exogenous anti-inflammatory drugs are often associated with significant side effects and systemic immunosuppression. Their lack of target specificity can interfere with natural tissue repair and increase the risk of infections. Moreover, long-term use may lead to tolerance, requiring higher doses and exacerbating adverse effects. Adiponectin, an endogenous cytokine secreted by adipose tissue, is markedly reduced in the circulation of obese individuals compared to that of non-obese subjects [42]. It has been proven to promote M2 polarization and reduced systemic inflammation [43, 44]. It has attracted attention in the field of orthodontics because orthodontic outcomes in obese individuals are often suboptimal, an *in vivo* experiment based on rats has reported that it can slow the rate of orthodontic tooth movement by acting on bone remodeling [45]. However, whether adiponectin can suppress mechanoresponses of macrophage remains unclear, and its influence on cementum is also unknown. This study aims to investigate the potential of adiponectin as an immune regulator for the treatment of OIIRR.

Table 1. *The phenotypes, mechanisms and functions of macrophage polarization [34].*

Macrophage phenotypes		Stimulus	Specific markers	Cytokines	Mechanisms	Functions
M1		LPS, IFN-γ, GM-CSF	CD80, CD86, CD16/32, MHCII, iNOS	IL-1β, IL-6, IL-12, IL-23, TNF-α, CXCL1~3, CXCL8~10, CCL2~5, CCL11	TLR4/NF-κB, IRF5, JAK/STAT1, Notch	Antigen presentation, Th1 immune reaction, proinflammation, pathogen elimination, anti-tumor
M2	M2a	IL-4, IL-13	CD206, MHCII, IL-1R, Dectin-1	Arg1, IL-10, TGF-β, CCL17, CCL22	JAK/STAT6, c-Myc, IRF4	Anti-inflammation, wound healing, Th2 immune response, anaphylaxis, fibrosis
	M2b	LPS, IC	CD206, MHCII, CD86	IL-10, IL-1β, IL-6, TNF-α, IL-12^{low}	TLR4, Syk, PI3K	Immune regulation, pro-tumor, promoting infection
	M2c	IL-10, TGF-β, glucocorticoid	CD206, CD163	IL-10, TGF-β, Arg-1, CXCL13	JAK/STAT3, NF-κB, TGF-β/Smads	Phagocytosis, immunosuppression, tissue remodeling
	M2d	TLR agonist, $A_{2A}R$ ligand	CD206	IL-10, VEGF, IL-12^{low}, TNF-α^{low}	TLR4, NF-κB	Pro-tumor, angiogenesis
M4		CXCL4	MMP7^{+}S100A8^{+}, CD206, CD163$^{+/-}$	TNF-α, CCL18	N/A	Proinflammation, low phagocytosis
Mox		QxPAPC	HO-1, Srxn1, Gclc, Gclm,Txnrd1, Nurr1, Trb3, COX-2	IL-1β, VEGF	Nrf2, Keap1, TLR2	Low chemotaxis and phagocytosis
M(Hb)		Hemoglobin	CD206, CD163	IL-10, IL-1R antagonist	PI3K/AKT, LXRα	Cholesterol loading resistance, ATP-binding cassette transporter up-regulation

4.4 Cementoblasts in OIIRR

Due to their similar ability to biomineralize, cementoblasts and osteoblasts are often compared. However, cementoblasts represent a unique phenotype rather than a subpopulation of osteoblasts. Cementoblasts have a distinct cellular origin from osteoblasts, and the cementum they produce is morphologically, functionally, and biochemically different from any type of bone [46]. Despite these differences, both osteoblasts and cementoblasts can respond to similar regulatory factors. For example, vitamin D deficiency leads to increased bone sialoprotein (BSP) gene expression and decreased osteopontin (OPN) gene expression in both cell types [47]. This suggests that cementoblasts likely possess regulatory mechanisms for biomineralization that are highly similar to those observed in osteoblasts.

The precise mechanisms underlying the failure of cementoblasts-mediated repair in OIIRR remain unclear. However, it is generally attributed to inappropriate orthodontic force. We propose two potential mechanisms of injury.

The first proposed mechanism involves a disruption of the damage-repair balance due to excessive inflammatory responses. Linares et al. (2017) have summarized the molecular pathways regulating external apical root resorption (EARR) taking place without orthodontic force, highlighting the key role of macrophages in these pathways

(Figure 2) [48]. In this model, M2 macrophages can activate cementoblasts and initiate cementum repair by reducing inflammation. Therefore, the interactions between macrophages and cementoblasts in the OIIRR are one of the foci of this study.

Another potential mechanism is the direct impact of mechanical stimulation on cementoblasts function, which also constitutes a major focus of the present study. Recent research has shown that compressive force can inhibit migration [16] and mineralization [15]. Our study provides a comprehensive analysis of the effects of compressive force on cementoblasts through RNA sequencing and further investigates the molecular mechanisms underlying the transduction of mechanical signals in cells, a process known as mechanotransduction.

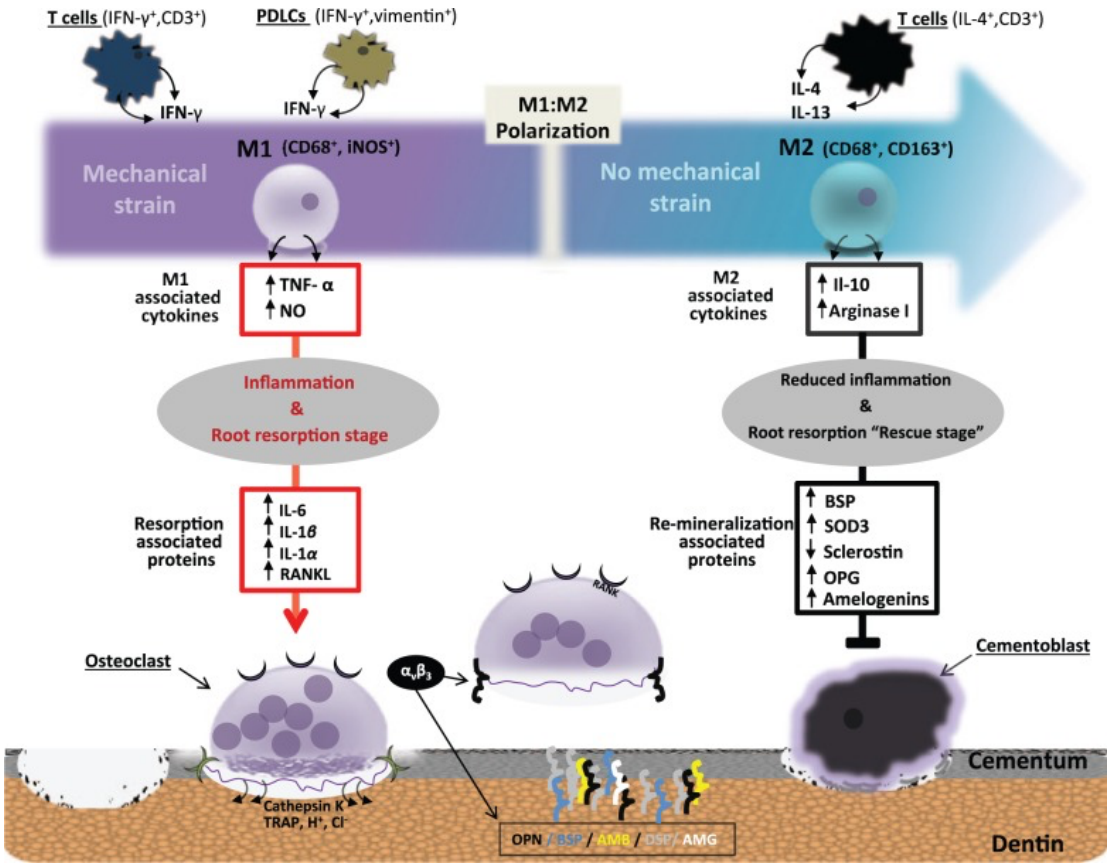

Figure 2. *Schematic graphic illuminates the critical influence of macrophages on the root resorption process [48].*

Remarkable plasticity can be observed in the switch from M1 to M2 polarization states, depending on the conditions in the cellular microenvironment, by secreting several proinflammatory cytokines. M1: CD68^{+}, inducible nitric oxide synthase–positive (iNOS^{+}) macrophages. M2: CD68^{+}, CD163^{+} type 2 macrophages. PDLCs, periodontal ligament cells; IFN, interferon; TNF, tumor necrosis factor; NO, nitric oxid; IL, interleukin; BSP, bone sialoprotein; SOD, superoxide dismutase; OPG, osteoprotegerin; AMB, ameloblastin; DSP, dentin sialoprotein; AMG, amelogenin; OPN, osteopontin; TRAP, tartrate-resistant acid phosphatase; RANKL, receptor activator for nuclear factor κ B ligand.

4.5 Mechanotransduction

All life forms sense and respond to mechanical stimuli. Throughout evolution, organisms develop diverse mechanotransduction pathways, leading to fast and sustained mechanoresponses [49]. Mechanical forces can spread quite rapidly over considerable distances through the cellular structure, compared to diffusible biochemical molecules which move slowly and dissipate significantly as the distance increases [50]. Investigating mechanotransduction is essential for understanding how cells—and even entire organisms—alter their behavior in response to external mechanical stimuli. However, this goal is challenging to achieve due to the complexity of mechanosensation, which involves various effectors and signaling pathways. This study primarily focused on three distinct mechanical effectors under compressive force and their roles in OIIRR: chromatin, lamin A/C and Piezo1.

4.5.1 Chromatin

The primary route of mechanotransduction in single cells is the mechanoreceptor - cytoskeleton direct force transduction pathway (e.g., integrins), permitting straight spreading of forces all the way into the nucleus [49]. Recent studies confirmed that chromatin structure alteration is a common feature of cellular mechanoresponse. This structure alteration can affect gene transcription [51], cellular mechanical property alteration [52, 53], mitosis [54] and DNA damage [55].

The nucleosome serves as the fundamental unit of chromatin, comprising a core histone octamer (with two molecules each, of histones H2A, H2B, H3, and H4) around which approximately 1.75 left-handed superhelical turns of DNA wrapped around [56]. These histones are extensively modified by post-translational modifications (PTMs), commonly referred to as epigenetic marks, that play a crucial role in regulating chromatin structure and thus various DNA-templated processes. Recently, PTMs have been suggested to encode memory and plasticity in response to

mechanical stimuli [49]. For example, a study from 2021 revealed that histone H3 acetylation is inhibited by exposure to a rough matrix, another type of mechanical stimulus [57]. The acetylated form of histone H3 (H3ac) can be recognized by bromodomain (BRD) proteins, which then modulate transcription of target genes.

Based on these insights, we hypothesized that H3ac is a key mediator linking orthodontic compressive forces to inflammation in periodontal tissue. In other words, orthodontic compression may modulate H3 histone acetylation, thereby promoting macrophage polarization.

4.5.2 Lamin A/C

The nuclear lamina, a protein network approximately 15 nanometers thick located beneath the inner surface of the nuclear envelope, consists of four distinct types of intermediate filaments in mammalian cells: lamin A, B1, B2 and C [58-60]. Lamin A and its splice variant lamin C, both encoded by the *LMNA* gene, have high similarities in their primary sequences, so they have mostly been studied together as lamin A/C [61]. Lamin A/C interacts with transcription factors, the nuclear pore complex (NPC), and chromatin, and is believed to be associated with nuclear stiffness, cellular migration, and differentiation [62, 63]. Recently, lamin A/C was found to respond to mechanical stimulation [63-65]. Specifically, lamin A/C is linked to the cytoskeleton and responds to external mechanical cues, such as shear force or extracellular matrix stiffness, which can affect lamin A/C protein levels or molecular conformation [66]. Clinically, deficient lamin A/C is linked to various pathological changes, including premature aging, cardiomyopathy, lipodystrophy, muscular dystrophy, microcephaly, epilepsy, mandibuloacral dysplasia type A and axonal peripheral neuropathy [67, 68]. These observations suggest that lamin A/C plays a role in cellular mechanotransduction and related diseases. However, the function of lamin A/C in mechanotransduction under hydrostatic compression—a type of mechanical stimulus

commonly found in tissues such as bones, muscles, the bladder, the eye, and periodontal ligaments—remains unclear.

Lamin A/C connects to the cytoskeleton *via* the linker of nucleoskeleton and cytoskeleton (LINC) complex [63, 69]. The LINC complex is a protein complex expressed on the nuclear envelope, consisting of outer nuclear membrane Klarsicht/ANC-1/Syne-1 homology (KASH) domain proteins (such as nesprin family members) and inner nuclear membrane Sad1/UNC-84 (SUN) domain proteins (such as SUN1 and SUN2) [70]. The N-terminus of KASH domain proteins interacts with cytoskeleton [70]. SUN proteins are anchored in the INM by at least one transmembrane segment, exposing their N termini to the nucleoplasm and connecting with nuclear binding partners [71]. Taking SUN2 as an example, the SUN2 protein trimer passes through the inner nuclear membrane and is connected to the nuclear lamina *via* a mechanosensitive domain [72]. Through this physical connection, lamin A/C can directly receive external mechanical signals. Additionally, lamin A/C also interfaces with chromatin, participating in diverse cell signaling pathways that influence essential cellular processes such as proliferation, migration, genome organization, and DNA repair [66]. Hence, we hypothesized that lamin A/C mediates macrophage mechanotransduction as a nuclear mechanical sensor, bridging external mechanical stimuli with gene transcription.

4.5.3 Piezo1

Another significant pathway of mechanotransduction involves mechanoreceptor-coupled biochemical secondary messenger systems. Mechanoreceptors, a diverse group of structures on the surface of cells that respond to mechanical stimuli, including various ion channels [73], integrins [74], cadherins [75], G protein-coupled receptor (GPCR) [76] and cilia [77]. Among these, ion channels are the most common mechanoreceptors in mammalian cells. Upon activation, these mechanically gated

channels allow ions to flow into/out of the cell, triggering downstream biochemical signaling cascades by altering membrane potential or introducing specific ions, such as Ca^{2+}, as second messengers [78].

The Piezo family of mechanosensitive ion channels was discovered in 2010 [79]. Piezo1 is the most well-known member in the family, previously known as FAM38A, that is broadly expressed in various tissues, especially those that are highly exposed to mechanical stimuli, such as the colon, kidneys, skin, bladder and lungs [79] and, in particular, endothelial cells in blood vessels [80]. Piezo1 is a homotrimer with a structure resembling a three-bladed propeller, featuring a central pore. The mechanosensitive domain of Piezo1 is embedded within the cell membrane. When mechanical force is applied to the membrane, this domain can directly sense membrane curvature and tension, converting the mechanical force into conformational changes in the protein's central pore, thus opening the channel. Opened channel allows the transmembrane transport of cations such as K^+, Na^+, Cs^+, Ca^{2+}, Ba^{2+}, Mg^{2+}, Tetramethylammonium (TMA), and Tetraethylammonium (TEA) [81, 82].

The role of Piezo1 in regulating bone homeostasis has been clearly demonstrated. In osteoblastic cells, Piezo1 deficiency results in reduced bone mass and spontaneous fractures, along with increased bone resorption in mouse models [83, 84]. Furthermore, Piezo1 has been shown to play a role in periodontal tissue response to orthodontic forces, where blocking Piezo1 reduces the osteogenesis-promoting capacity of periodontal ligament cells [85]. To date, only one study has suggested that Piezo1 mediates the inhibition of cementum formation under compressive force *in vitro* (2017), though it did not reveal any specific signaling pathways [86]. Based on this, we hypothesize that compressive force acts on Piezo1 to influence cementoblasts functions and aimed to elucidate the downstream mechanisms of Piezo1 in this process.

5. Aims of the Study

Previous research has shown that macrophages can respond to mechanical stimuli, and some indirect evidence has hinted towards their involvement in OIIRR. We hypothesize that orthodontic compressive force may induce macrophages to polarize into a pro-inflammatory phenotype, thereby inhibiting the mineralization of cementoblasts. Additionally, we proposed that compressive force may directly reduce cementogenesis. This study also investigated the underlying mechanotransduction mechanisms in both macrophages and cementoblasts.

Specifically, this study aimed to investigate:

1) the effects of orthodontic compressive force on macrophage functions, including polarization, cytokines, proliferation and migration
2) the effects of adiponectin on mechanically activated macrophages
3) the roles of Histone H3 acetylation in the mechanotransduction of macrophages
4) the roles of Lamin A/C in the mechanotransduction of macrophages
5) the effects of mechanically activated macrophages in cementoblasts
6) the effects of orthodontic compressive force on cementoblastic functions, including hypoxia, mineralization and migration
7) the roles of Piezo1 in mechanically impaired cementoblasts
8) the downstream signaling pathways of Piezo1

6. Methods and Materials

6.1 Materials

6.1.1 Chemical/Reagents

All the chemicals listed in Table 2 were purchased from the named companies. The application of assays listed below are described in the corresponding methods part.

Table 2. *Chemicals/Reagents*

Items	Supplier
Cell Culture Medium	DMEM, high glucose (Thermo Fisher Scientific, USA) DMEM, high glucose, no calcium (Thermo Fisher Scientific, USA)
FBS (Fetal Bovine Serum)	Fetal Bovine Serum (FBS) with low Endotoxin (Gibco, USA)
PBS Buffer	Phosphate Buffered Saline (PBS) Dulbecco without Ca^{2+} and Mg^{2+} (Gibco, USA)
Antibiotics	Penicillin/Streptomycin 10,000 U/mL (Gibco, USA)
RIPA Buffer	Protein Lysis Buffer (Thermo Fisher Scientific, USA)
Osteogenic Differentiation Kit	Osteogenic Differentiation Kit (MUXX90021, Cyagen, China)
Protease Inhibitor	Protease Inhibitor Cocktail (Thermo Fisher Scientific, USA)
CCK-8 Kit	Cell Counting Kit-8 (MedChemExpress, USA)
SDS-PAGE	Mini-PROTEAN® TGX™ Gels (Bio-Rad, USA)
Protein Molecular Weight Marker	PageRuler™ Prestained Protein Ladder (Thermo Fisher Scientific, USA)
Western Blot Transfer	Trans-Blot® Turbo™ Transfer Pack (Bio-Rad, USA)

Blocking Buffer	5% Non-Fat Milk (Carl Roth, Germany)
Washing Buffer	1× Tris-Buffered Saline, 0.1% Tween®-20 (TBS-T) (Sigma-Aldrich, USA)
Western Blot Stripping Buffer	Restore™ PLUS Western Blot Stripping Buffer (Thermo Fisher Scientific, USA)
β-Mercaptoethanol	β-Mercaptoethanol Purity ≥99.0% (Sigma-Aldrich, USA)
qRT-PCR Supermix	DyNamo Flash SYBR Green qPCR Kit (Thermo Fisher Scientific, USA)
PCR Primers	Synthesis by Qiagen (Qiagen, Germany)
PCR DNase/RNase-Free Water	Invitrogen Distilled Nuclease-Free Water (Thermo Fisher Scientific, USA)
Ethanol	Ethanol (Carl Roth, Germany)
Tween-20	Tween-20 (Sigma-Aldrich, USA)
Triton X-100	0.1% Triton™ X-100 (Sigma-Aldrich, USA)
Alizarin Red S Staining Solution	1% Alizarin Red S Solution (Sigma-Aldrich, USA)
Transfection Reagent	HiPerFect® Transfection Reagent (Qiagen, Germany)
DMSO	Dimethyl Sulfoxide for Molecular Biology, Purity ≥99.9% (Sigma-Aldrich, USA)
Laemmli Sample Buffer	4× Laemmli Sample Buffer (Bio-Rad, USA)
Fluorescent Mounting Medium	Fluorescent Mounting Medium with DAPI (Abcam, UK)
GSMTX4	GSMTX4 (Sigma-Aldrich, USA)
Yoda1	Yoda1 (Sigma-Aldrich, USA)
Cytocalasin D	Cytocalasin D (Thermofisher Scientific, USA)
Phallodin	Phallodin-iFlour 488 (Abcam)
I-BET 762	I-BET 762 (Sigma-Aldrich, USA)
Adiponectin	Adiponectin (Sino biological, China)
PI	FxCycle™ PI/RNase Staining Solution (Thermofisher Scientific, USA)
RNA Protector	NucleoProtect RNA Reagent for RNA stabilization

6.1.2 Instruments/Apparatus

All instruments/apparatus used in the study are listed in Table 3.

Table 3. *Technical Apparatus*

Items	Supplier
Sterilization	Systec™ Laboratory Autoclave V-75 (Systec, Germany)
Air-Flow Cell Culture Hoods	Laminar Flow Hood (Thermo Fisher Scientific, USA)
Ultra-pure Water Purification Machine	Elix® Reference Water Purification System (Millipore, USA) ZRX0010WW (Billerica, USA)
Dishwasher	Miele™ Professional Dishwasher G7883 CD (Miele, Germany)
Precision Balance	Denver Instrument SI-234A (Denver Instrument, USA)
CO_2 Cell Culture Incubator	HERAcell 150i CO2 Incubator (Thermo Fisher Scientific, USA)
Water Bath	GFL® Water Bath (GFL, Germany)
Centrifuge	Mikro 200R (Hettich, Germany) Centrifuge 5810 (Eppendorf, Germany) Galaxy MiniStar (VWR, USA)
Micro-plate Reader	96-Well Micro-Plate Reader (BioTek, USA)
Light Microscope	Eclipse LV150N (Nikon, Japan)
Inverted Phase Contrast Fluorescence Microscope	DMI6000 B (Leica Microsystems, Germany)
Confocal Laser Microscope	LSM980 Airyscan 2 (Carl Zeiss, Germany)
Refrigerator	1-4°C Refrigerator (Liebherr, Germany) -20°C Refrigerator (Liebherr, Germany) -80°C Refrigerator (Thermo Fisher Scientific, USA)
Shaker	Vortex-2 Genie (Scientific Industries, USA)
Roller	Roller Mixer SRT6 (Stuart, United Kingdom)

	MAXI HP 1P VARIOMAC® (Thermo Scientific, USA)
Spectrophotometer	NanoDrop 2000 (Thermo Fisher Scientific, USA)
Electrophoresis Chambers	Mini-PROTEAN Tetra Vertical Electrophoresis Cell (Bio-Rad, USA)
	Mini-Sub Cell GT Horizontal Electrophoresis System (Bio-Rad, USA)
Western Blot Transfer System	Trans-Blot® Turbo™ Transfer System (Bio-Rad, USA)
Western Blot Cassettes	Trans-Blot® Turbo™ Cassette (Bio-Rad, USA)
Transmission Electron Microscope	JEM-2100 Transmission Electron Microscope (JEOL, Japan)
Western Blot Imaging System	ChemiDoc Imaging System (Bio-Rad, USA)

6.1.3 Consumables

All consumables used in this study are listed in Table 4.

Table 4. *Consumables*

Items	Supplier
Tips	Eppendorf Biosphere@ Filter Tip: 10 µL, 100 µL,1,000 µL (Sarstedt, Germany)
Cell Counting	Chamber Manual Counting Chamber (Marienfeld, Germany)
Cell Culture Plate	35 mm 6-Well Cell Culture Plate (Greiner Bio-One, Germany) 9 mm 96-Well Cell Culture Plate (Greiner Bio-One, Germany)
Reaction Tubes	1.5 mL Micro Tube (Sarstedt, Germany) 15/50 mL Falcon type centrifuge tube (Sarstedt, Germany)
Syringe	Sterile Injekt@ 10 mL Luer Solo (Braun, Germany)
Syringe Filter	Sterile Syringe Filter 0.45 µm Cellulose Acetate Membrane (VWR, Germany)
Cell Scraper	STERILE CELL SCRAPER 28 CM LONG (Greiner, Bio-One, Germany)
cDNA Tube Multiply@	Multiply@-µStripPro Low Profile (Sarstedt, Germany)
PCR Plate	0.2 mL non-Skirted 96-Well PCR Plate (Scientific Industries, Germany)

6.1.4 Kits

All Kits used in this study are listed in Table 5.

Table 5. *Kits*

Kits	Supplier
Protein Assay Kit	Pierce™ BCA Protein Assay Kit (Thermo Fisher Scientific, USA)
RNA Isolation Kit	NucleoSpin RNA Kit (MACHEREY-NAGEL, Germany)
cDNA Synthesis Kit	Verso cDNA Synthesis Kit (Thermo Fisher Scientific, USA)
Western Blot Membrane	Trans-Blot® Turbo RTA Mini 0.2 µm Nitrocellulose Transfer Kit (Bio-Rad, USA)
Calcium Detection Kit	Calcium Detection Kit (Cell-Based) (Abcam, UK)
H3 Acetylation Detection Kit	Histone H3 Total Acetylation Detection Fast Kit (Colorimetric) (Abcam, UK)
Comet Assay Kit	Comet Assay Kit (3-well slides) (Abcam, UK)
Cell Counting Kit-8	Cell Counting Kit-8 (MedChemExpress, USA)
Live/Dead Viability Assay Kit	Live/Dead Viability Assay Kit (Thermo Fisher Scitific, USA)
Proliferation Assay Kit	Click-iT™ EdU Cell Proliferation Kit for Imaging, Alexa Fluor™ 488 dye (Thermo Fisher Scientific, USA)
Phagocyte Assay Kit	Vybrant™ Phagocytosis Assay Kit (Thermo Fisher Scientific, USA)
Clarity Western ECL Substrate	Clarity Western ECL Substrate Kit (Bio-Rad, USA)
Alkaline Phosphatase Staining Kit	Blue-Color Alkaline Phosphatase Staining Kit (BioCat, Germany)
Transfection Reagent	HiPerFect® Transfection Reagent (Qiagen, Germany)

6.1.5 Software

All digital software applications used in this study are listed in Table 6.

Table 6. *Software*

Applications	Software and Company
Visualization and Statistical Analysis	Prism 10.0 (Graphpad, USA)
Image Analysis System	Leica Application Suite LASV4.8 (Leica, Germany) Zen lite (Zeiss, Germany) Image J Software (NIH, USA)
References Management	EndNote X9 (Thomson Reuters, USA)
Western Blot Analysis	Image Lab (Bio-Rad, USA)
Figure Management	Microsoft Office (Microsoft, USA)

6.1.6 qRT-PCR Primers

All primers used for qRT-PCR in this study are listed in Table 7.

Table 7. *qRT-PCR Primers*

Primers (Qiagen)	Catalog number
IL-1β	QT01048355
ARG1	QT00134288
IL-10	QT00106169
INOS	QT01547980
Actin-β	QT0095242
OPG	QT00106757
RUNX2	QT00102193
SAA3	QT00249823
APOE	QT01043889
SP7	QT00293181
OPN	QT02524536
LMNA	QT00102193
HIF-1α	QT01039542
VEGF	QT00160769
ANGPT1	QT00166859
ANGPTL4	QT00139748
LMCD1	QT00150731
POSTN	QT00150759
PIEZO1	QT01560216
SUN1	QT00139223
SUN2	QT00138530

6.1.7 Antibodies

All antibodies used in this study are listed in Table 8.

Table 8. *Antibodies*

Primary Antibodies	Company	Catalog number
LMCD1	Invitrogen	PA5-49414
YAP1	Abcam	ab56701
Activated YAP1	Abcam	ab205270
POSTN	Abcam	ab92460
HIF-1α	Abcam	ab51608
γH2AX	Abcam	ab81299
SUN1	Abcam	ab10321
SUN2	Abcam	ab124916
Actin-β	Abcam	ab8227
GAPDH	Sigma	G8795
IRF4	Sigma	SAB4501566
Lamin A/C	Abcam	ab133256

Secondary Antibodies	Company	Catalog number
Goat Anti-rabbit IgG Alexa Fluor594	Abcam	ab150080
Goat Anti-rabbit IgG Alexa Fluor488	Abcam	ab176753
Polyclonal Goat Anti-Rabbit HRP	Dako	P0448
Polyclonal Goat Anti-Mouse HRP	Dako	P0447

6.1.8 siRNAs

All siRNAs used in this study are listed in Table 9.

Table 9. *siRNAs*

Flexitube siRNA (Qiagen)	Catalog number
LMNA	SI01090803
Negative Control	1027280
Death Control	SI04939025

6.2 Methods

6.2.1 Cell Culture

The murine macrophage cell line RAW264.7 was purchased from the ATCC, and the OCCM-30 cementoblasts cell line was kindly provided by Prof. M. Somerman [87] (NIH, NIDCR, Bethesda, MD, USA). Briefly, OCCM-30 cells were isolated from the root surface of the first mandibular molars of osteocalcin-transgenic mice. These mice are engineered to carry the simian virus 40 (SV40) large T-antigen under the control of the osteocalcin promoter. As a result, only cells expressing osteocalcin also express the T-antigen, establishing them as an immortalized cell line [87].

All cells were maintained in DMEM (41965062, Gibco) containing 10% Fetal Bovine Serum (FBS) (10270-106, Gibco) and 1% penicillin/streptomycin (A3160502, Gibco) and incubated in a humidified atmosphere of 5% CO_2 at 37 °C. Generally, the medium was changed twice a week.

For passaging, the cells were seeded into 6-well plates (657160, Greiner Bio-One).) at a density of 3×10^4 cells / well until confluence.

6.2.2 Cell Harvesting

For harvesting RAW 264.7 cells, they were washed twice with 1× phosphate-buffered saline (PBS). Fresh complete medium was added to the flask or plate, and the cells were detached by gently scraping with a plastic scraper. The resulting suspension was carefully collected.

For OCCM-30 cell harvesting, the cells were washed twice with 1× PBS and then treated with trypsin. After a 5-minute incubation at 37°C, the detached cells were diluted with warm growth medium and centrifuged at 1,000 rpm for 3 minutes. The supernatant was carefully removed, and the pellet was resuspended in the appropriate liquid to obtain the cell suspension.

6.2.3 Cell Freezing and Thawing

For cell freezing, OCCM-30 cells were washed twice with 1× PBS and treated with trypsin. After a 5-minute incubation at 37°C, the detached cells were diluted with warm growth medium, centrifuged at 1,000 rpm for 3 minutes, and the supernatant was carefully removed. The concentrated cell pellet was then resuspended in freshly prepared freezing medium (90% complete medium and 10% dimethyl sulfoxide (DMSO)) and stored at -20°C for 1 hour before being transferred to -80°C for long-term storage.

To thaw the frozen cells, the vial was quickly transferred to a 37°C water bath and incubated for 1 minute. The cells were then suspended in fresh, pre-warmed medium, centrifuged to remove the DMSO-containing supernatant, and plated in fresh growth medium for further cultivation.

6.2.4 Reagents Solution Preparation

Mouse adiponectin was purchased from Sino Biological Inc. (50636-M08H) with a purity higher than 95% (determined by SDS-PAGE). It was dissolved in RNase-free water to obtain a stock solution of 1 mg/mL.

The histone acetylation inhibitor I-BET 762, Piezo1 inhibitor GSMTX4, and Piezo1 activator Yoda1 were purchased from Sigma-Aldrich (SML1272, SML-3140, and SML-1558, respectively). Cytochalasin D was purchased from Thermo Fisher Scientific (PHZ1063). All compounds were dissolved in DMSO to prepare stock solutions at a concentration of 1 mg/mL.

6.2.5 Compressive Force Loading

The cells were seeded into 6-well plates (657160, Greiner Bio-one) at the density of 1×10^6 cells / well 24 h before compressive force loading. The contactless force-loading appliance utilized has been described in our previous publication [88].

Briefly, a floating weight was placed on the medium to subject macrophages to 1 g/cm^2 hydrostatic pressure. Cells were harvested by a scraper to operate further analysis (Figure 3).

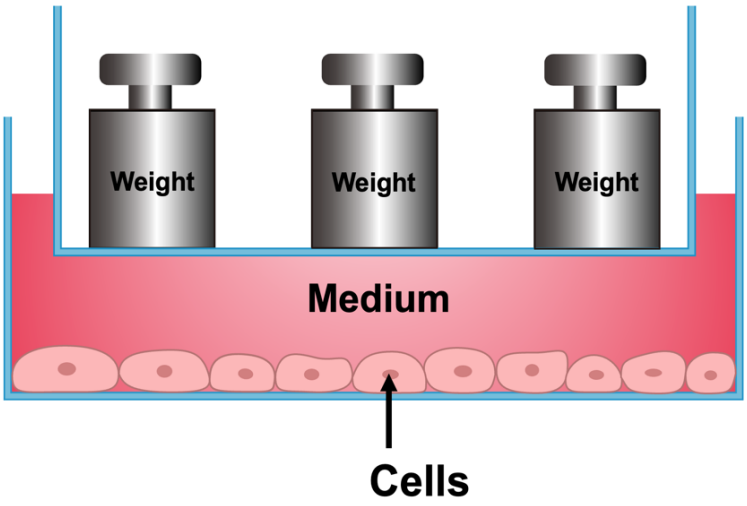

Figure 3. *Schematic diagram illustrates the model used for hydrostatic compressive force.*

A weight and its container, represented as a 'ship,' float on the medium, applying compressive force to the cells in the form of hydrostatic pressure.

6.2.6 Scratch Assay

Cells were respectively plated in 6-well plates and cultured at density of 1× 10^6 cells per well. Cells were preincubated for 12 h in starvation medium and wounded by scratching using a 100 µL tip. Through this, a cell-free area was created in the center of the cell layer. Afterwards, all non-adherent cells were washed with 1× PBS (10010023, Thermo-Fisher). Photographs of the wounded area were taken immediately after wounding and after setting the timepoints following scratching. The wounded cell layers were photographed at ×10 magnification (DMI6000 B, Leica) and the wound closure area between the cell layer borders was analyzed and

calculated over time using the Image J software (National Institutes of Health and University of Wisconsin, United States).

6.2.7 Identification of Differentially Expressed Genes (DEGs) and Protein-Protein Interaction (PPI) Analysis based on Macrophages Public Dataset

The gene expression profile data of GSE186185 was downloaded from the Gene Expression Omnibus (GEO) in NCBI (http://www.ncbi.nlm.nih.gov/geo/) based on the platform of GPL17021 Illumina HiSeq 2500 (Mus musculus). This database includes transcriptomes of alveolar macrophage samples after force application in a mouse model of tooth movement and without force application (control). The downloaded profile had been preprocessed which was carried out with background correction, log2 transformation in R (4.1.0). The differentially expressed genes (DEGs) in case samples were screened compared with control samples using the Linear Models for Microarray data (limma) package in R. Threshold for the DEGs were set as p-value <0.01 and |log2 FC (fold change) | ≥ 1. The STRING database demonstrates known and predicted protein-protein interactions (PPIs) from interaction sources, including text mining, experiments, databases, co-expression, neighborhood, gene fusion, and co-occurrence. 28 DEGs were mapped to the STRING, selected the medium confidence (0.4) as the minimum required interaction score, hid disconnected nodes in the network, and set other parameters as default.

6.2.8 RNA-seq and PPI Network Analysis of Cementoblasts

The total RNA was isolated using the ReliaPrep™ RNA Miniprep Systems (z6011, Promega). RNA concentrations were measured at 260 nm using a spectrophotometer (Nanodrop2000, Thermo Scientific). The quantity and quality of the RNA samples were assessed by 1% agarose gel electrophoresis to test RNA degradation and potential contamination, and by Bioanalyzer (Agilent 5400, Agilent), to test sample

purity, quantitation and integrity. Messenger RNA was purified from total RNA using poly-T oligo-attached magnetic beads. After fragmentation, the first strand cDNA was synthesized using random hexamer primers followed by the second strand cDNA synthesis. The library was ready after end repair, A-tailing, adapter ligation, size selection, amplification, and purification. The library preparation kit used is Novogene property (PT042) for 250~300 bp insert cDNA library.

The library quality was checked with Qubit 2.0 and real-time PCR for quantification and bioanalyzer for size distribution detection. The qualified libraries were sequenced by Next Generation Sequencing (NGS) based on Illumina's Sequencing Technology by Synthesis (SBS) - detection by fluorescence of the nucleotide added during the synthesis of the complementary chain - and in a parallelized and massive way. The Novaseq X Plus sequencing system was used to sequence the libraries. The strategy was paired-end 150bp (PE150), data amount 9 G raw data per sample.

All statistical analyses were conducted using the R statistical programming language (R Foundation for Statistical Computing). Genes with an adjusted p-value of < 0.05 found by DESeq2 were considered differentially expressed. DEGs were defined as having $|\log_2\text{FoldChange}| > 0$ and p-value < 0.05. Gene Ontology (GO) enrichment analysis and Kyoto Encyclopedia of Genes and Genomes (KEGG) pathway analysis were performed using the clusterProfiler R package v4.0 (R Foundation for Statistical Computing). Gene set enrichment analysis (GSEA) was performed using all normalized probes on the ‘curated gene set’ and ‘GO gene set’ collections of the Molecular Signatures Database v5.2 (MSigDB).17.

The PPI network analysis of all DEGs was performed using STRING 12.0 database (https://string-db.org/), with minimum required interaction score ≥0.7. The PPI network was further visualized using Cytoscape (3.10.2). Topological analysis of target genes was performed using the NetworkAnalyzer plug-in and CytoNCA plug-in of Cytoscape. The protein nodes were sequenced according to degree centrality (DC).

6.2.9 Transmission Electron Microscopy (TEM) Analysis

Each of the fixed and concentrated cell suspensions (3 µl) was high-pressure frozen (Wohlwend HPF Compact 02) and freeze-substituted (AFS2, Leica). A medium based on acetone, containing 0.25% osmium tetroxide, 0.2% uranyl acetate, and 5% ddH_2O, was used. All samples were freeze-substituted according to the following protocol: -90°C for 22 hours, from -90 °C to -60 °C over 1 hour, -60 °C for 8 hours, from -60°C to -30°C over 1 hour, -30°C for 8 hours, and from -30°C to 0 °C over 1 hour. At 0 °C, samples were washed three times with acetone before a 1:1 mixture of Epon 812 substitute resin (Fluka) and acetone was applied at room temperature for 2 hours. The 1:1 mixture was substituted with a 2:1 mixture overnight, followed by fresh pure resin the next day for 2 hours to impregnate the samples. After another substitution with fresh Epon, samples were polymerized at 60°C for 2 days. The polymerized Epon blocks were then trimmed with razor blades and cut into 50 nm ultrathin sections using an ultramicrotome (UC7, Leica) and a diamond knife (Diatome). Sections were applied onto 100 mesh copper grids coated with pioloform. For additional contrast, mounted sections (labeled or unlabeled) were post-stained with 2% uranyl acetate for 20-30 minutes and subsequently with lead citrate for another 1-2 minutes. The sections were finally analyzed and imaged using a JEOL JEM-2100 transmission electron microscope operated at 120 kV and equipped with a TVIPS 2k x 2k F214 fast-scan CCD camera.

6.2.10 Click-iT® EdU Proliferating Assay

The proliferation assay was conducted using the Click-iT® EdU Flow Cytometry Assay Kit (C10425, Thermo Fisher) according to the manufacturer's instructions. Briefly, cells were seeded into 6-well plates at a density of 2×10^5 cells per well. Following a 2-hour incubation with Click-iT® EdU, cells were harvested, resuspended in PBS containing 1% BSA, and subsequently fixed and permeabilized. The cells

were then incubated with the Click-iT® reaction cocktail for 30 minutes at room temperature, shielded from light. Finally, cell proliferation was assessed on a flow cytometer (BD Biosciences, USA), and data analysis was performed using FlowJo software (TreeStar, USA).

6.2.11 Cell Viability Assay

Cell viability was assessed using the Cell Counting Kit-8 (CCK-8) assay according to the manufacturer's instructions (HY-K0301, MedChemExpress). Briefly, cells were seeded onto glass slides in 6-well plates at a density of 3×10^5 cells per well and adhered overnight. The cells were then treated with compressive force of 1 g/cm², and the glass slides with the cells were subsequently transferred into 96-well plates. Following treatment, 10 μL of CCK-8 solution was added to each well, and the plates were incubated at 37°C for 1–4 hours. Absorbance was measured at 450 nm using a microplate reader. The relative cell viability was calculated as a percentage of the control group.

6.2.12 Small Interfering RNA Oligonucleotides

The siRNAs targeting mouse *LMNA* (the gene coding lamin A/C) (SI01090803), negative control (NC) siRNA (1027280) and cell death control (SI04939025) were purchased from QIAGEN (Germany). Transfection mixture was formulated of 1.2 μL *siLMNA* oligonucleotides, 12 μL HiPerFect@ Transfection Reagent (301705, QIAGEN) and 100 μL serum-free medium. The mixed solution was incubated at room temperature (RT) for 10 min before being added to 2.3 mL complete medium in the 6-well plate. Meanwhile, cells were seeded in the density of 6×10^5 cells/well. At least 24 hours after transfection, 1 g/cm^2 compressive force was loaded as stimulus.

6.2.13 Plasmid Construction and Transfection

A custom-synthesized siRNA-resistant mutated LMNA gene (sR *LMNA*) was obtained from Invitrogen, which was inserted into the vector pcDNA3.1+ Hygro_A069 downstream of the CMV promoter. To confer resistance to siRNA designed to target the wild-type LMNA sequence, 'TTCCCACCGAAGTTCACCCTAAAG', a synonymous mutation—replacing this sequence with 'TTTCCCCCCAAATTTACATTAAAA'—was introduced in the siRNA target region and verified *via* Sanger sequencing. The plasmid DNA was purified from transformed bacteria and concentration determined by UV spectroscopy. The final construct was verified by sequencing.

6.2.14 RNA Extraction

Cells were seeded into 6-well plates at a density of 1×10^6 cells/well and incubated overnight before treatment with stimuli.

To extract total RNA, the cell culture medium was aspirated, and an equal amount of PBS was added to wash the cells. The PBS then was aspirated. Next, cells were incubated with 500 µL RNA protector（740400.250, Macherey-Nagel) for an appropriate amount of time to detach them from the surface of the dish. After cell detachment, cell culture medium was added, and the cells were transferred to a tube. The cells were then pelleted by centrifugation for 10 minutes at 5000 rpm. The supernatant was removed, and lysis buffer was added to the cell pellet. 350 µL of Buffer LBP was added per sample, and the sample was disrupted. The NucleoSpin® gDNA removal column was placed in a collection tube, and the homogenized lysate was transferred to the NucleoSpin® gDNA removal column. The sample was then centrifuged for 30 seconds at 11,000 × g. 100 µL of binding solution was added to the flowthrough, and the mixture was well mixed by moderate vortexing or by pipetting up and down several times. The whole lysate (~450 µL) was transferred to the

NucleoSpin® RNA Plus column, which was preassembled with a collection tube. The sample was then centrifuged for 15 seconds at 11,000 × g. 200 µL of buffer WB1 was added to the NucleoSpin® RNA Plus Column, and the sample was centrifuged for 15 seconds at 11,000 × g. The flowthrough was discarded along with the collection tube, and the column was placed into a new 2 mL collection tube.

600 µL of Buffer WB2 was added to the NucleoSpin® RNA Plus Column, and the sample was centrifuged for 15 seconds at 11,000 × g. The flowthrough was discarded, and the column was placed back into the collection tube. 250 µL of Buffer WB2 was added to the NucleoSpin® RNA Plus Column, and the sample was centrifuged for 2 minutes at 11,000 × g to dry the membrane completely. The column was then placed into a nuclease-free collection tube. 30 µL of RNase-free H_2O was added, and the sample was centrifuged at 11,000 × g for 1 minute and collected.

6.2.15 Quality and Quantification of Total RNA

To prevent potential contamination, standard precautions were strictly followed for all steps and equipment. For example, the working area was cleaned with RNaseZap® RNase Decontamination Wipes (AM9786, Life Technologies), and RNase/DNase-free tubes and water were used throughout the process.

RNA concentrations were measured using a spectrophotometer (NanoDrop 2000, Thermo Fisher Scientific). The quality and quantity of the RNA were evaluated based on spectrophotometric readings. The A260/280 ratio ranged from 2.0 to 2.2, and the A260/230 ratio was approximately 2.0, indicating that the isolated RNA was free from polyphenols, polysaccharides, and protein contaminants.

6.2.16 Complementary DNA (cDNA) synthesis

For synthesis of cDNA, 1.0 µg RNA was transcribed using commercial Verso cDNA Synthesis Kit (AB1453B, Thermo Fisher). The mRNA sample was mixed with

Rnase-free water to achieve 11 µL. Next, 4 µL of 5X cDNA synthesis buffer, 2 µL of dNTP Mix, 1 µL RNA Primer, 1 µL of RT Enhancer and 1 µL of Verso Enzyme Mix were added to each reaction mix and the resulting final volume of 20 µL solution was incubated at 42℃ for 30 minutes, 95℃ for 2 minutes. Further, each sample was diluted with Rnase-free water to achieve 320 µL

6.2.17 Quantitative Real-Time Reverse Transcriptase-Polymerase Chain Reaction (qRT-PCR)

The DyNAmo Flash SYBR Green qPCR Kit (Thermo Fisher Scientific, USA) was used in each reaction setup. The primers employed has been listed in table 7. β-Actin was used as housekeeping gene. Each reaction contained 8 µL cDNA template, 10 µL qPCR master mix and 2 µL primers. Reaction conditions included 40 cycles repeat and were denatured initially for 15 seconds at 95°C, subsequently, each cycling stage was performed at 95°C for 15 seconds and 1 minute of amplification at 60°C. The cycle threshold value (Cq) for each individual PCR product was calculated by the Bio-Rad CFX Manager 3.1 software. Relative levels of transcript expression were quantified using the 2ΔΔCt method.

6.2.18 Protein Extraction and Western Blotting Analysis

RIPA buffer (89901, Thermo Scientific) supplemented with 3% protease inhibitor (78442, Thermo Scientific) was used for the protein extraction. Protein concentrations were measured using PierceTM BCA Protein Assay Kit (23225, Thermo Scientific) on a direct reading Spectrophotometer (DR/2000, HACH). Further, 20 µg protein samples were separated by electrophoresis using 10% SDS-PAGE gel and transferred onto a nitrocellulose membrane (1704271, Bio-Rad). The membranes were blocked with 5% non-fat milk (T145.1, ROTH) in 4 ℃ for 24 h and incubated with the primary antibodies (listed in Table 8) at a concentration of 1:1,000. The used

secondary antibodies were: Polyclonal Goat Anti-Rabbit Horseradish Peroxidase (HRP) (P0448, Dako) and Polyclonal Goat Anti-Mouse HRP (P0447, Dako) in a concentration of 1:2000. The band signals were detected with ChemiDoc Imaging System (Bio-Rad) utilizing Clarity Western ECL Substrate (170-5061, Bio-Rad).

6.2.19 H3 Histone Global Acetylation Levels

Macrophage were plated in 6-well plates (1.0×10^6 cells/well) and treated with 1 g/cm^2 as previously described. After 24 h, all adherent cells were harvested. The acetylation level detection was performed using the Histone H3 Total Acetylation Detection Fast Kit (ab115124, Abcam), purchased from Abcam. Samples were prepared, quantified and assayed according to the manufacturer's protocol. Finally, the obtained yellow color was read on a microplate reader at 450 nm within 2–15 min.

6.2.20 Live Cell Assay

A live cell assay was performed using the LIVE/DEAD™ Viability/Cytotoxicity Assay Kit (L32250, Thermo Fisher). Live cells were identified by their intrinsic intracellular esterase activity, indicated by the enzymatic conversion of nearly non-fluorescent, cell-permeable Calcein AM into intensely fluorescent calcein. This compound is effectively retained within live cells, resulting in uniform and intense green fluorescence. The experimental procedures were conducted according to the manufacturer's instructions. Briefly, cells were plated in a 6-well plate at a density of 1×10^5 cells per well 12 hours prior to mechanical stimulation. After applying the force, Calcein AM was added to the medium, and the cells were incubated for 30 minutes at room temperature. Subsequently, the cells were examined using an inverted phase contrast fluorescence microscope (DMI6000 B, Leica)

6.2.21 Phagocytosis Assay

Phagocytosis was assessed using the Vybrant™ Phagocytosis Assay Kit (V6694, Thermo Fisher Scientific) according to the manufacturer's instructions. Cells were seeded in a 6-well plate at a density of 1×10^5 cells per well and incubated overnight. Fluorescent *E. coli* BioParticles were prepared by suspending them in Hanks' Balanced Salt Solution (HBSS) and sonicating for homogeneity. Following the desired stimulation, the BioParticles were added to the wells. After a 1-hour incubation at 37°C, the wells were washed to remove any non-internalized particles. To quench extracellular fluorescence, 100 µL of trypan blue was added. Fluorescence intensity was analyzed using an inverted phase contrast fluorescence microscope (DMI6000 B, Leica) and quantified with ImageJ software (National Institutes of Health and University of Wisconsin, United States).

6.2.22 Comet Assay

The comet assay was performed following the manual of the comet assay kit (ab238544, Abcam). Briefly, cells were prepared as single cell suspensions and combined with agarose at 37 ℃. The agarose/cells mixture was pipetted onto a glass slide. After the samples were solidified, they were treated with lysis buffer and alkaline solution included in the kit. Electrophoresis was performed via Tris/Borate/EDTA (TBE) electrophoresis (10.8 g Tris Base, 5.5 g Boric Acid, 0.93g EDTA disodium salt and adjust volume to 1L with DI H_2O) at 2 volt/cm for 15 min. Cells were stained with DNA dye provided in the kit for 15 min and viewed by a confocal laser microscope (LSM980 Airyscan 2, Carl Zeiss) using FITC filter.

6.2.23 Evaluation of Nuclear Permeability

The evaluation method is modified from the protocol reported by Raices and Angelo [89]. The protocol is briefly described as follows: the macrophages were seeded together with the *siLMNA* into the 6-well plate. After 24 h, cells were rinsed with cold PBS for 2min and incubated with buffer A (20 mM HEPES pH 7.5, 110 mM KOAc, 5 mM MgCl2, 0.25 M sucrose, and protease inhibitors.) for 5 min on the ice. After then, macrophages were incubated with buffer B (20 μg/mL 500 or 65-80 kDa TRITC-dextran, 20 mM HEPES pH 7.5, 110 mM KOAc, 5 mM sodium chloride, 2 mM $MgCl_2$, 0.25 M sucrose, and protease inhibitors) for 10 min. Cells were rinsed 3 times with cold PBS and mounted by fluorescent Mounting Medium with DAPI (ab104139, Abcam). Finally, the cells were observed under a confocal laser microscope (LSM980 Airyscan 2, Carl Zeiss) with 590 nm (TRITC) or 353 nm (DAPI) laser to evaluate nuclear permeability. For quantification using the Image J software (National Institutes of Health and University of Wisconsin, United States), the DAPI coloring area was selected as the region of interest (ROI), the ratio of dextran integrated density in ROI to entire cells was calculated as the index of permeability.

6.2.24 Immunofluorescence (IF) Staining

Macrophages were fixed with 4% paraformaldehyde (30525-89-4, Sigma- Aldrich) for 15 min at room temperature. Cells were permeabilized using 0.5% Triton X-100 (28313, Thermo-Fisher) for 10 min. Then, cells were blocked in immunofluorescence blocking buffer (12411S, Cell signaling Technology) for 30 min at room temperature and further incubated with primary antibodies at 4°C overnight. The primary antibodies used include lamin A/C (ab133256, Abcam) (dilution 1:100), activated yes-associated protein 1 (YAP1) (ab205270, Abcam) (dilution 1:500), SUN1 (ab103021, Abcam) (dilution 1:200), SUN2 (ab124916, Abcam) (dilution 1:200), phosphorylated H2A histone family member X (γH2AX) (ab81299, Abcam) (dilution

1:250) and Piezo1 (NBP1-78537, NOVUS) (dilution 1:100). The secondary antibodies that were used included goat anti-rabbit IgG H&L Alex Fluor 594® (ab150080, Abcam) or Alexa Fluor® 488 (ab150077, Abcam) After washing with PBS, samples were incubated with phalloidin-iFlour 488 Reagent (ab176753, Abcam). After rinsing with PBS for 3 times, all samples were mounted using a fluorescent mounting medium with DAPI (ab104139, Abcam). The staining was analyzed using a confocal laser microscope (LSM980 Airyscan 2, Carl Zeiss).

6.2.25 Microscope Parameters

All fluorescent images were captured using either an inverted phase contrast fluorescence microscope (DMI6000 B, Leica) with HCX PL FLUOTAR 10×/0.3 and 63×/0.7 dipping lenses, or a confocal laser microscope (LSM980 Airyscan 2, Carl Zeiss) equipped with a Plan Apo 63×/1.4 oil immersion objective. Images were acquired with hybrid detectors configured to the following detection ranges: green, 491–646 nm; red/pink, 578–757 nm; and blue, 426–544 nm. Excitation was provided by a filtered white light source at 493 and 590 nm, and a UV laser at 353 nm.

6.2.26 Nuclear-Cytoplasmic Fractionation Experiment

Cells were grown to approximately 80% confluency and harvested by scratching. The cells were collected by centrifugation at 300 × g for 5 minutes at 4°C. The supernatant was discarded, and the cell pellet was re-suspended in lysis buffer (50 mM Tris-HCl (pH 7.5), 150 mM NaCl, 1 mM EDTA, 1% Trition X-100 and protease inhibitors). The lysate was centrifuged at 600 × g for 10 minutes at 4°C. The nuclear pellet was resuspended in RIPA buffer supplemented with protease inhibitors. The supernatant, containing the cytoplasmic fraction, was carefully collected and mixed with an equal volume of RIPA buffer. Both of them are incubated on ice for 30 minutes and stored at −80°C for further analysis.

6.2.27 ALP Staining

Cementoblasts were placed in density of 1×10^5/well and induced towards osteogenic differentiation using Osteogenic Differentiation Kit (MUXMX-90021, Cyagen) for 5 days. After the induction period, alkaline phosphatase (ALP) activity was assessed using an ALP staining kit (AP100B-1, System Biosciences Innovation) according to the manufacturer's protocol. Briefly, cells were fixed with 4% paraformaldehyde for 10 minutes at room temperature and then washed three times with PBS. ALP substrate solution was added to the cells and incubated at 37°C for 30 minutes. After incubation, the cells were washed with distilled water, and the staining was visualized using a light microscope (DMI6000 B, Leica). The presence of blue precipitates indicated ALP-positive cells. Images were captured at random fields of view to assess the extent of ALP-positive staining.

6.2.28 Alizarin Red S Staining

The cementoblasts were plated in density of 1×10^5 cells/well and treated with Osteogenic Differentiation Kit (MUXMX-90021, Cyagen). At day 14 post-osteogenic induction, the cementoblasts were washed three times with PBS and fixed with 4% paraformaldehyde for 15 minutes at room temperature. Following fixation, cells were washed again with PBS and stained with Alizarin Red S staining (pH 5.2) for 10 minutes at room temperature. After staining, the cells were thoroughly washed with distilled water to remove excess dye. The presence of calcium deposits was observed under an inverted phase-contrast microscope (DMI6000 B, Leica). Images were captured to evaluate the extent of mineralization.

6.2.29 Calcium Detection

Intracellular calcium ion concentration was detected using Calcium Detection Kit (ab284545, Abcam). When cells achieved desired density in 6-well plate, they were

incubated for 45 min at 37°C with fluorescent calcium probe, and 10 min with DAPI (ab104139, Abcam). The cells were observed under fluorescence microscope (DMI6000 B, Leica) with 488 nm wavelength excitation filter.

6.2.30 Statistical Analysis

All experiments were successfully conducted with at least three biological replicates. Statistical analyses were performed using the GraphPad Prism 9.0 software (GraphPad software, La Jolla, CA, USA). All values are expressed as means ± standard deviation (SD) and were analyzed using one-way ANOVA or Student's t-test to determine the statistically significant differences between groups. Differences were considered statistically significant at a p value of <0.05.

7. Results

7.1 Compressive Force Induced Macrophages Nuclear Deformation and Inhibited Proliferation

The macrophages were subjected to a static compressive force of 1 g/cm² for 24 hours and the overall cell morphology did not change according to optical microscope images (Figure 4a). However, under TEM, we observed a substantial increase in shrunken nuclei, yet their nuclear envelopes retained their intact structures (Figure 4c). Additionally, a significant increase in heterochromatin was observed within these cells, tightly adhering to the nuclear envelope (Figure 4c, black arrows). Moreover, we observed vesicles-like structures in the region of heterochromatin (Figure 4c, red arrows), with still unknown specific composition and biological role. These findings support the presumption that chromatin plays a role in mechanotransduction by condensing itself. More importantly, the subnuclear localization of these condensed heterochromatin suggests that the nuclear envelope also responds to compressive force by interacting with heterochromatin. Given the observed vesicles-like structures, we think the response of the nuclear envelope is likely associated with increased nuclear-cytoplasmic transport. Hence, the responses of the nuclear membrane to and its associated structures under compressive force serve as the focus of this study.

Moreover, we found that compressive force significantly inhibits macrophages viability according to the CCK-8 results (Figure 4b). For further investigating the impacts of compressive force on proliferation, we performed an EdU incorporation assay. Cells undergoing proliferation incorporate EdU into their DNA, and can be detected as EdU-positive cells by flow cytometry. After 24 hours of compressive force stimulation, the number of S-phase cells was nearly undetectable, suggesting that compressive force substantially suppresses cell proliferation (Figure 4d).

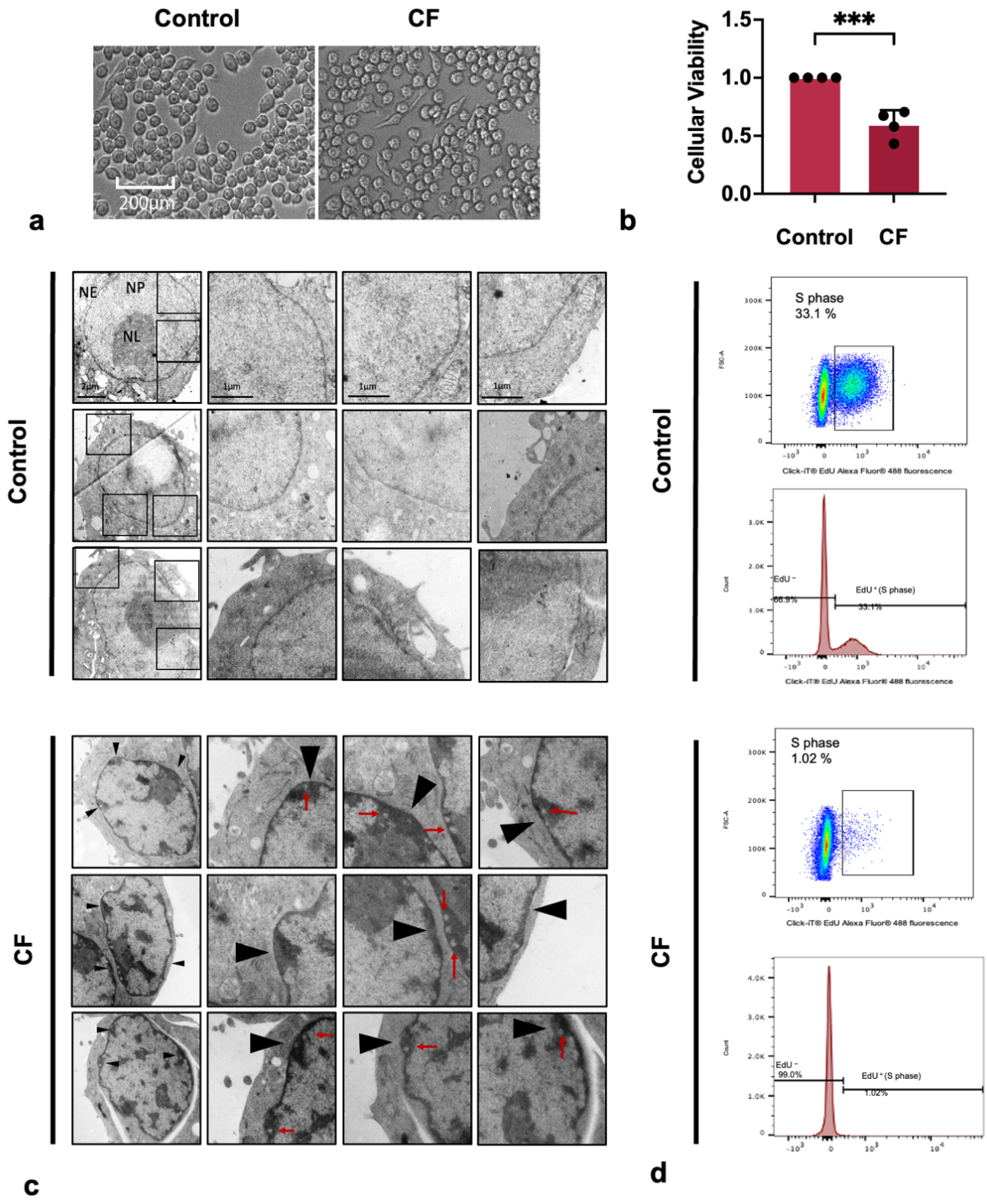

Figure 4. *Compressive force (1 g/cm^2) induced heterochromatin formation and nuclear deformation, as well as inhibited proliferation.*

*(a) The effect of compressive force on the morphology of macrophages was negligible; (b) Compressive force significantly inhibited cellular viability. (c) TEM images showed increased heterochromatin formation within the nucleus after 24 hours, localized along the nuclear envelope. Vesicle-like structures were also observed at the sites of interaction between heterochromatin and the nuclear envelope; (d) Compressive force significantly reduced the proportion of cells in the S phase. Values are expressed as mean ± SD; *** $p < 0.001$. CF: compressive force;*

NE: nuclear envelope; NP: nucleoplasm; NL: nucleolus; black arrows: heterochromatin; red arrows: vesicles.

7.2 Compressive Force Enhanced Polarization Markers of Macrophages

After 1 g/cm^2 compressive force application, inducible nitric oxide synthases (iNOS, *Nos2*), interleukin 1*β* (IL-1*β*, *Il1b*), interleukin 10 (IL-10, *Il10*), and Arginase 1 (ARG1, *Arg1*) were detected by RT-qPCR. All four gene expressions were elevated. However, it is noticeable that *Nos2* was the first marker to respond to mechanical compression, showing an increasing trend at 6 h (Figure 5a). All other markers, *Il1b*, *Arg1*, and *Il10*, were enhanced after 24 h (Figure 5b–d). Here, we induced adiponectin, serving as a therapeutic agent. Adiponectin is an adipokine secreted by fat cells, and it has been reported to be inversely correlated with systemic chronic inflammation in obese individuals. We aimed to use it to reverse macrophage inflammation induced by orthodontic compressive force. The macrophages were treated with a compressive force and/or 10 μg/mL adiponectin for 24 h before being collected and analyzed. However, the results indicated that adiponectin had no effect on any of the markers, whether they were with or without compression (Figure 5e–h).

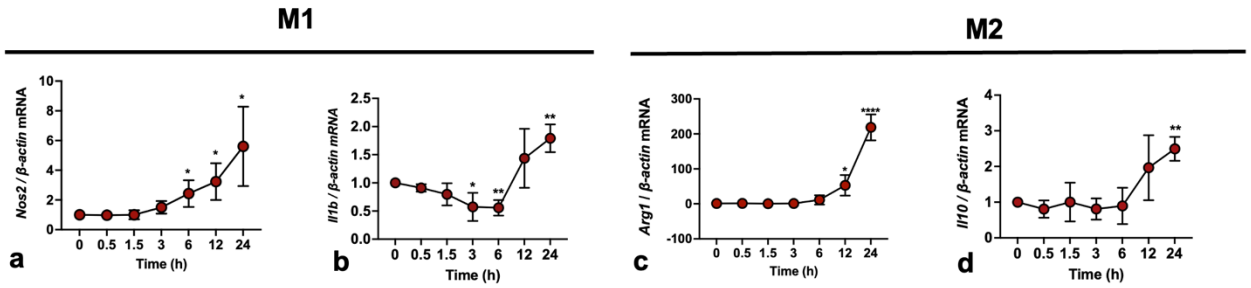

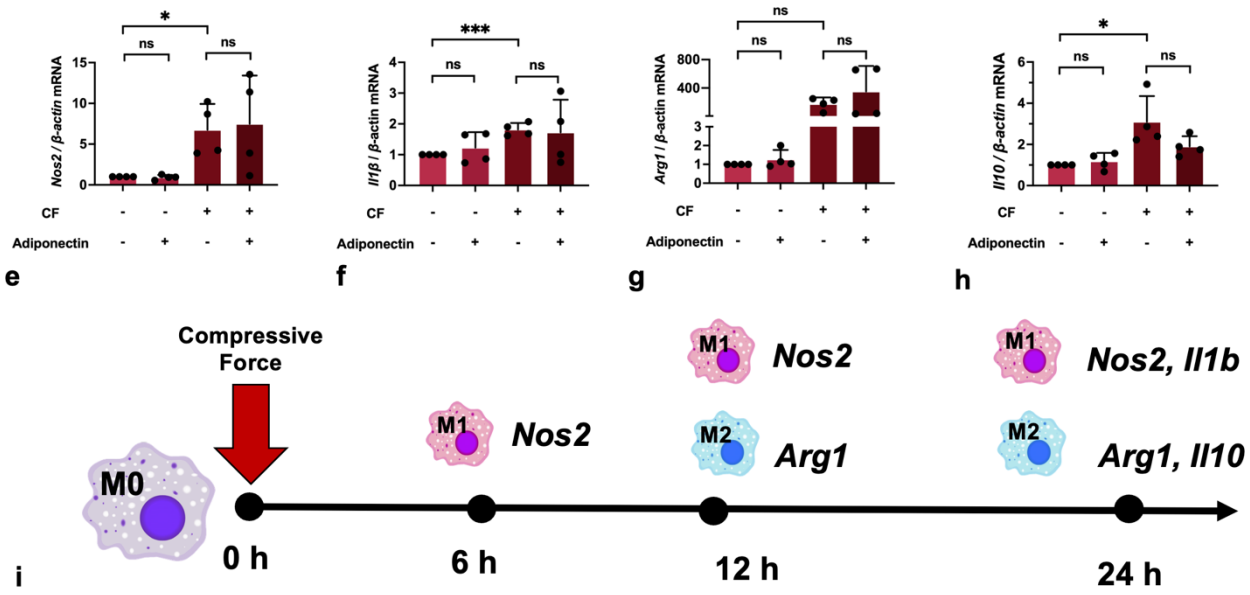

Figure 5. *The effects of compressive force on macrophage polarization markers. (a–d) Compressive force up-regulated Nos2, Il1b, Arg1, and Il10 levels. (e–h) Adiponectin did not affect Nos2, Il1b, Arg1, and Il10 expression. (i) Nos2 increased significantly 6 h after force-loading. Il1b, Arg1, and Il10 were elevated after 24 h. Values are expressed as mean ± SD; ns—not significant; * $p < 0.05$; ** $p < 0.01$; *** $p < 0.001$; **** $p < 0.0001$.*

7.3 Compressive Force Promoted the Expression of Saa3 and ApoE in Macrophages

To further investigate the effects of compressive force and adiponectin on macrophages, we performed a bioinformatic analysis based on public gene expression profile data (GSE18618). Setting an adjusted p-value of <0.01 and |log2 FC (fold change) | of ≥1 as the cutoff criteria, a total of 28 DEGs were identified. A total of 21 were upregulated and 7 were downregulated (Table 1 & Figure 6a). To confirm the possible action target of adiponectin, adiponectin and 28 proteins corresponding to DEGs were both mapped to the STRING. According to STRING, eight disconnected genes were filtered out, and the PPI network contained 21 nodes (20 DEGs and adiponectin) and 32 edges (Figure 6b). This shows that serum amyloid A3 (SAA3),

apolipoprotein E (APOE), and IL-1β connected directly to adiponectin. Then, *Saa3* and *ApoE* expression levels were estimated in the genes to verify the conclusion. The qRT-PCR results revealed that compressive force induced macrophages to up-regulate *Saa3* and *ApoE*, but adiponectin had no effect on them (Figure 6c & d).

Table 10. *DEGs in macrophages induced by compressive force.*

A total of 28 DEGs were identified in macrophages subjected to force compared to control, including 21 upregulated genes and 7 downregulated genes.

DEGs	Gene Name
Upregulated	*Saa3, BC100530, Lrg1, Chil3, Stfa2, Il1b, Ifitm1, Asprv1, Fpr1, Gm5483, Il1a, Apoe, Il1f9, Marcksl1, Arg2, Stfa2l1, C5ar1, Cd14, Ms4a8a, Stfa3, Slfn2*
Downregulated	*Cxcr4, Cd74, H2-Eb1, H2-Ab1, Hbb-bs, Hbb-bt, Hba-a1*

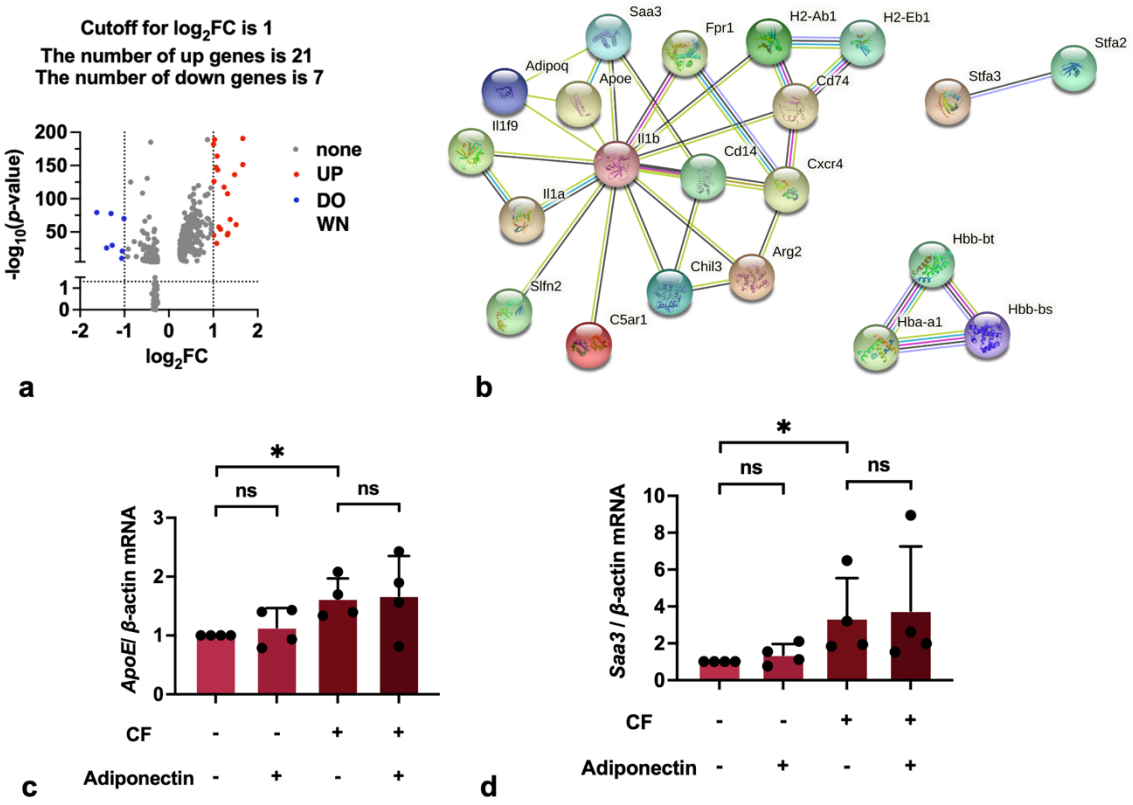

Figure 6. *Compression modulated adiponectin-related genes.*

*(a) Volcano plot illustrates significant differences in gene expressions pattern between macrophages with and without stimulation by compressive force. (b) Based on the STRING online database, top 21 upregulated or downregulated differential genes and adiponectin were filtered into the DEGs PPI network. (c,d) Increased mRNA expression of Saa3 and ApoE was detected by qRT-PCR. Values are expressed as mean ± SD; ns—not significant; * $p < 0.05$.*

7.4 Compression-Induced H3 Histone Acetylation Mediates M2 Polarization

Compressive stimulation significantly increased H3 histone acetylation levels (Figure 7a). Furthermore, 500 nM I-BET762 was used to prevent the acetylation reader from recognizing histone. The qRT-PCR results indicated treatment with I-BET762 alone did not affect cytokine expression in macrophages. However, it significantly dampened the enhancement of *Arg1* and *Il10*, M2 polarization markers, by compression (Figure 7f & g). Meanwhile, it had no effect on the up-regulation of *ApoE*, *Saa3*, *Nos2*, and *Il1b* (Figure 7b–e).

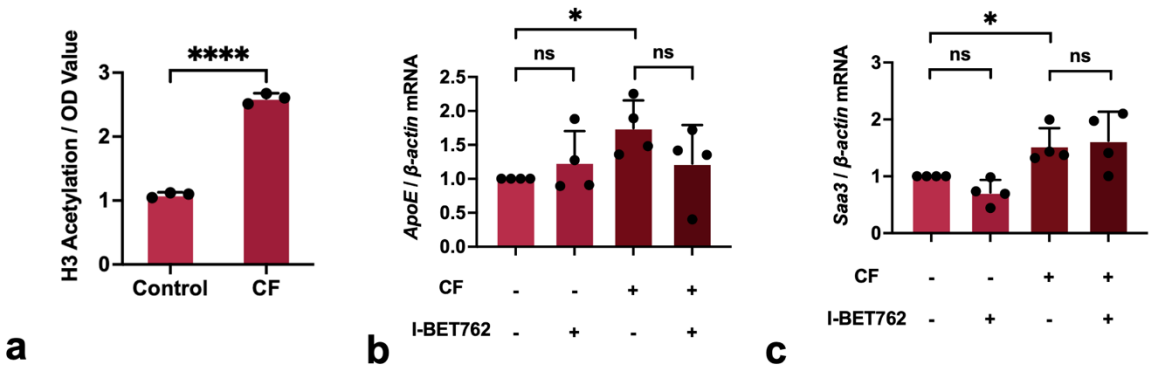

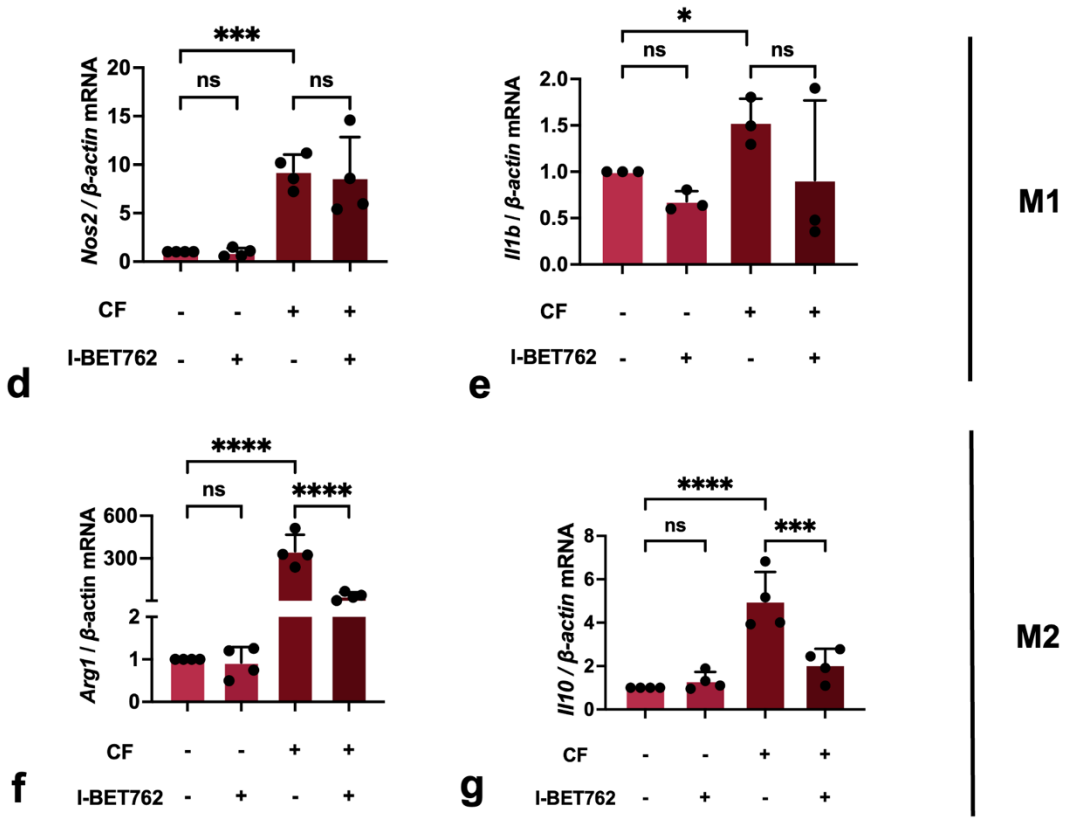

Figure 7. *Compressive force induced M2 polarization by promoting H3 histone acetylation.*

*(a) H3 histone acetylation level increased after force-loading. (b–e) ApoE, Saa3, Nos2, and Il1b showed no reaction to I-BET762 in the presence or absence of compression. (f & g) I-BET762 blunted the effects of force on Arg1 and Il10 expression. Values are expressed as mean ± SD; ns—not significant; * $p < 0.05$; *** $p < 0.001$; **** $p < 0.0001$.*

7.5 Compressive Force Induced Transient Lamin A/C Deficiency

Lamin A/C constitutes a protein meshwork located beneath the nuclear envelope. After applying compressive force, we observed a significant decrease in lamin A/C expression at 1 and 3 hours, with reductions of 35.25% at 1 hour and 33.11% at 3 hours. Notably, lamin A/C levels returned to baseline by the 6-hour mark (Figure 8a). Next, we stained the macrophages with anti-lamin A/C primary antibody and

fluorescent secondary antibody, then observed them using confocal laser fluorescence microscopy. The fluorescence intensity of lamin A/C exhibited a significant decrease at 3 hours (Figure 8c). However, there was no alteration in gene expression levels at either 1 or 3 hours (Figure 8b). These findings suggest that compressive force induces a transient lamin A/C deficiency at the protein level rather than at the gene level.

Moreover, a considerable proportion of macrophage nuclei displayed abnormal morphology at 1 hour, resembling shrunken peanut-like structures, which then partially recovered at 3 hours (Figure 8c & d). These macrophages with deformed nuclei still maintained a normal cellular profile and viability according to Calcein AM staining (Figure 8d). Interestingly, this nuclear deformation and lamin A/C protein reduction were both transient and essentially synchronized, being most prominent at 1 hour and then diminishing over time (Figure 8a & c). These data suggest that compressive force can condense nuclear structures, likely as an adaptive response to increasing external compression. However, the nuclei gradually adapt to the compressive force, partially recovering to their original structure.

To further elucidate the association between compressive force and the reduction of lamin A/C, we disrupted the cytoskeleton to prevent force transmission. Macrophages were pre-incubated with 2 μM cytochalasin D (PHZ1063, ThermoFisher) for 24 hours, a cytoskeleton-disrupting agent that induces F-actin depolymerization [90, 91], before being subjected to compressive force. The control group was treated with an equivalent volume of DMSO prior to compression force stimulation. Phalloidin staining revealed significant cytoskeletal disruption (Figure 8e), and Western blot analysis showed that lamin A/C were unable to respond to compressive force at all time points (Figure 8f), suggesting that the force-induced lamin A/C deficiency is cytoskeleton-dependent.

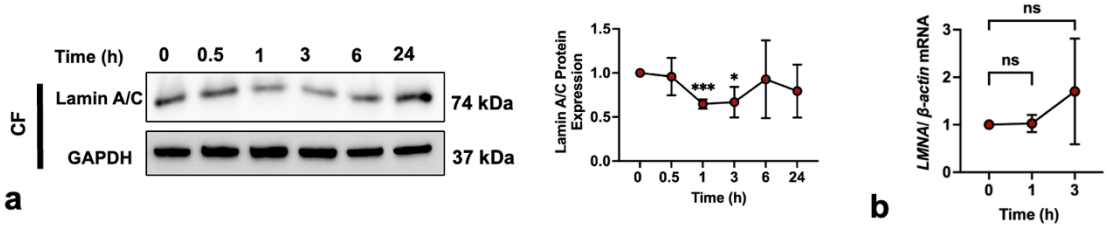

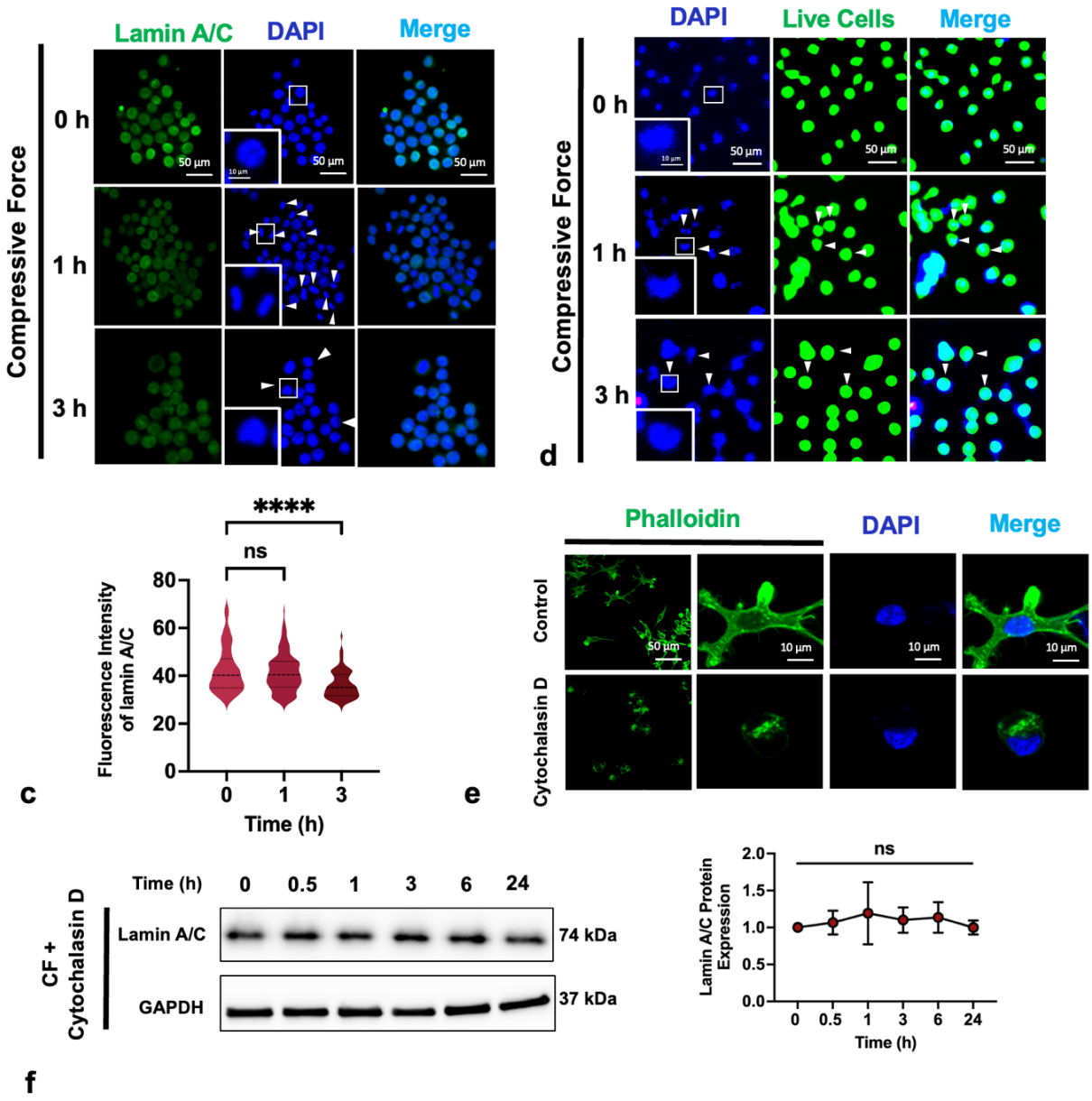

Figure 8. *Compressive force induced cytoskeleton-dependent lamin A/C protein suppression.*

(a & b) Compressive force transiently downregulated lamin A/C at the protein level after 1 and 3 hours; (c) Immunofluorescent staining and quantification demonstrated a transient decrease in lamin A/C and deformed nuclei induced by compression (white arrows indicate morphologically abnormal nuclei); (d) Calcein AM staining confirmed that cells with shrunken nuclei remained viable; (e) Cytochalasin D caused cytoskeleton destruction; (f) Cytochalasin D eliminated the inhibition of lamin A/C by

*compressive force. CF: compressive force. Values are expressed as mean ± SD: ns - not significant; *p < 0.05; **p < 0.01; ***p < 0.001; ****p < 0.0001.*

7.6 Lamin A/C Deficiency Increased Nuclear Permeability

To further investigate the role of lamin A/C, we transfected macrophages with siRNA to achieve a more sustained lamin A/C deficiency. qRT-PCR analysis revealed a significant decrease in *LMNA* mRNA after 24 and 48 hours of transfection (Figure 9b). Consistently, IF staining showed that lamin A/C protein levels decreased at 24- and 48-hours post-transfection but returned to baseline levels after 72 hours (Figure 9a). Western blotting results demonstrated that at 48 hours post-transfection, the lamin A/C protein inhibition rate reached approximately 44%-52% (Figure 9b). Hence, for all subsequent studies we selected 48 hours as the transfection duration. Additionally, 24-hour compressive force loading, previously verified to significantly affect inflammatory cytokine secretion, did not interfere with the inhibition of lamin A/C by *siLMNA* (Figure 9b).

Further, given that lamin A/C is a primary component of the nuclear lamina, a protein network that supports the inner nuclear envelope and encases the nuclear chromatin, we performed TEM assay to observe nuclear envelope. The data displayed that lamin A/C deficiency caused an ambiguous nuclear envelope (Figure 9c). Hence, we hypothesized that lamin A/C deficiency might lead to increased nuclear permeability.

Therefore, we assessed nuclear permeability using two types of fluorescent dextran with different molecular masses. The smaller molecular mass dextran (65-80 kDa) can passively diffuse into the nucleus through the nuclear pore transport complex (NPC), whereas the larger molecular mass dextran (500 kDa) requires NPC deformation or nuclear damage for permeation (Figure 9e). Lamin A/C deficiency significantly increased the permeability of the large molecular dextran ($p < 0.001$). Additionally, we introduced a siRNA-resistant *LMNA* mutant (sR *LMNA*) to rescue the lamin A/C

deficiency induced by *siLMNA*. The results of a protein assay suggested that sR *LMNA* significantly reversed the lamin A/C deficiency at 48 hours (Figure 9d). As expected, this increased permeability can be reversed by sR *LMNA* (Figure 9f & g). This evidence confirmed that lamin A/C plays a crucial role in maintaining nuclear isolation of macromolecules.

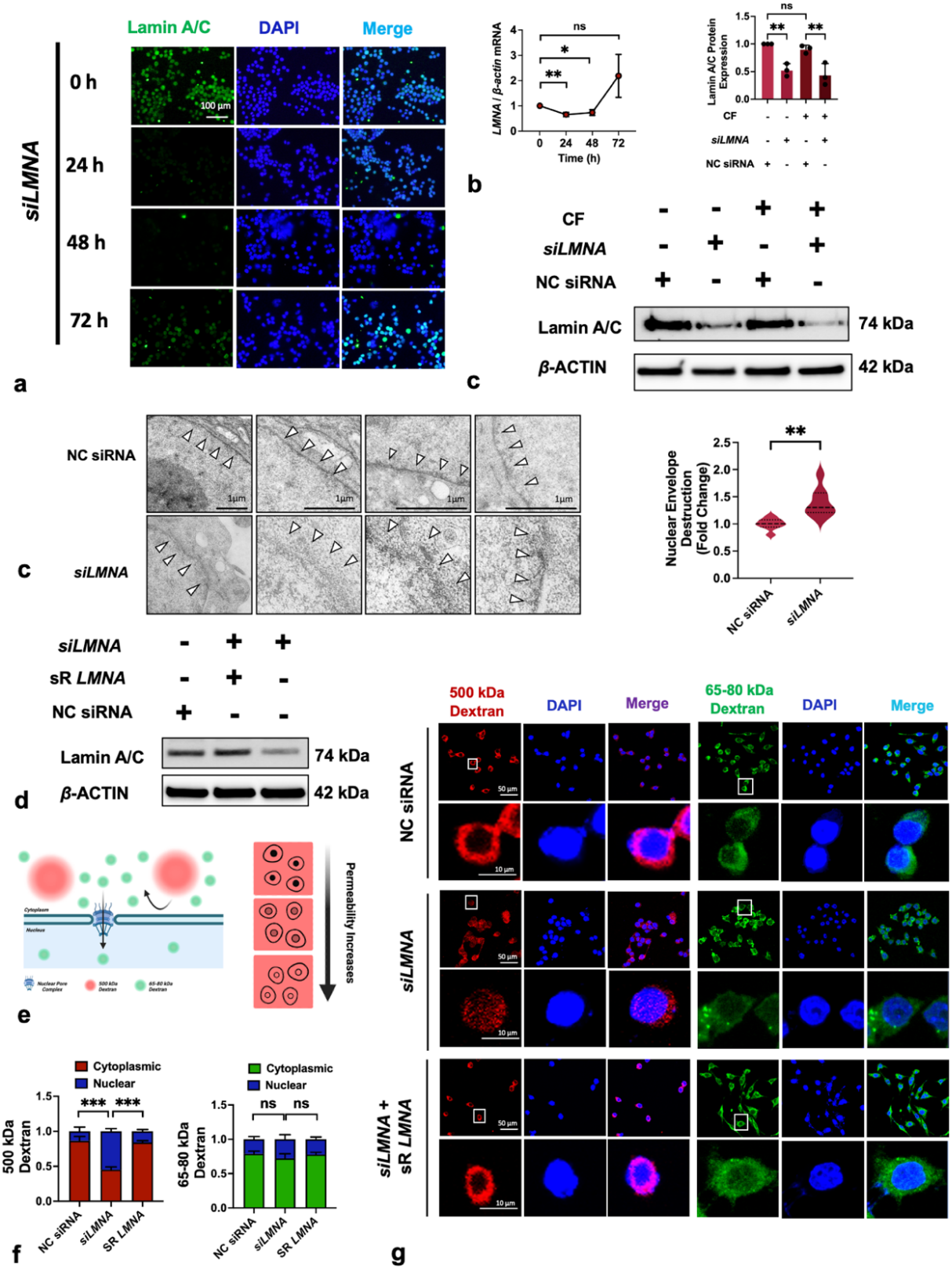

Figure 9. *siLMNA induced lamin A/C deficiency and enhance nuclear permeability. (a) IF results showed siLMNA down-regulated lamin A/C protein levels; (b & c) siLMNA suppressed the LMNA gene expression during the 24- to 48-hour period, and reduced lamin A/C protein levels, whether compressive force was present or not; (d) TEM displayed that siLMNA caused impairment of the nuclear envelope; (e) Under physiological conditions, 65-85 kDa dextran can passively transport into the nucleus through NPC but 500 kDa dextran cannot permeate the nuclear envelope due to its larger molecular diameter than NPCs. A schematic graphic exhibits the cells with different permeabilities to dextran; (f & g) The siLMNA significantly increased the nuclear permeability to 500 kDa dextran and sR LMNA eliminated the effect. CF: compressive force; NC: negative control. White arrows: nuclear envelope. Values are expressed as mean ± SD: ns - not significant; *p < 0.05; **p < 0.01; ***p < 0.001; ****p < 0.0001.*

7.7 Lamin A/C Deficiency Enhanced Effects of Compressive Force

We further investigated the role of lamin A/C in cellular mechanotransduction. First, we evaluated the effects of compressive force on migration. Interestingly, while lamin A/C deficiency induced by siRNA significantly enhanced cellular migration, cells exposed to compressive force, which also induces lamin A/C deficiency, did not show increased migration (Figure 10a). We hypothesize that, while lamin A/C plays an essential role in macrophage migration, compressive force may introduce other factors related to migration that mask the positive effects typically associated with lamin A/C deficiency.

Second, given the increased nuclear permeability, we hypothesized that lamin A/C deficiency may influence the nuclear translocation of transcription factors involved in mechanotransduction. Yes-associated protein 1 (YAP1), a well-known mechanosensitive transcription factor, accumulates in the nucleus under mechanical

force [92]. Western blot analysis revealed that both 48-hour *siLMNA* transfection and 24-hour compressive force loading increased the level of active YAP1, instead of total YAP1 (Figure 10b). Moreover, immunofluorescence demonstrated that the intranuclear signal of YAP1 in the CF + *siLMNA* group was significantly increased compared to other groups (Figure 10c), supporting the hypothesis that lamin A/C restricts compressive force-induced YAP1 translocation. Another noteworthy observation is that cells subjected to compressive force displayed nuclei that appeared to be shrinking, and cells treated with both compressive force and *siLMNA* exhibited even more pronounced nuclear deformations (Figure 5c). Therefore, it is reasonable to conclude that the nucleus tends to undergo morphological changes under compression, and lamin A/C serves as a structural support.

Moreover, YAP1 is implicated in regulating cellular proliferation [93] and macrophage polarization [94]. Thus, we further examined the gene expressions of *Arg1*, *Il10*, and *NOS2*, as well as proliferation. As expected, 1 g/cm^2 compression elicited inflammatory gene expression and inhibited cell viability, with deficient lamin A/C exacerbating these effects (Figure 10d & e). Interestingly, when comparing the CF + *siLMNA* group with the CF group, *siLMNA* promoted the nuclear localization of YAP1 rather than its protein level. Nevertheless, it still intensified the effects of compressive force on polarization markers and proliferative viability (Figure 10d & e). This suggests that the subcellular localization of YAP1 may be more critical than its total level in mechanotransduction. Furthermore, as YAP1 concentration increased in the nucleus, the signal tended to form punctate aggregations. This could suggest the presence of regions within the nucleus with a high affinity for YAP1, such as nucleoli, nuclear bodies, or specific chromatin sites, where YAP1 preferentially accumulates rather than being uniformly distributed. However, more evidence is needed to definitively identify these high-affinity regions

or substances. In conclusion, lamin A/C deficiency exaggerates the cellular response to compressive force by promoting the nuclear translocation of YAP1.

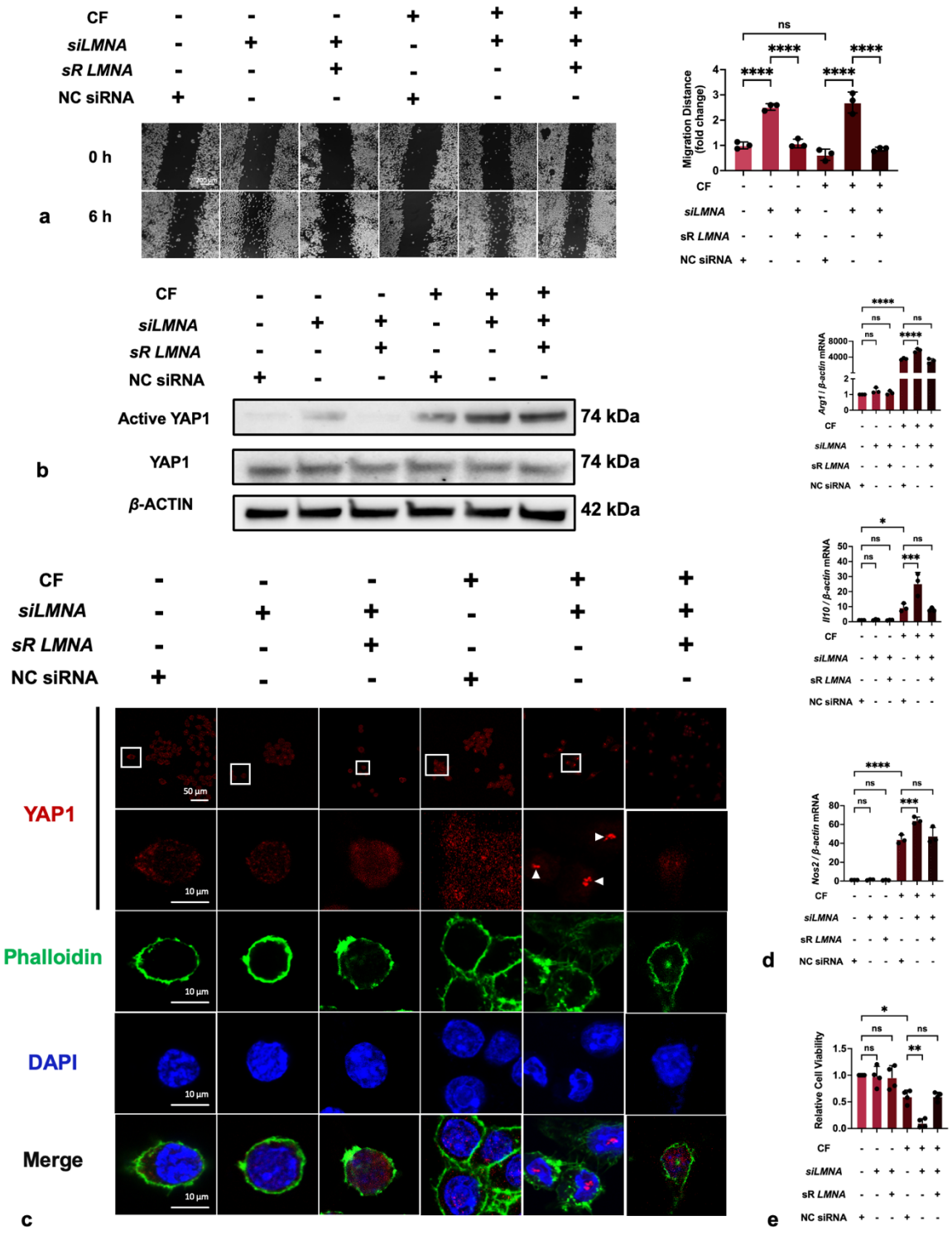

Figure 10. *Lamin A/C deficiency enhanced the effects of compressive force, including promoting YAP1 translocation, inducing polarization, and inhibiting proliferation.*

*(a) Lamin A/C deficiency enhanced migration function of macrophages; (b) Lamin A/C deficiency and compressive force both increased active YAP1 protein levels. (c) IF staining showed the distributions of YAP1 in nuclei and cytoplasm (white arrows: YAP1 accumulation in nuclei). (d) Compressive force induced the expression of Arg1, Il10 and Nos2, and siLMNA enhanced these effects. (e) Compressive force inhibited cellular viability, with siLMNA further reducing it. CF: compressive force; NC: negative control. Values are expressed as mean ± SD: ns - not significant; *p < 0.05; **p < 0.01; ***p < 0.001; ****p < 0.0001.*

7.8 Lamin A/C Deficiency Detached LINC Complex from Nucleus

The LINC complex is a vital structure that connects the cytoskeleton to the lamina, playing a critical role in intracellular mechano-transmission [95]. Therefore, we evaluated the impact of lamin A/C deficiency and compressive force on the LINC complex. The protein levels of SUN1 and SUN2, components of the LINC complex, were significantly suppressed by compressive force, but unaffected by *siLMNA* (Figure 11a). Moreover, based on immunofluorescence images, SUN1 signals are assembled in the nucleus, but *siLMNA* and (or) compressive force caused SUN1 to diffuse into the cytoplasm (Figure 11b). Similarly, an intact circle of SUN2 that surrounded the nucleus was observed in the control group but *siLMNA* and (or) compressive force resulted in distinct disruption of the SUN2 circle (Figure 11b). Notably, these detachments of SUN1 and SUN2 were reversed by the introduction of sR *LMNA*. Additionally, we conducted a fractionation experiment to separate nuclear and cytoplasmic components. Through centrifugation, the nuclear envelope, nucleolus, chromatin, and other nuclear materials are separated into the nuclear fraction, while cell membrane fragments, cytoplasm, endoplasmic reticulum, mitochondria, and other components are separated into the cytoplasmic fraction. SUN1 and SUN2 were detected in the cytoplasm whenever lamin A/C deficiency or

compressive force was applied (Figure 11c). In summary, only compressive force reduced the protein SUN1 and SUN2, but compressive force and (or) lamin A/C deficiency led to the detachment of SUN1 and SUN2 from the nucleus.

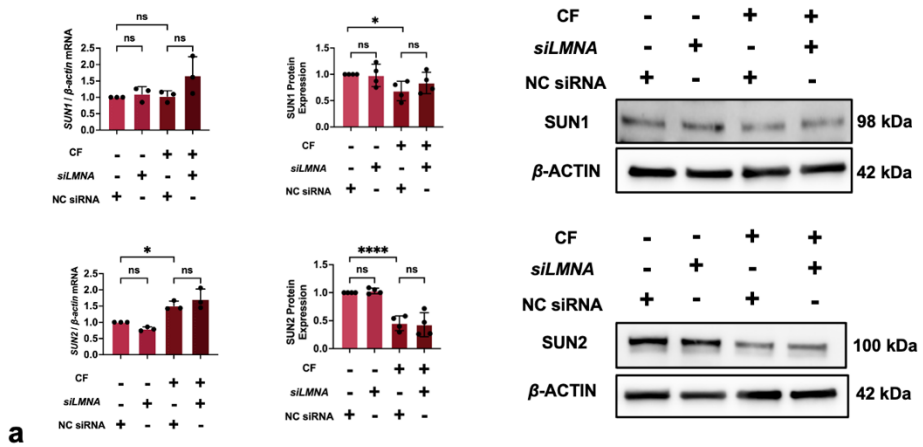

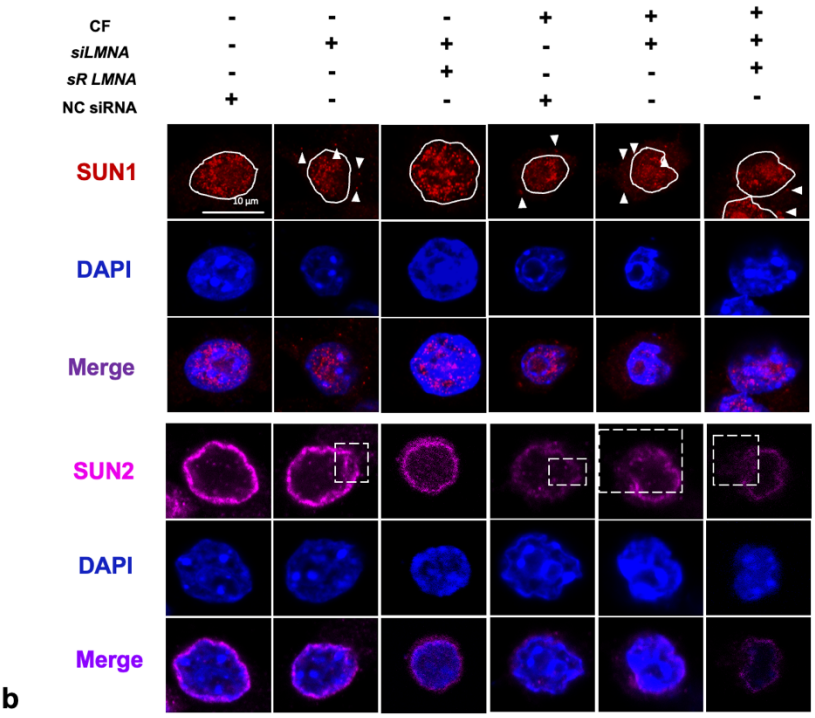

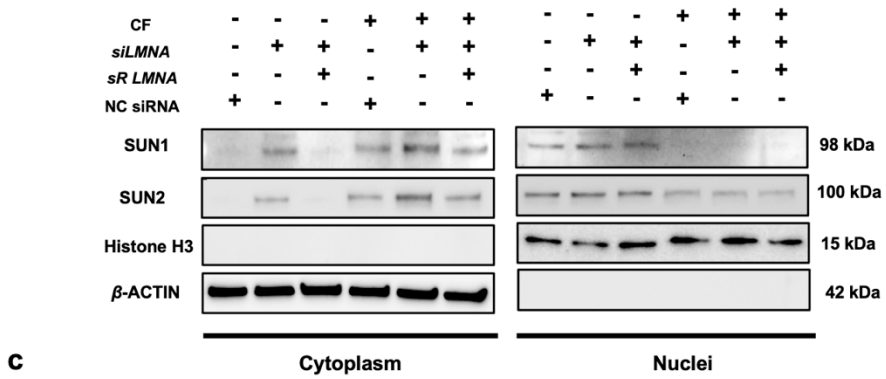

Figure 11. *Compressive force and siLMNA influenced the LINC complex.*

*(a) Compressive force, instead of siLMNA，significantly decreased protein expression of SUN1 and SUN2; (b & c). Compressive force or (and) siLMNA detached SUN1 and SUN2 from the nuclei (white solid line: the boundaries of the cell nucleus; white arrows: SUN1 signals in cytoplasm; white square: discontinuous signal indicating SUN2 destruction). CF: compressive force; NC: negative control. Values are expressed as mean ± SD: ns - not significant; *p < 0.05; **p < 0.01; ***p < 0.001; ****p < 0.0001.*

7.9 Lamin A/C Deficiency Inhibited Compressive Force-Induced DNA Damage and IRF4 Expression

Considering that both compressive force and *siLMNA* resulted in nuclear deformation, we assessed their effects on DNA damage. γH2AX, a biomarker for DNA double-strand breaks [96], was assayed by IF and Western blot. These experiments revealed that γH2AX is located in the nucleus and is significantly increased by compressive force (Figure 12a & b). Interestingly, although lamin A/C is known as a nuclear supporter due to its proportional relationship with nuclear stiffness, *siLMNA* reduced significantly γH2AX protein levels (Figure 12a). We further corroborated these findings with a comet assay. Specifically, cells subjected to compressive force had the longest 'comet tail' comprised of DNA fragments and *siLMNA* significantly shortened these tails (Figure 12c). Therefore, we believed that compressive force elicited DNA damage in macrophages, and this damage was reduced by lamin A/C deficiency. Consistently, our results also demonstrated that compressive force increased interferon regulatory factor 4 (IRF4) levels, a transcription factor associated with the anti-inflammatory activation of macrophages [97, 98], and phagocytosis. Notably, these two effects can be eliminated by lamin A/C deficiency (Figure 12d & e). These results showed that lamin A/C deficiency can reverse some effects of compressive

force on macrophages (promoting DNA damage, IRF4 expression, and phagocytosis), rather than amplifying them.

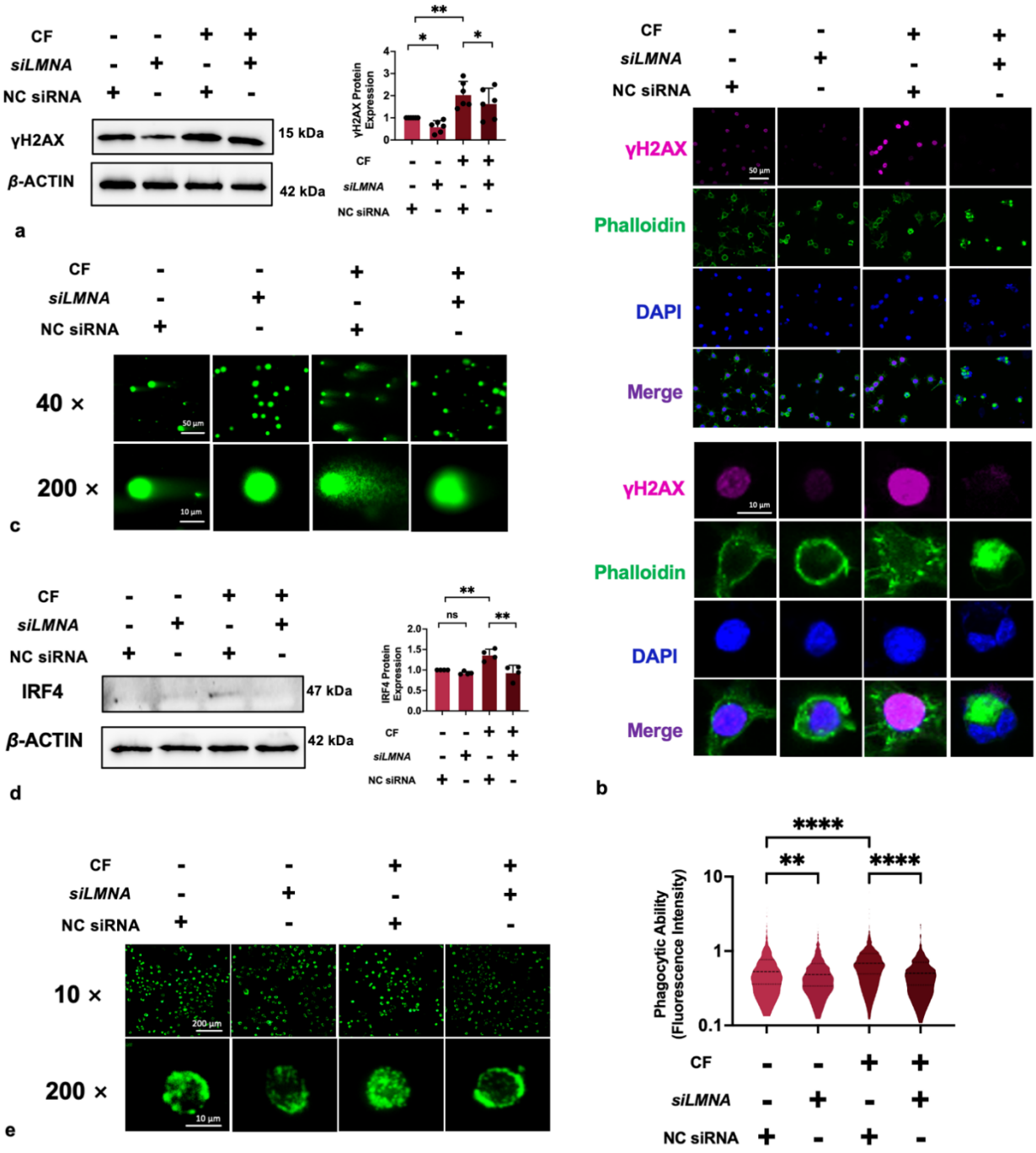

Figure 12. *Compressive force-induced functional alterations were reversed by siLMNA.*

*(a - b) The effects of compressive force and (or) siLMNA on γ-H2AX; (c) Comet assay revealed that compressive force caused more DNA fragments, but siLMNA eliminated this effect; (d) The effects of compressive force or (and) siLMNA on IRF4 protein level; (e) The macrophages phagocytosis function was enhanced by compressive force but inhibited by siLMNA. CF: compressive force; NC: negative control. Values are expressed as mean ± SD: ns - not significant; *p < 0.05; **p < 0.01; ***p < 0.001; ****p < 0.0001.*

7.10 Cementoblasts Functions were Impaired by Compression, instead of Macrophage Conditioned Medium

To further investigate the regulation of cementum by immune cells, force-activated macrophages medium supernatant or 1 g/cm^2 hydrostatic pressure were used to treat cementoblasts for 24 h. Unexpectedly, although cementoblasts migration or OPG mRNA was inhibited directly by compression, neither of them reacted to the macrophage medium (Figure 13a & b). Interestingly, we found that mRNA level of a mechanoreceptor, PIEZO1, increased in cementoblasts subjected to compressive force (Figure 13c). Meanwhile, the inhibitor of mechanoreceptor, GSMTX4 can partly rescue the migration impairment induced by compression (Figure 13 d). These data suggest that cementoblasts can directly response to compressive force, probably *via* mechanoreceptors Piezo1.

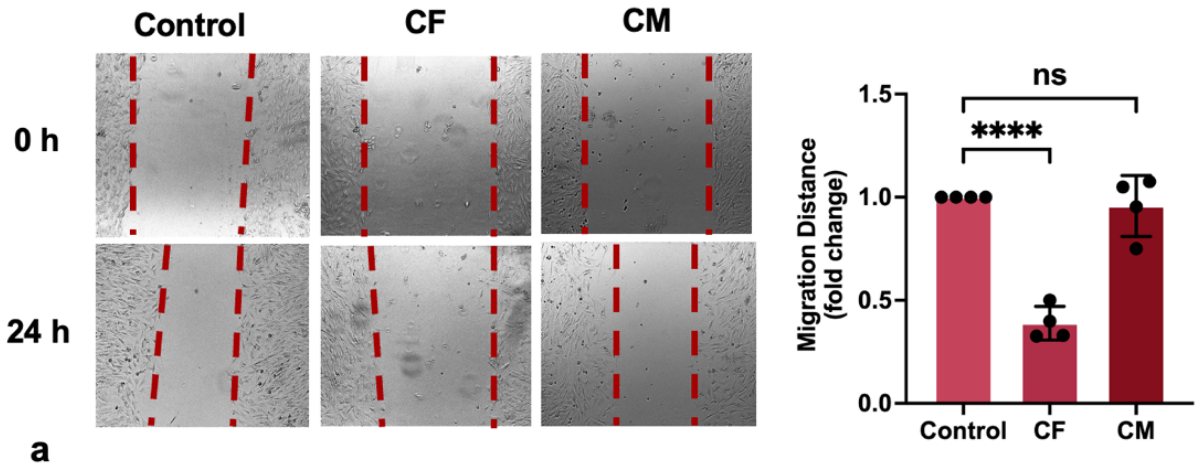

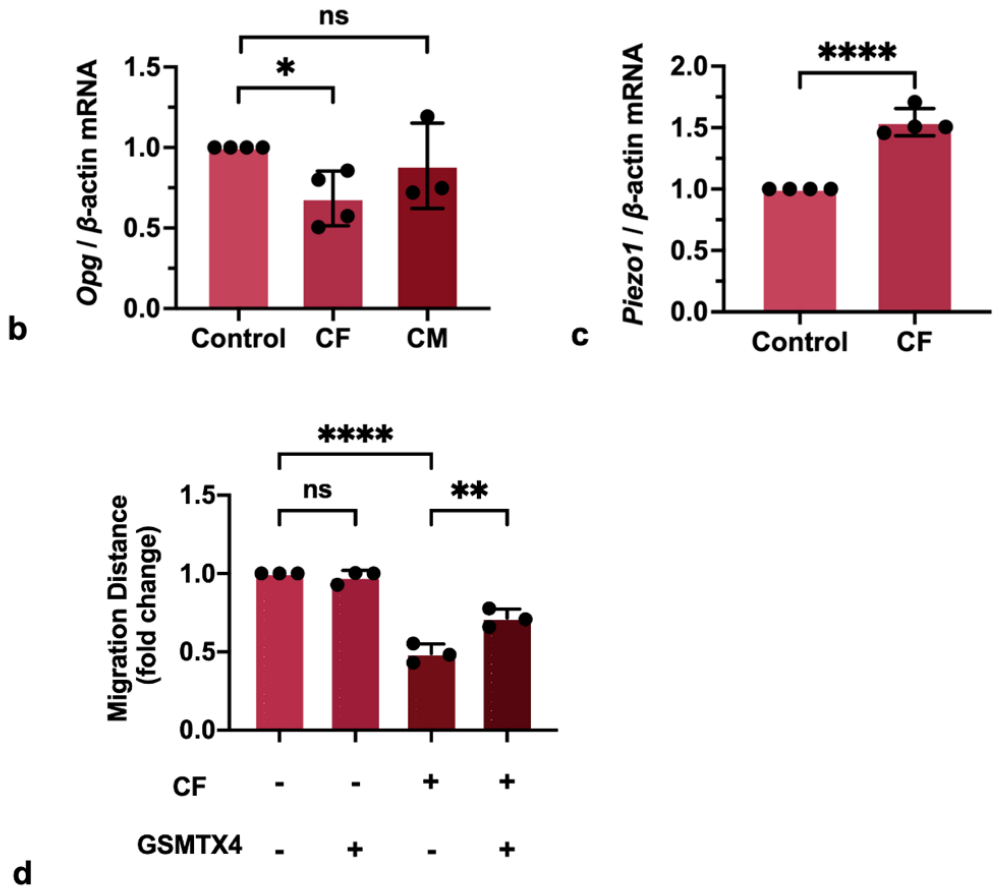

Figure 13. *Compression impaired cementoblastic functions.*

*(a) The migration distance of cementoblasts decreased after 24 hours of force application but remained unaffected by incubation with conditioned medium (CM); (b) qRT-PCR analysis revealed that compressive force suppressed Opg expression within 24 hours; (c) Compressive force upregulated the expression of Piezo1 at the gene level in cementoblasts. (d) Inhibition of Piezo1 mitigated the migration impairment caused by compressive force. Values are expressed as mean ± SD: ns (not significant); *p < 0.05, **p < 0.01, ***p < 0.001, ****p < 0.001.*

7.11 Compressive Force Regulates Genes Expression of Cementoblasts

We profiled genes expression of cementoblasts after loading 1 g/cm^2 compressive force, using RNA-seq. Based on the results, 6932 DEGs were confirmed (3715 genes were up-regulated and 3217 were down-regulated) (Figure 14a). PPI network analysis further revealed that 622 DEGs significantly associated with each other (Figure 14b). The 12 most critical genes (degree > 18) include *Kif11*, *Pkm*, *Brca1*, *Ccna2*, *Brca2*, *Bub1*, *Mapk8*, *Exo1*, *Cdc20*, *Gpi1, Cenpe* and Fau. Furthermore, we performed GO enrichment analysis on up-regulated and down-regulated DEGs. Interestingly, among the top 10 most significantly enriched biological functions for the upregulated genes, 8 are related to hypoxia or angiogenesis (the latter is usually the biological response to the former [99]). In contrast, among the top 20 enriched biological functions for downregulated genes, 19 are related to biomineralization.

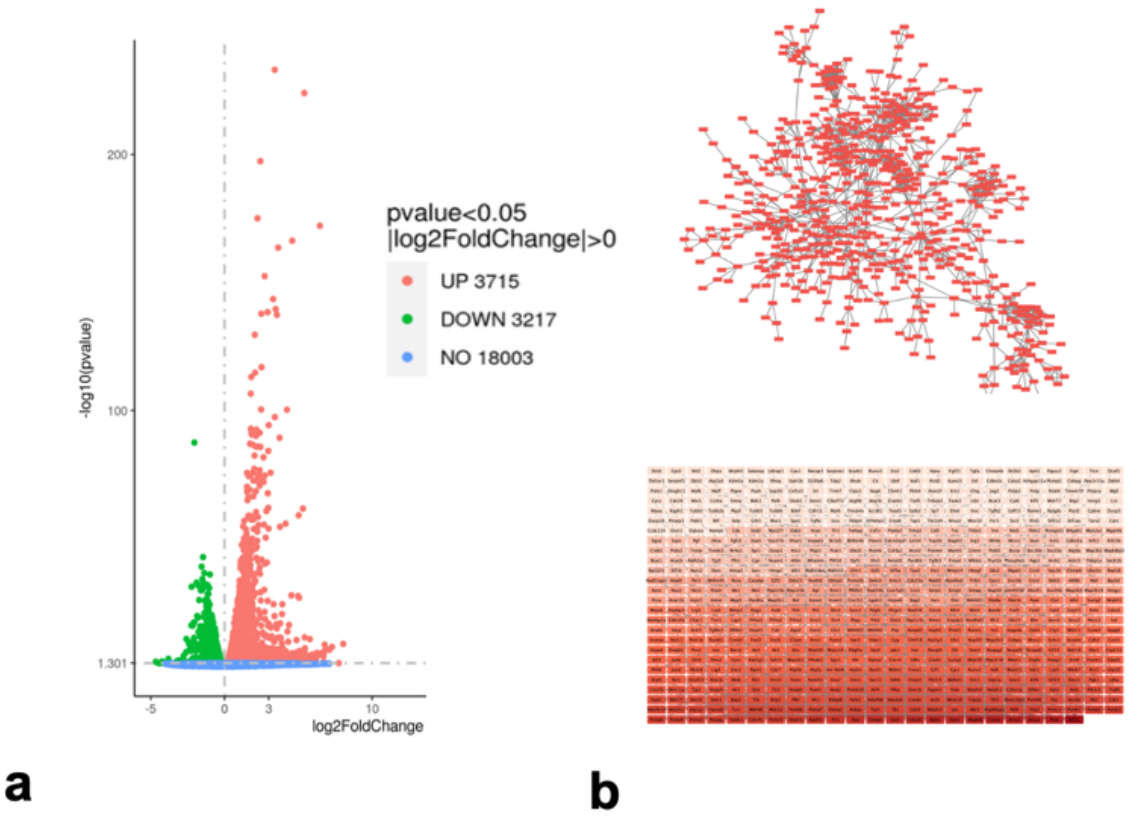

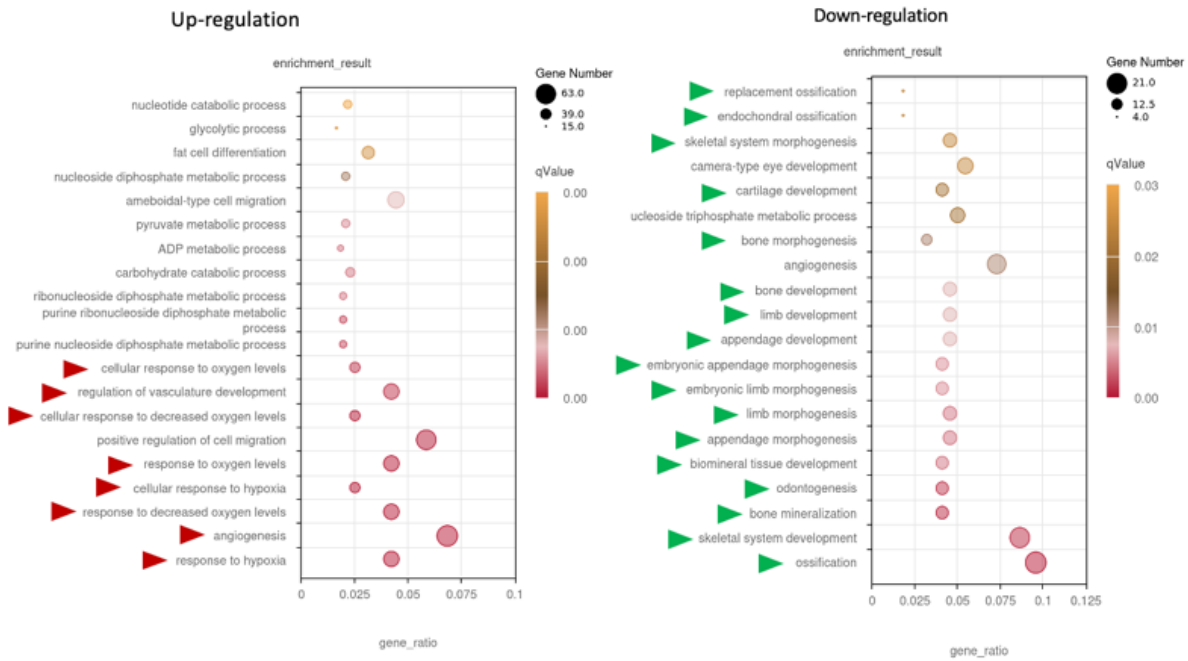

c

Figure 14. *Compressive force regulated cementoblasts genes expression.*

(a) Volcano plot showed that compressive force up-regulated 3715 genes and inhibited 3217 genes; (b) PPI analysis was performed on all DEGs, resulting in a PPI network consisting of 622 nodes. The nodes were ranked according to the degree of centrality and color-coded to indicate their importance within the network; (c). Up-regulated and down-regulated DEGs were used to performed gene ontology (GO) enrichment analysis, respectively. Most relevant 20 biological processes represented as a bubble plot colored by q-value and size constrained by number of DEGs contributing to term and ordered by q-value (Red arrows indicates hypoxia-related processes, green arrows are for mineralization-related processes).

7.12 Cementoblasts Expressed Piezo1 and Responded to Piezo1 Activator by Reducing Proliferation and Migration

Piezo1 is a mechanically sensitive ion channel that forms a homotrimer and adopts a triple-blade propeller-like structure, which is attached to a central ion-conducting pore with a cap [100] (Figure 15a). Its curved blades are embedded in the cytomembrane to sense membrane tension [101]. IF showed that Piezo1 was expressed on the cytomembrane of cementoblasts (Figure 15a). Hence, we believed Piezo1 is the sensor to compressive force in cementoblasts. Piezo1 activator, Yoda1, was used to treat cells and its effects on cellular behaviors were analyzed. Cells proliferation was inhibited by 20 μM Yoda1, rather than 5 μM or 10 μM (Figure 15b). Scratch assay indicated that 5 and 10 μM Yoda1 significantly reduced cell migration. (Figure 15c). Piezo1 responds to mechanical force by inducing monovalent and divalent cation influx to activate a downstream signaling pathway. RNA-seq analysis revealed that Yoda1 upregulated 128 genes and downregulated 81 genes (Figure 15d). These genes are enriched in processes related to mineralization and hypoxia (Figure 15d), which, as expected, overlap significantly with the DEGs induced by compressive force.

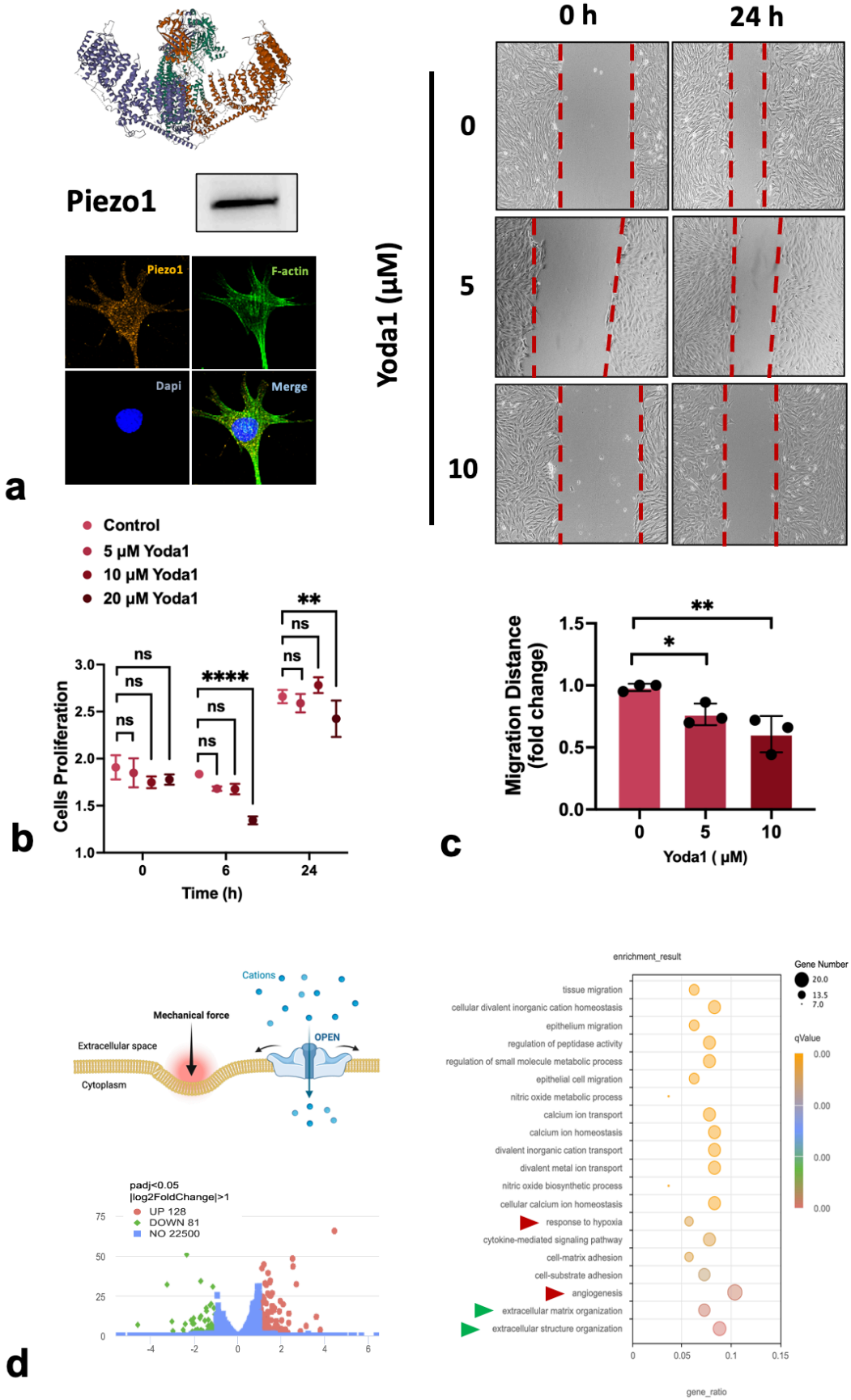
a
Piezo1
Piezo1
F-actin
Dapi
Merge
0 h
24 h
Yoda1 (μM)
0
5
10
b
Control
5 μM Yoda1
10 μM Yoda1
20 μM Yoda1
Cells Proliferation
Time (h)
ns
****
**
c
Migration Distance (fold change)
Yoda1 (μM)
d
Cations
Mechanical force
Extracellular space
Cytoplasm
OPEN
padj<0.05
|log2FoldChange|>1
UP 128
DOWN 81
NO 22500
enrichment_result
Gene Number
qValue
tissue migration
cellular divalent inorganic cation homeostasis
epithelium migration
regulation of peptidase activity
regulation of small molecule metabolic process
epithelial cell migration
nitric oxide metabolic process
calcium ion transport
calcium ion homeostasis
divalent inorganic cation transport
divalent metal ion transport
nitric oxide biosynthetic process
cellular calcium ion homeostasis
response to hypoxia
cytokine-mediated signaling pathway
cell-matrix adhesion
cell-substrate adhesion
angiogenesis
extracellular matrix organization
extracellular structure organization
gene_ratio

Figure 15. *Piezo1 was expressed on the cementoblasts and affects cellular functions. (a) The three-dimensional structure of Piezo1 and its localization in cementoblasts; (b & c) The effects of Piezo1 activator (Yoda1) on cementoblasts proliferation and migration; (d) The activation of Piezo1 induced cations influx and over 200 genes were expressed differentially. The DEGs were enriched in hypoxia related process (red arrows) and mineralization-related process (green arrows). Values are expressed as mean ± SD: ns (not significant); *p < 0.05, **p < 0.01, ***p < 0.001, ****p < 0.001.*

7.13 Compressive Force Mediated Hypoxia/Angiogenesis through Piezo1/HIF-1α Axis

KEGG enrichment analysis showed that Piezo1-induced DEGs were enriched in HIF-1α signaling pathway, a classic pathway associated hypoxia (Figure 16a). Western blot verified that 5 μM Piezo1 activator significantly up-regulated HIF-1α (Figure 16b). Moreover, compressive force can enhance HIF-1α protein and mRNA levels, and downstream vascularization genes expression (vascular endothelial growth factor (VEGF, *Vegf)*, angiopoietin 1 (ANGPT1, *Angpt1)* and angiopoietin-like 4 (ANGPTL4, *Angptl4*). Data showed that Piezo1 inhibitor can eliminated all enhancement (Figure 16c & d).

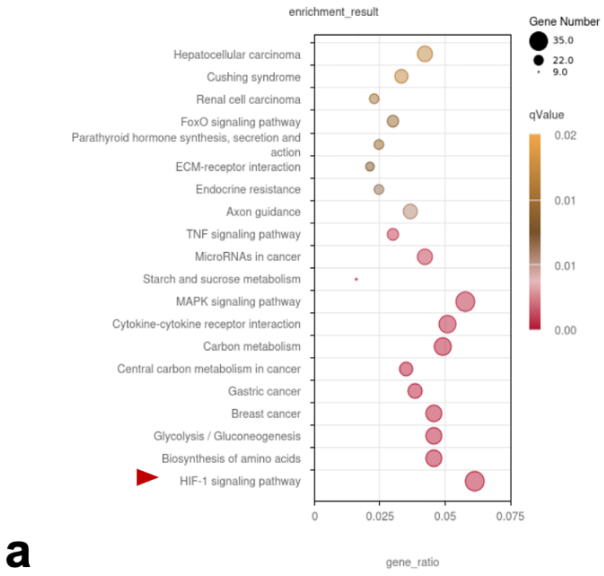

a

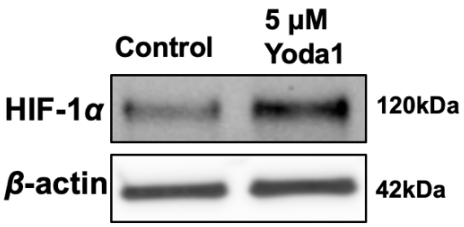

b

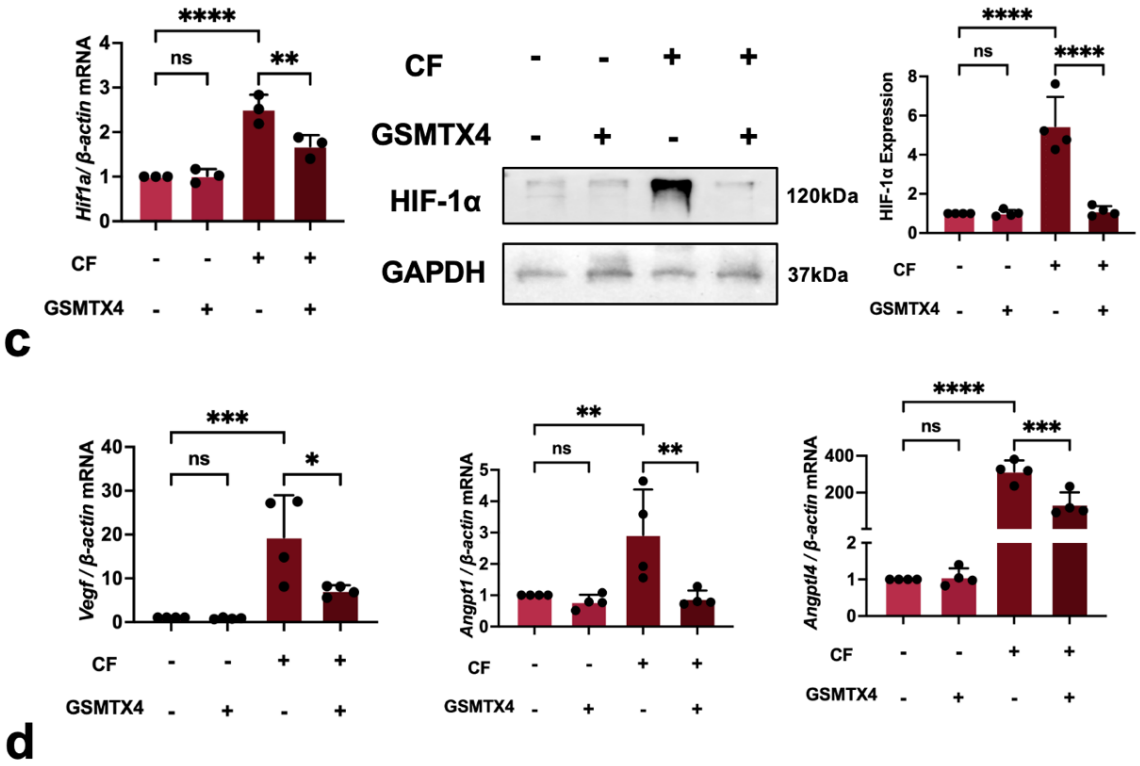

Figure 16. *Compressive force activated the Piezo1/Hif-1α axis to induce angiogenesis.*

*(a) KEGG analysis indicated that the genes upregulated by Yoda1 were significantly enriched in the HIF-1 signaling pathway; (b) Treatment with 5 μM Yoda1 led to an increase in HIF-1α protein levels; (c & d) Compressive force induced the upregulation of HIF-1α and its downstream vascularization-related genes; however, this effect was abolished by GSMTX4. Values are expressed as mean ± SD: ns (not significant); *p < 0.05, **p < 0.01, ***p < 0.001, ****p < 0.001.*

7.14 Compressive Force Suppressed Cementoblasts Mineralization through Piezo1

Our data demonstrated that Piezo1 activator reduced the expression of the mineralization-related genes, *Runx2*, *Opn*, *Sp7* and *Opg* mRNA. *Sp7* is the most sensitive gene, its mRNA level was to one-fourth of the control group 24 h after being treated by10 μM Yoda1 (Figure 17a). Similarly, the protein assay revealed that the

Piezo1 activator caused time-dependent inhibition of RUNX2, SP7, and BMP2, resulting in almost no detectable expression of SP7 in cementoblasts after 24 hours (Figure 17b). ALP and Alizarin Red staining results showed that 5 μM and 10 μM Piezo1 significantly inhibited cementogenic differentiation and mineral node formation (Figure 17c).

Furthermore, we observed that compressive force also reduced RUNX2 and SP7 expressions, while the BMP2 expression remained unaffected. Meanwhile, these reductions were completely rescued by a Piezo1 inhibitor (Figure 17d). Thus, these figures supported the assumption that compressive force inhibits the expression of mineralization-related proteins, cementogenic differentiation, and mineral nodule formation through Piezo1 in cementoblasts.

7.15 The Effects of Compressive Force on Cementoblasts are Ca^{2+}-unassociated

Ca^{2+} is the most well-known downstream effector of Piezo1 [102], as well as crucial second messenger in mammalian cells [103]. Hence, this part section aimed to investigate the role of Ca^{2+} in the impairments of cementoblasts by compressive force. Compressive force induced the intracellular Ca^{2+} concentration to shortly increase 1 hour after applying force (Figure 18a). Thus, we pre-incubated cells with a Piezo1 inhibitor and found that it significantly prevented Ca^{2+} influx at this time point (Figure 18b).

However, we used Ca^{2+}-free medium to culture cells to cut off their Ca^{2+} supply. Surprisingly, exclusion of Ca^{2+} did not affect the influence of compressive force, specifically, the inhibition of migration and mineralization (Figure 18c & d). Therefore, we believe that for cementoblasts, the mechanical force-induced changes in cell function mediated by Piezo1 are independent of the presence of calcium ions. The downstream targets of Piezo1 mediating this process require further investigation.

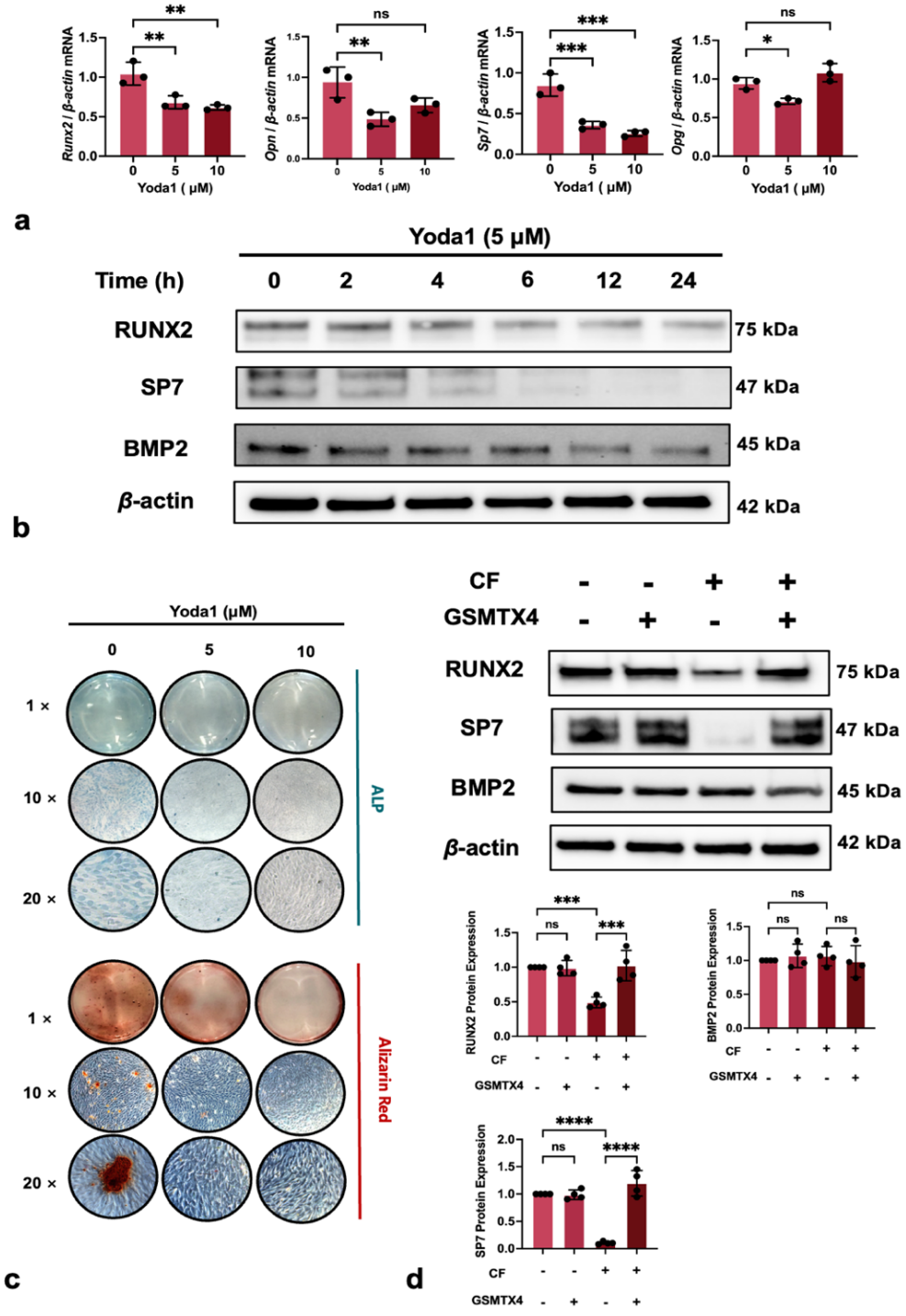

Figure 17. *Compressive force impaired mineralization via Piezo1.*

(a & b) Piezo1 activator inhibits mineralization-related genes and proteins expression; (c) ALP and Alizarin staining elucidated that Piezo1 activator inhibits cementogenic differentiation and mineral nodes formation; (d) Piezo1 inhibitor

*(GSMTX4) recovered the inhibition of mineralization-related proteins by compressive force. Values are expressed as mean ± SD: ns (not significant); *p < 0.05, **p < 0.01, ***p < 0.001, ****p < 0.001.*

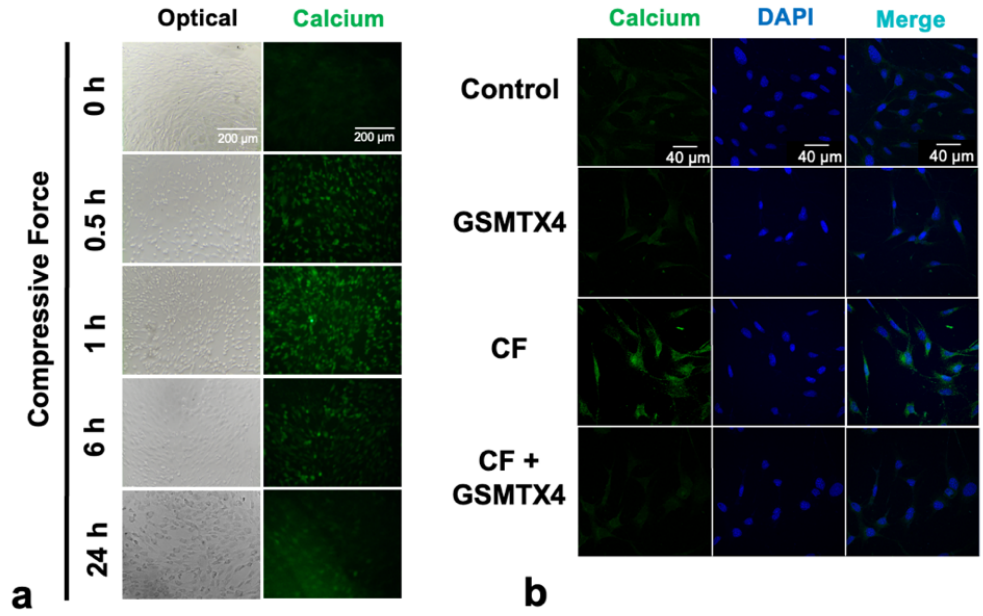

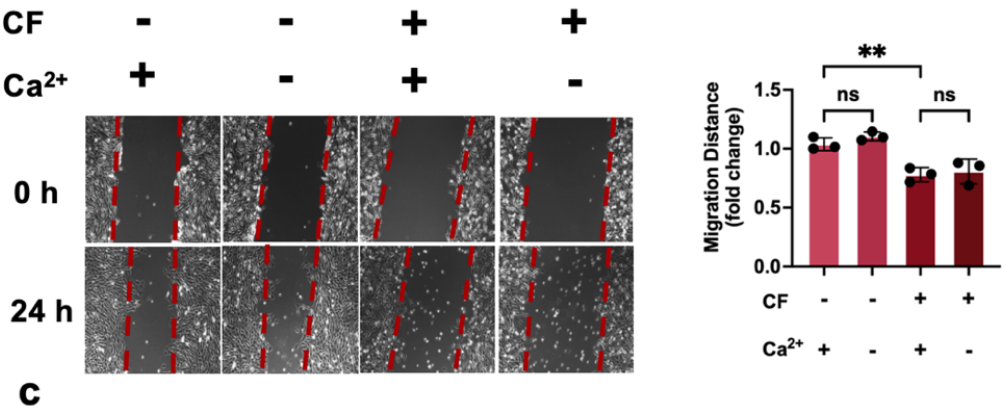

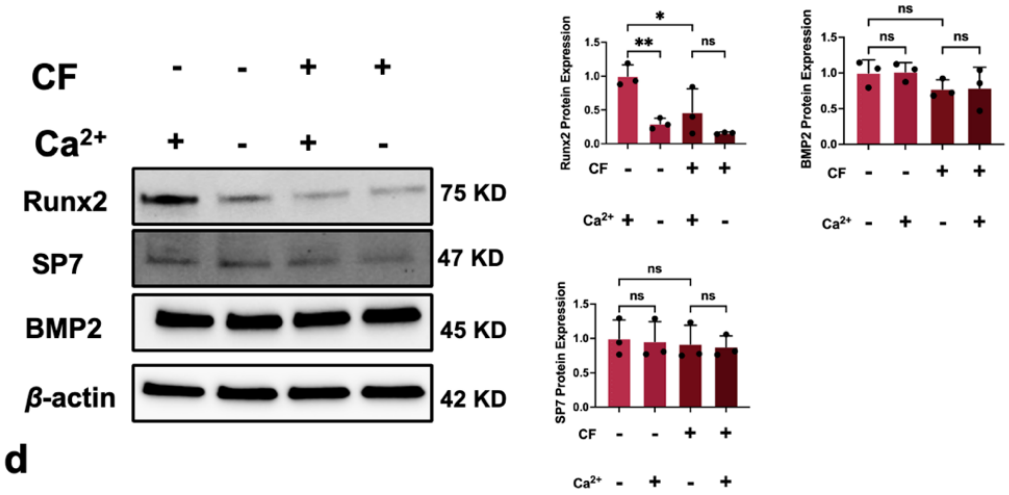

Figure 18. *Ca^{2+} were not essential for the process that compressive force affects cementoblasts through Piezo1.*

*(a) Compressive force rapidly increased intracellular Ca^{2+} concentration; (b) This Ca^{2+} influx was inhibited by the Piezo1 inhibitor; (c & d) Removing extracellular Ca^{2+} did not rescue the compressive force-induced impairment of cementoblasts migration and mineralization. Values are expressed as mean ± SD: ns (not significant); *p < 0.05, **p < 0.01, ***p < 0.001, ****p < 0.001.*

7.16 LMCD1 and POSTN are Potential Downstream Targets of Piezo1

To explore Piezo1 downstream targets in OIIRR, we identified 1,368 differentially expressed genes (DEGs) regulated by compressive force and 384 DEGs influenced by the Piezo1 activator through RNA-seq analysis. A Venn diagram revealed 149 DEGs regulated by both factors, as shown in the heat map (Figure 19a & b). Among these, we focused on periostin (POSTN) and LIM and cysteine-rich domains 1 (LMCD1) due to their potential relevance to OIIRR.

POSTN, a matricellular protein, is a secreted adhesion-related molecule localized in the periodontal ligaments and periosteum. It plays a pivotal role in the formation and maintenance of teeth, bones, and other collagen-rich connective tissues under mechanical stress, such as heart valves and tendons [104, 105]. Similarly, LMCD1 is known to regulate osteogenic differentiation [106] and migration [107], two essential cellular processes involved in cementum repair.

qRT-PCR and Western blot analyses confirmed that both compressive force and the Piezo1 activator increased LMCD1 expression while suppressing POSTN expression (Figure 19c & d). Interestingly, while the Piezo1 inhibitor reversed the protein-level effects of compressive force, it did not affect LMCD1 or POSTN transcription. These findings suggest that LMCD1 and POSTN are downstream targets of Piezo1 and may

represent potential therapeutic targets for OIIRR. However, further research is required to develop effective regulatory strategies.

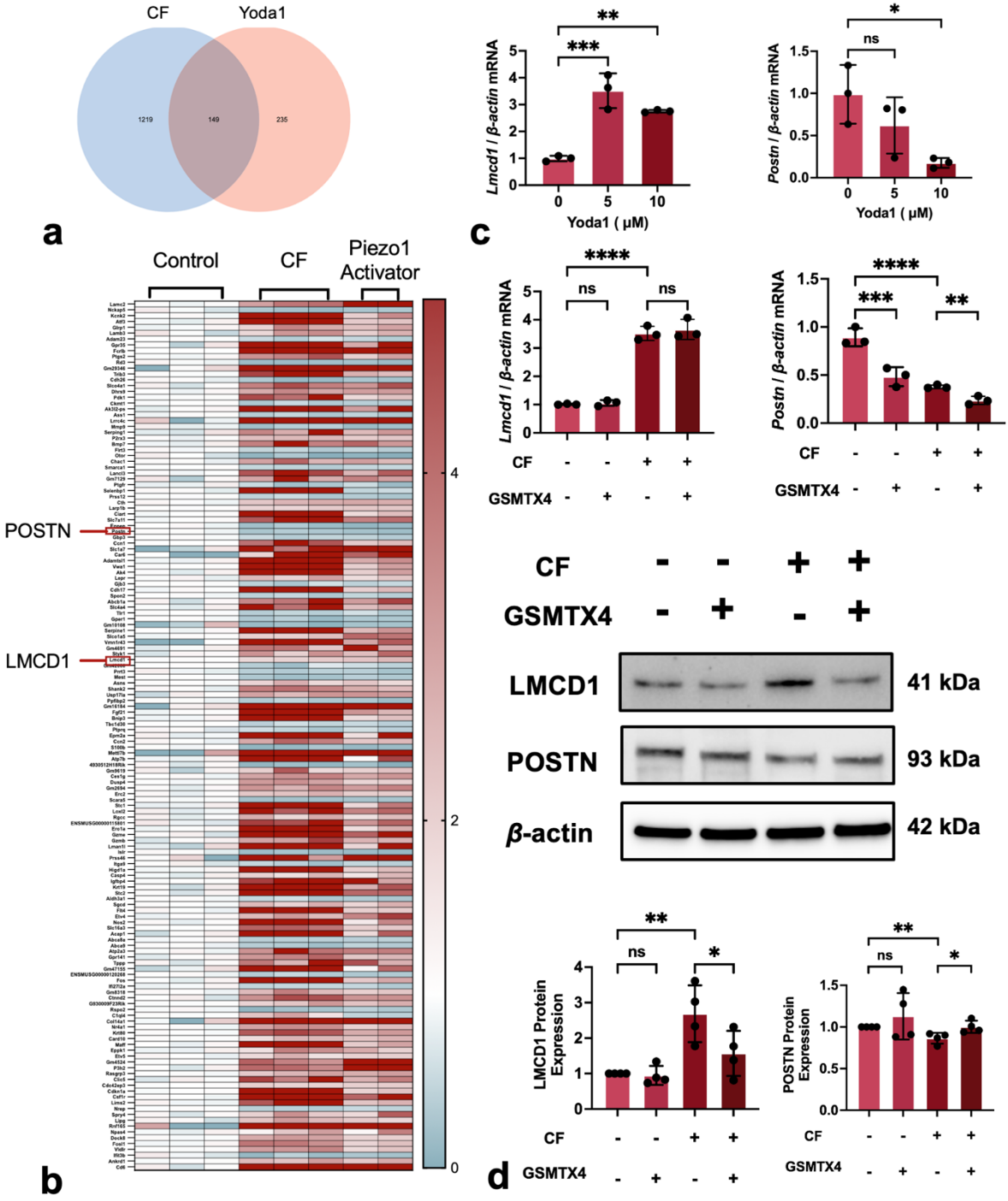

Figure 19. *LMCD1 and POSTN were identified as Piezo1 downstream targets in OIIRR.*

(a & b) The Venn diagram and heat map highlight DEGs co-regulated by compressive force and Yoda1; (c) Yoda1 increases LMCD1 mRNA levels while suppressing POSTN mRNA expression; (d) GSMTX4 reverses the effects of compressive force on LMCD1 and POSTN protein expression but does not impact the gene transcription. Values are expressed as mean ± SD: ns (not significant); *$p < 0.05$, **$p < 0.01$, ***$p < 0.001$, ****$p < 0.001$.

8. Discussion

As excessive orthodontic force is a key risk factor for orthodontically induced inflammatory root resorption (OIIRR), it is essential to understand the effects of compressive force on teeth and periodontal tissues at both cellular and molecular levels. The pathogenesis of orthodontically induced inflammatory root resorption (OIIRR) is fundamentally characterized by a disruption in the dynamic balance between cementum destruction and repair. However, the underlying causes of this imbalance remain unclear. This study focuses on cementoblasts—the primary cells responsible for cementum repair—and aims to investigate the mechanisms by which their reparative capacity is impaired under compressive stress. To this end, two hypotheses are proposed: (1) compressive force induces an excessive innate immune response that leads to cementoblast dysfunction, and (2) compressive force directly suppresses the reparative function of cementoblasts, independent of immune modulation. Consequently, the research focused on macrophages and cementoblasts, exploring their responses to compressive force and potential interactions.

Furthermore, considering that cellular mechanosensation plays a pivotal role in various physiological and pathological processes, understanding the mechanisms of mechanotransduction is of critical importance. Our findings have identified three distinct intracellular mechanotransduction pathways (Histone H3 acetylation, Lamin A/C and Piezo1) as potential therapeutic targets for mechanically induced diseases.

8.1 Macrophages

8.1.1 Compressive Force Induces Deformation of the Macrophage Nucleus, rather than Overall Cell Structure

As mechanosensitive cells, macrophages can perceive various mechanical signals and convert them into biochemical signals, influencing the microenvironment, inflammatory response, and tissue homeostasis [22]. Previous studies have shown that

macrophages elongate on rough extracellular matrix surfaces, exhibiting reduced adhesive capacity and suppressed pro-inflammatory cytokine expression [57, 108]. This morphological alteration of overall cell is believed to couple mechanical stimulation and downstream functional output by rearranging the actin cytoskeleton, the Golgi complex, and the cation channel receptor transient receptor potential melastatin 2 (TRPM2) [109].

In contrast, our compressive model revealed significant macrophage polarization without observable overall morphological changes (Figure 4c & 5). This difference may arise from the hydrostatic pressure we applied, which exerted a uniformly distributed force on the cell membrane, directed toward the center of the cell. This is in contrast to the tensile forces induced by a rough extracellular matrix. This difference also explains why our model upregulated pro-inflammatory factors, rather than downregulating them as observed with rough matrix stimulation. It was also demonstrated that macrophages sense hydrostatic pressure through mechanisms independent of morphological alterations, highlighting a distinct mechanotransduction pathway.

Interestingly, our data showed that force caused marked nuclear shrinkage, accompanied by the formation of large amounts of heterochromatin (Figure 4c). Stephens et al. (2019) [110] observed a similar phenomenon in mesenchymal stem cells. These highly condensed chromatin structures were believed to increase nuclear stiffness against compression, thereby reducing nuclear rupture and DNA damage. Meanwhile, heterochromatin has lower transcriptional activity; therefore, the condensation of this chromatin may be one of the mechanisms by which mechanical forces regulate gene transcription [111].

Meanwhile, we observed that cells exhibiting excessive heterochromatin formation showed a lower proportion of S-phase, indicating reduced proliferative viability (Figure 4d). This was also supported by our related viability assay (Figure 10e). The

stabilization of heterochromatin has been widely reported to be associated with cellular aging and proliferation arrest [112-115]. However, a limitation of our study is the inability to confirm a direct causal relationship between mechanically induced heterochromatin condensation and inhibition of proliferation.

Another interesting observation is that some heterochromatin was co-localized with the inner nuclear envelope and vesicles. It remains unclear why these condensed chromatins adhere to the nuclear envelope. However, the 'vesicle-like' structures observed within the heterochromatin offer a potential explanation; this adhesion may facilitate the exchange of heterochromatin components with the extranuclear environment.

For investigating the effects of compressive force on gene transcription, the expression levels of *Nos2*, *Il1b*, *Arg1*, *Il10*, were analyzed using qRT-PCR. *Nos2* and *Il1b* are well-established markers of LPS-induced M1 polarization. Our results show that compressive force promotes M1 polarization, amplifying inflammation. This finding aligns with reports by He et al. (2015) [12], Fang et al. (2022) [116] and Zhang et al. (2020) [41]. Typically, ARG1 hydrolyzes arginine into ornithine and urea, a hallmark of M2 polarization, which is antagonized by the metabolic pathway involving iNOS [117]. Similarly, IL-10 is also thought to act in opposition to iNOS, and the two jointly contribute to the regulation of inflammatory responses [118]. Interestingly, our study observed an increase in *Arg1* and *Il10* expression under compressive force. According to updated definitions, macrophage polarization is heterogeneous, with M1 and M2 phenotypes being dynamic, overlapping, and interconvertible [119]. We hypothesize that the simultaneous upregulation of M1 and M2 markers during the later stages reflects macrophage heterogeneity. This is supported by single-cell sequencing studies in mouse models, which show that macrophages activated by orthodontic force do not exhibit a single phenotype but instead form diverse cell clusters [28]. This heterogeneity of macrophages may

represent a compensatory mechanism to limit excessive inflammatory responses under mechanical stress.

Notably, *Nos2* is the first marker to respond to mechanical stimulation, preceding *Arg1* and *Il-10* (Figure 5). This suggests that macrophages initiate inflammation during the early stages of compression but subsequently regulate the immune response and facilitate tissue repair after 24 hours. Similar to macrophage activation by biochemical stimuli, M1 macrophages drive inflammation during the acute phase, while M2 macrophages mediate resolution of inflammation and tissue repair at later stages [120, 121]. In summary, compressive force can effectively drive macrophage polarization, highlighting its dual role in orthodontic-induced tissue remodeling.

It is well-documented that adiponectin regulates macrophage polarization through AMPK, NF-κB, and PPAR-γ signaling pathways [43, 122-126]. However, our results indicate that polarization markers upregulated by compressive force do not respond to adiponectin. To further explore whether adiponectin influences mechanically activated macrophages, we performed bioinformatic analysis. This analysis revealed that *Saa3* and *ApoE* are upregulated under compression and may be linked to adiponectin (Figure 6a & b). SAA3 is an acute-phase protein [127], and APOE is known to regulate osteoclast activity, lipid metabolism, and inflammation [128, 129]. However, their roles in OTM remain unclear. Further validation using qRT-PCR confirmed that both *Saa3* and *ApoE* were significantly enhanced by compressive force but showed no response to adiponectin. These findings indicate that compressive force triggers macrophage activation *via* a distinct, non-canonical pathway that does not require the adiponectin receptor, setting it apart from classical stimuli such as LPS, IFN-γ, and IL-4.

In summary, these evidence highlights that compressive force significantly affects macrophage nuclei and regulates both proliferation and polarization. Understanding of the underlying mechanism will provide valuable insights into the regulation of OTM

and other mechanically associated pathophysiological processes, paving the way for targeted therapeutic interventions.

8.1.2 Histone H3 Acetylation Mediates M2 Polarization

The role of epigenetics in mechanical sensation has gained increasing attention in recent years. Acetylation and deacetylation are key chemical modifications on histones that are closely linked to gene expression and gene silencing [130]. It has been demonstrated that histone H3 acetylation (H3ac) is associated with IL-10 expression in force-stressed periodontal ligament (PDL) fibroblasts [131]. Our research confirmed that H3ac is significantly elevated under compressive force.

Bromodomain and extraterminal domain (BET) proteins are well-known readers of H3ac. They bind to relaxed chromatin regions marked by acetylated histones, acting as scaffolds on euchromatin to facilitate the binding of transcription elongation factors, transcription factors, and other coactivators [132]. IBET762, a specific inhibitor of BET proteins that competes with H3ac for BET binding, significantly suppressed the expression of *Il10* and *Arg1*, while having no notable effect on *Nos2* (Figure 7d-g). These findings suggest that compression induces macrophage anti-inflammatory polarization through histone H3 hyperacetylation (Figure 20). This result aligns with the conclusions of Jain et al. (2018), who proposed that spatial confinement reduces the inflammatory response of macrophages [24]. However, in contrast to our findings, research by Veerasubramanian et al. (2021) reported that mechanical stimulation reduced histone H3 acetylation [57]. It could be the case because they used micropatterns as mechanical stimuli, which elongated the cell membrane and cytoskeleton, unlike our hydrostatic compressive force. Nevertheless, the role of H3ac in macrophage mechanosensation remains critical.

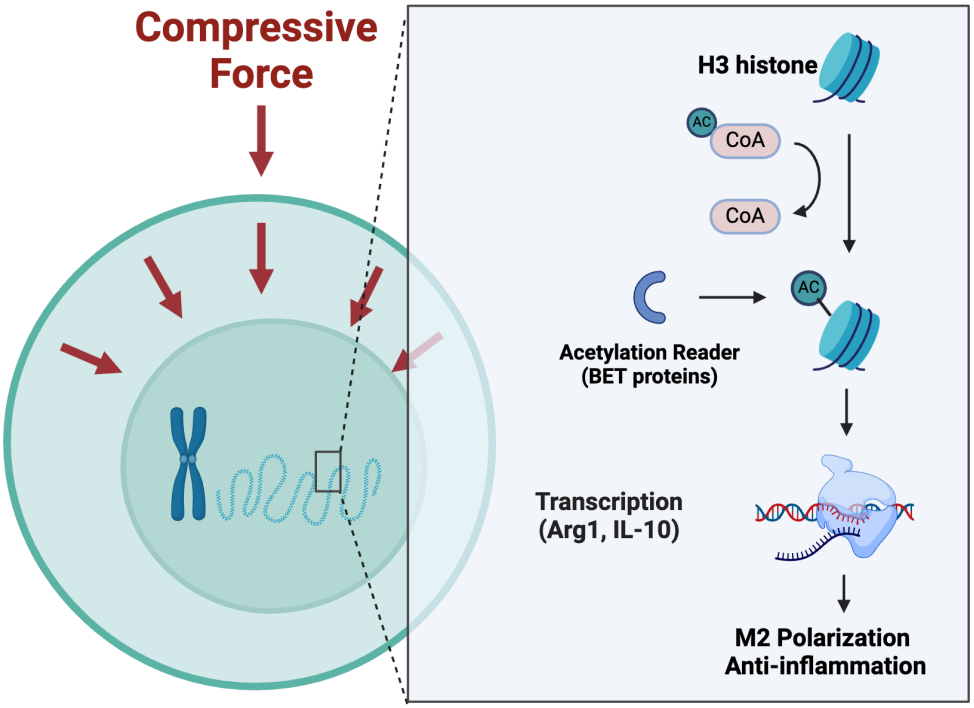

Figure 20. *Compressive force enhances H3 histone acetylation to promote M2 polarization.*

8.1.3 Mechanic-Induced Lamin A/C Deficiency Increases Nuclear Permeability

This study clearly identified that the compression inhibited the lamin A/C protein level (Figure 8a & c), aligning with the results of the studies by Chambliss et al. (2013) [133] and Fu et al. (2023) [134]. Interestingly, in different cell lines, lamin A/C seem to respond differently, or even oppositely, to mechanical force. Maremonti et al. (2022) [135] observed contrasting responses in two different human epithelial cell lines (MDA-MB-231 and MCF-10A) subjected to the same mechanical stimulation, with an increase in MCF-10A cells but a decrease in MDA-MB-231 cells.

Anyway, our study demonstrated that macrophages (RAW264.7) responded to compressive force *via* reducing lamin A/C, and this reduction was cytoskeleton-dependent (Figure 8f). It suggests that force is transmitted along the cytoskeleton to reach the lamina.

Moreover, this force-induced lamin A/C deficiency was not constant. Western blot analysis showed that lamin A/C levels were inhibited after 1 hour but completely recovered after 6 h (Figure 8a). Lamin A/C deficiency induced by *siRNA* was also recovered after 72 h at both the gene and protein levels (Figure 9a & b). Considering that lamin A undergoes periodic dynamic changes throughout the cell cycle [63, 136, 137], we suggest that the cell has a lamin A/C repair mechanism. Specifically, compressive force impairs lamin A/C in the early stage, and a repair mechanism is subsequently initiated to rescue the lamin A/C level and to re-strengthen nuclear stiffness for resistance against external pressure. It was reported that the *LMNA*-mRNA expression level depends on the existing amount of *LMNA*-related proteins [138], providing further support for our repair mechanism theory. This theory may help explain the temporal variation in macrophage responses to compressive force, as the protein level of the mechanosensitive effector, lamin A/C, fluctuates—initially decreasing after mechanical stimulation, followed by recovery mediated by cellular repair mechanisms. It further explains why distinct cell lines exhibit contrasting responses of lamin A/C to the same mechanical stimulation. We propose that the repair mechanism may overcompensate in those up-regulation cases.

The role of lamin A/C on cells in mechano-transduction was in the focus of this study. First, lamin A/C level was believed to determine nuclear rigidity [139]. After 1 hour of force loading, lamin A/C decreased and nuclear deformation occurred concurrently (Figure 8a-d). Meanwhile, *LMNA* knockdown enhanced compressive force-induced nuclear deformation (Figure 10c & 11b). These findings align with observations that fibroblasts that lack lamin A/C face an increased risk of nuclear rupture under

compression [82, 83], supporting the conventional theory that lamin A/C, serving as the nuclear scaffold, counteracts mechanical pressure's impact on the nucleus [140, 141].

Due to the transient nature of force-induced lamin A/C deficiency, we employed *siRNA* to induce lamin A/C deficiency for longer periods to conduct other gene and protein analysis. Our data showed that *LMNA* was silenced from post-transfection 24-48 h (Figure 9a-c). Whereas, sR *LMNA* can completely rescue lamin A/C protein level (Figure 9d).

The lamin A/C deficiency caused nuclear envelope impairment and increased nuclear permeability (Figure 9f & g). This increased permeability coincided with enhanced nuclear translocation of YAP1 (Figure 10c). YAP1 is a classic mechanical response protein. Numerous studies have shown that it mediates the mechanotransduction by translocating into the cellular nucleus [142-147]. YAP1 can modulate cellular inflammation [94] and proliferation [148]. Thus, we detected expressions of inflammatory genes (*Arg1*, *Il10*, and *Nos2*) and the cellular proliferative ability using qRT-PCR and viability assay (Figure 10d & e). The results showed that deficient lamin A/C levels significantly enhanced the effects of force on macrophage, including induction of polarization and inhibition of proliferation. These results suggested that deficient lamin A/C plays a positive role in mechanotransduction by increasing the nuclear permeability and YAP1 translocation.

Interestingly, apart from limiting the nuclear translocation of YAP1, lamin A/C did also regulate its protein level. The classical regulatory mechanism of YAP1 is the Hippo signaling pathway [149]. Briefly, the Hippo signaling pathway is initiated when the large tumor suppressor kinase 1/2 (LATS1/2) complex is phosphorylated, leading to the downstream phosphorylation of YAP1. Phosphorylated YAP1 binds to 14-3-3 proteins and is eventually degraded in the cytoplasm. When the Hippo signaling pathway is 'turned off,' non-phosphorylated YAP1 —also referred to as

active YAP1—translocates into the nucleus and triggers genes transcription. However, what cannot be explained by the classical modulation theory is that, in our experiments, although either force or lamin A/C deficiency can upregulate non-phosphorylated YAP1 levels, it does not increase its nuclear translocation. Only under the combined action of compressive force and lamin A/C deficiency significant nuclear translocation of YAP1 occurs (Figure 10c). Thus, we proposed a model to explain regulated mechanisms of YAP1 translocation by compressive force and lamin A/C (Figure 21). Specifically, compressive force provided an unknown initiating factor, and deficient lamin A/C levels induced nuclear envelope impairment to permit translocation. There are many possible explanations for the exact nature of this unknown initiation signal. Here are two hypotheses we propose: a). compressive force probably stretches nuclear pores, enhancing YAP1 nuclear translocation [150, 151]; b). mechanical clues may be necessary for the recognition of importin, a nuclear transport carrier, to recognize the nuclear localization signal (NLS) of YAP1. However, a more definitive conclusion cannot be drawn until more relevant research results are revealed.

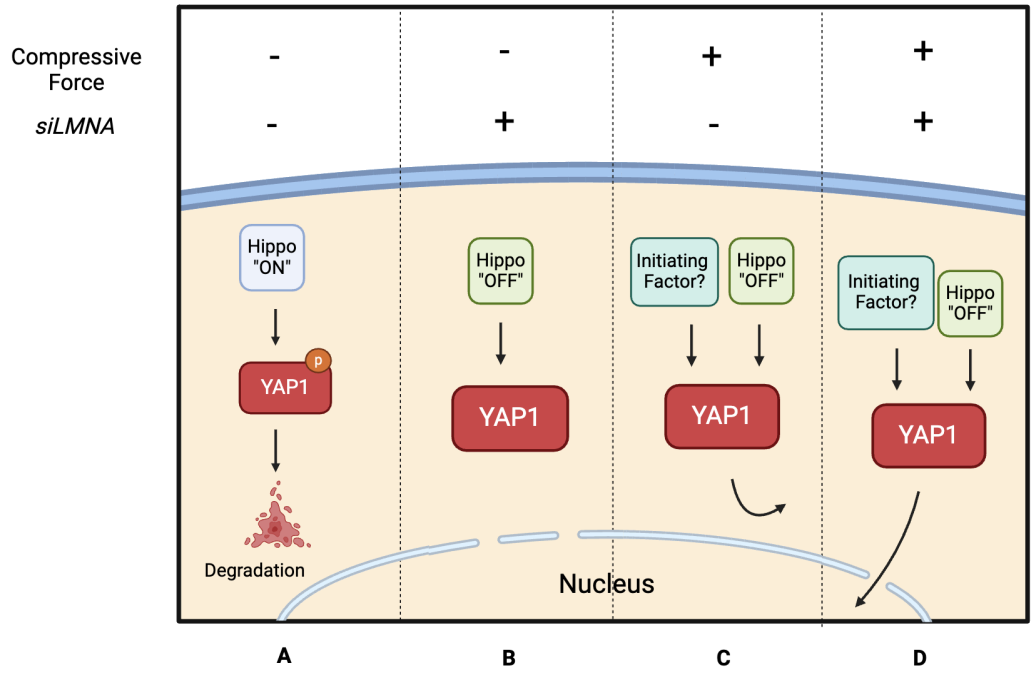

Figure 21. *A simplified schematic diagram illustrates the regulation of YAP1 translocation in four different states*

A: In the physiological state, the Hippo pathway phosphorylates (inactivates) YAP1, leading to its degradation in the cytoplasm.

B: Although siLMNA interferes with YAP1 phosphorylation, YAP1 cannot translocate into the nucleus due to the absence of the "initiating factor" associated with compressive force.

C: Due to the mechanical impedance of lamin A/C, activated YAP1 accumulates in the cytoplasm.

D: Compressive force drives the activated YAP1 to translocate into the nucleus, overcoming the deficiency in lamin A/C.

Another significant effect of lamin A/C deficiency is its role in regulating migration. Knockdown of lamin A/C *via siLMNA* significantly enhances macrophage migration (Figure 10a). In mesenchymal stem cells, reduced levels of lamin A/C contribute to a softer nuclear structure, thereby facilitating migration [59]. A similar phenomenon has been observed in breast cancer cells [152], aligning with our data. However, while compressive force can also decrease lamin A/C levels, it fails to promote cell migration. We hypothesize that this may be due to compressive forces triggering other factors that counteract migration, such as hypoxia.

On the other hand, we also found that lamin A/C deficiency has negative impacts on mechano-transduction. We observed that lamin A/C deficiency induced detachment of the LINC complex from the nuclei (Figure 11b & c). The LINC complex forms a physical connection between cytoskeleton and nucleoskeleton, which transduces the mechanical signals from the environment to the nuclei [70]. The LINC complex consists of an outer nuclear membrane, the KASH domain protein and an inner nuclear membrane SUN domain protein. SUN1 and SUN2 constitute the inner nuclear

membrane (INM) component of the LINC complex, interacting with lamina and connecting with the KASH domains of nesprins in the perinuclear space (PNS) [153, 154]. Some scholars have reported that the deletion of lamin A/C impairs the nuclear localization of SUN2 [155, 156], which is consistent with our findings. Whereas its effects on SUN1 is controversial. Chiarini et al. (2022) [157] and Mattioli et al. (2011) [158] reported that the presence of lamin A/C is significantly proportional to the nuclear localization of SUN1, but Haque et al. (2010) [156] reported that lamin A/C did not affect SUN1 localization and believed SUN1 was anchored on the nucleus by binding to chromatin rather than the lamina. Differing conclusions may be due to different cell lines that were used. Anyway, our data clearly demonstrated that deficient lamin A/C levels caused detachment of SUN1 and SUN2 from nuclei, impeding mechano-transduction (Figure 11b & c). Considering deficient lamin A/C can be caused by compressive force in the early stage, we believe that this negative feedback loop represents a cellular self-protective mechanism from excessive mechanosensation. A convincing piece of evidence is that some effects of compressive force can be inhibited by lamin A/C deficiency, such as IRF4 expression, DNA damage and enhanced phagocytosis induced by compressive force (Figure 12).

Finally, the unexpected finding was that SUN1 and SUN2 were significantly inhibited by compressive force (Figure 11a). The inhibition of SUN2 (57 %) is even more significant compared to lamin A/C (34 %). Gilbert et al. (2019) [72] reported that another form of mechanical stimulation, cyclic tensile strain (CTS), can also downregulate the SUN2 expression. Three CTS-sensitive phosphorylation sites on the lamin-binding domain of SUN2 have been identified, which may induce the rapid loss of SUN2. This SUN2 loss disrupts mechano-transmission between the cytoskeleton and the nucleus, thereby protecting chromatin. On the other hand, evidence suggests that SUN proteins regulate downstream processes such as histone methylation,

cytoskeletal metabolism, and DNA repair [72, 159, 160]. Therefore, we propose that the SUN proteins may couple mechanical stimulation with these biological processes, not only by serving as a mechanical linker but also through direct interactions with chromatin and the regulation of gene expression.

This study elucidates that compressive force transiently down-regulates macrophage lamin A/C levels. This transient downregulation impairs the nuclear envelope and increases nuclear permeability to YAP1, subsequently enhancing force-induced cytokine expression and proliferative inhibition. Meanwhile, it also reduces force-induced IRF4 expression, DNA damage and enhancement of phagocytosis, probably due to the disrupted LINC complex. These two downstream effects play antagonistic roles in mechanotransduction, jointly regulating cellular behavior under pressure (Figure 22).

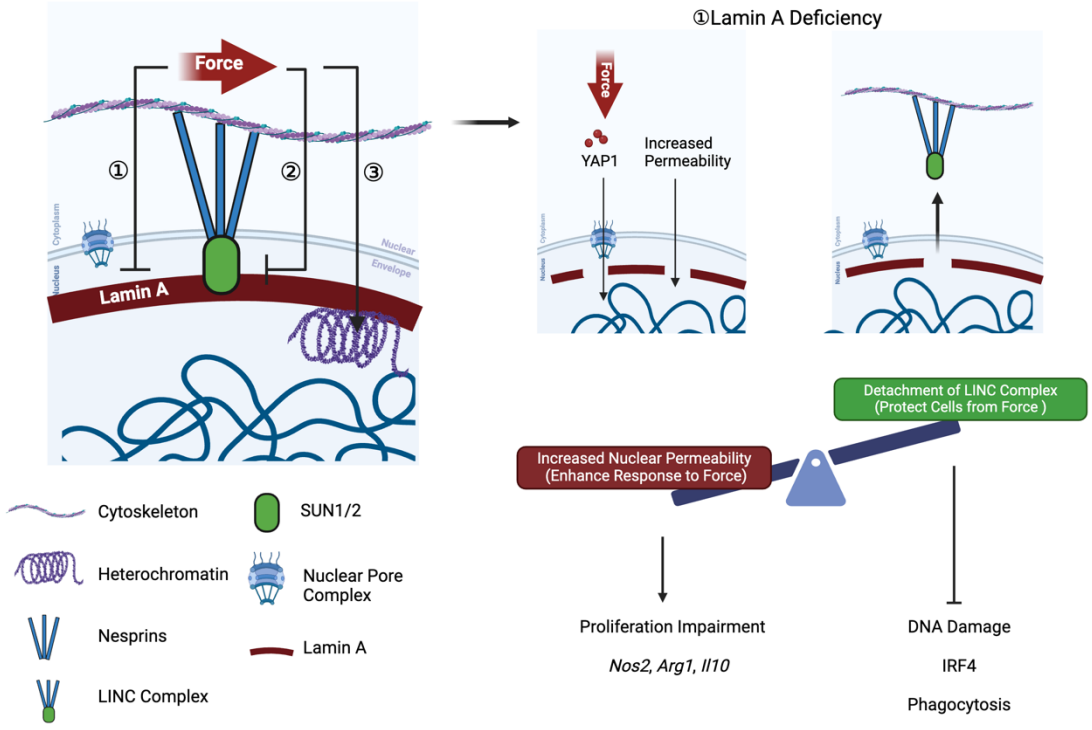

Figure 22. *Lamin A/C is involved in macrophage mechanotransduction through two opposing regulatory pathways.*

Firstly, compressive forces reduce lamin A/C levels, thereby increasing nuclear permeability to transcription factors. Secondly, insufficient lamin A/C disrupts the transmission of mechanical signals by impairing the attachment of the LINC complex to the nuclear membrane.

8.2 Cementoblasts

8.2.1 Cementoblasts Respond to Compressive Force, Instead of Mechanically Activated Macrophages

To investigate the cementum-immune interaction, conditioned medium from force-activated macrophages was collected to treat cementoblasts. In contrast to our expectations, although compression significantly influenced macrophages, their conditioned medium had no effect on cementoblasts. This contradicts previous observations that M1 polarization is positively correlated with root resorption in mice [12]. We believe there are two potential reasons for this contradiction: 1) although M1 polarization was promoted in the early stage, the upregulation of M2 in the later stage may offset the effects of M1; 2) under *in vivo* condition, other mechanically sensitive cells, such as periodontal ligament cells (PDLCs), are involved in root resorption, and their contributions were not addressed in our *in vitro* study.

However, direct compressive stimulation led to impaired migration and reduced *Opg* expression in cementoblasts, indicating that, like PDLCs and macrophages, cementoblasts are also mechanically sensitive cells (Figure 13a & b). This conclusion is further supported by RNA-seq results (Figure 14), which identified over 6,000 DEGs in response to compressive force. Enrichment analysis of these DEGs revealed that compressive force significantly affects two key cellular functions: hypoxia (or angiogenesis) and mineralization (Figure 14c). However, a limitation of this study is that we cannot determine whether the effects of compressive force on

hypoxia/angiogenesis-related genes are direct or indirect. Similar to real biological tissues, compressive force in our model reduces fluid or air exchange, making it difficult to isolate the effects of compressive force from the accompanying decrease in oxygen levels. Therefore, an *in vitro* model that can apply static pressure to cells while maintaining oxygen levels is still needed.

8.2.2 Compressive Force Induces Angiogenesis and Inhibits Mineralization through Piezo1 in Cementoblasts

Mechanistically, we detected an increased Piezo1 mRNA level in these cementoblasts subjected to compression (Figure 13c), which is a mechanically gated ion channel [161]. The Piezo1 inhibitor GSMTX4 was employed to treat cementoblasts. A significantly dampened effect of force on the *Opg* mRNA expression was demonstrated. Thus, we hypothesize that Piezo1 mediates mechanical signal transmission in cementoblasts.

We confirmed that Piezo1 is expressed on the surface of cementoblasts (Figure 15a & b). Furthermore, treatment with 5 and 10 μM Piezo1 activator inhibited cellular migration, consistent with the findings by Yu et al. (2023) [162] and Zhu et al. (2023) [163], who reported similar effects in breast cancer cells and microglia, respectively. The underlying mechanisms remain unclear but may be related to increased cell stiffness and contractility [162]. Additionally, Holt et al. (2023) observed that Piezo1 activation in keratinocytes causes retraction during migration, thereby slowing wound healing [164]. This intriguing research suggests that Piezo1 may regulate not only the speed of migration but also the direction. Further studies are warranted to elucidate these mechanisms. Notably, the effect of Piezo1 activation on migration appears to vary between cell types. For instance, activation of Piezo1 has been shown to enhance migration in neutrophils [165] and T cells [166], which contrasts with our findings. This highlights the cell type-specific nature of Piezo1's role in migration.

Previous studies have highlighted the positive role of Piezo1 in promoting the proliferation of macrophages [23, 167], fibroblasts [168], carcinoma cells [148] and astrocytes [169]. Surprisingly, we found that cementoblasts proliferation was unaffected by low concentrations of Piezo1 activator (5 and 10 μM) but was significantly suppressed at higher concentrations (20 μM) (Figure 15b). This observation aligns with the properties of cementum, which resists mild mechanical stimulation but is susceptible to damage under excessive mechanical force.

KEGG pathway analysis revealed that the DEGs induced by pharmacological activation of Piezo1 were primarily enriched in the HIF-1 signaling pathway, a hallmark of hypoxia signaling (Figure 16a). This finding aligns with the results of GO analysis, which showed that compressive force upregulated hypoxia-related genes. Further protein and gene assays confirmed that compressive force upregulates HIF-1α and its downstream vascularization-related genes, including *Vegf*, *Angpt1*, and *Angptl4*, through Piezo1 activation (Figure 16c & d). Numerous studies have reported that Piezo1 plays a significant role in regulating hypoxia and angiogenesis [170-174], processes that are considered critical during the early stages of bone repair [175-177]. However, for cementum repair, reports on the role of hypoxia remain contradictory [178, 179]. While some studies have shown that hypoxia impairs cementoblasts mineralization [180-182], others have reported positive effects [122, 183]. We believe this discrepancy may be caused by the heterogeneity of the methods used to induce hypoxia and the varying degrees of hypoxia during these studies. In summary, compressive force induces hypoxia/angiogenesis through Piezo1, although whether this activation has a positive or negative effect on OIIRR remains unknown. More precise and reproducible methods for hypoxia induction, along with relevant animal experiments, need to be further developed in future studies.

On the other hand, compressive force inhibits cementoblasts mineralization through Piezo1. Notably, different mineralization markers exhibited varying sensitivities to

mechanical stimulation (or Piezo1 activation). Among all the markers we assessed, SP7 is the most responsive to both compressive force and Piezo1 activation, while BMP2 only responds to Piezo1 activation and not to compressive force (Figure 17b & d). Therefore, we propose that SP7 is a valuable marker for OIIRR and may play a crucial role in this process.

SP7, also known as OSX, has long been recognized as a key factor in both skeletal and cementum formation. While SP7 is expressed in both the tooth crown and root, its deletion affects the formation of the root but not the crown [184, 185]. Feng et al. (2015) proposed that this discrepancy may be due to the function of SP7 being compensated by other factors in the crown, whereas such compensation fails in root formation [185]. However, the exact compensatory mechanisms remain unclear, and investigating whether compensatory SP7 expression can prevent or even reverse OIIRR presents a promising research direction.

8.2.3 LMCD1 and POSTN are Downstream Mediators of Piezo1, Likely Regulating Cementum Repair

Piezo1 is widely recognized as a cation ion channel permeable to both monovalent and divalent ions [100]. Among its downstream mediators, Ca^{2+} is the most extensively studied. Our data confirmed that intracellular Ca^{2+} levels increase in response to compressive force but can be mitigated by a Piezo1 inhibitor (Figure 18a & b). To further explore the role of downstream Ca^{2+} signaling in cementoblasts, we employed a Ca^{2+}-free medium. Surprisingly, excluding Ca^{2+} influx did not reverse the effects of compressive force on migration or mineralization (Figure 18c & d). This suggests that the functional alterations of cementoblasts induced by Piezo1 are mediated through mechanisms independent of Ca^{2+}. Recent studies have shown that Piezo1 can mediate iron influx to promote ferroptosis [186], highlighting the involvement of other downstream mediators in Piezo1-related functions.

On the other hand, according to the Venn graphic, a total of 149 DEGs were regulated by both compressive force and Piezo1 activator (Figure 19a). Heat map illuminates the effects of compressive force and Piezo1 activator on these DEGs (Figure 19b). Among all of DEGs, we focused on POSTN and LMCD1, as their known biological functions are closely linked to OIIRR.

Compressive force and an Piezo1 activator can significantly reduce the POSTN protein level (Figure 19c & d), which plays a positive role in postnatal tooth mineralization. Ma et al. (2011) reported that POSTN is expressed in the ameloblast cells, and an enamel defect is identified in POSTN-null adults [187]. Yang et al. (2023) reported that POSTN/β-catenin is the mediator of autophagy and mineralization in mice cementoblasts, enhancing mineralization by regulating Wnt signaling [15]. Its effect on human OIIRR needs further exploration.

Additionally, we found that the Piezo1 activator and compressive force significantly up-regulated LMCD1 (Figure 19c & d). This protein is a co-regulator which has been intensively studied in the area of carcinoma. For instance, LMCD1 can regulate hepatocellular carcinoma growth, collagen deposition, metastasis and migration [107, 188]. Recently, it was recognized to regulate cellular function of mechanically sensitive tissue, such as skeletal muscle [189], myofibroblast [190] and smooth muscle [191]. Most importantly, Zhu et al. (2018) found that LMCD1 promotes osteogenic differentiation of human bone marrow stem cells by regulating BMP signaling [106]. Thus, we assume that LMCD1 and POSTN are downstream mediators of Piezo1 and likely potential therapeutic targets of OIIRR.

In conclusion, compressive forces can regulate various cellular functions and signaling protein through Piezo1 in cementoblasts, as summarized in Figure 23.

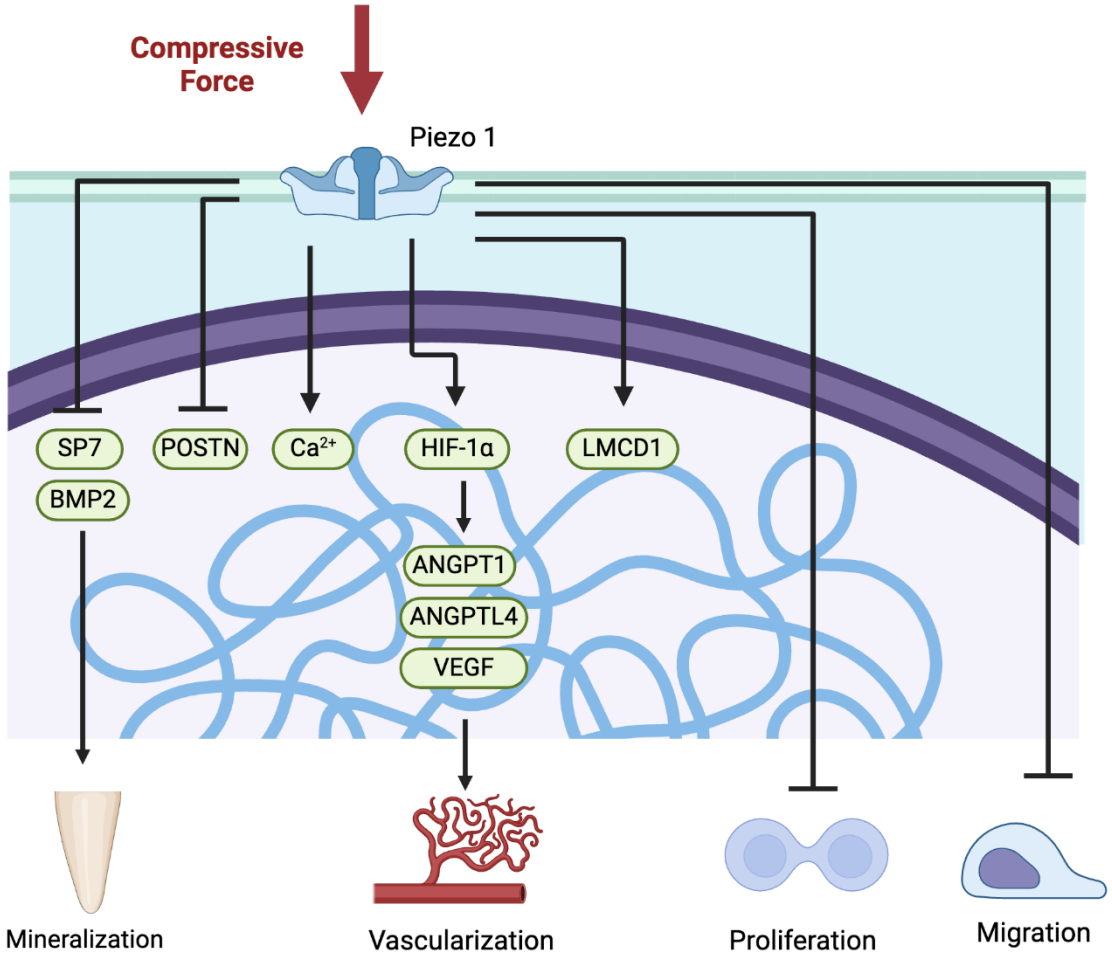

Figure 23 *Compressive force regulates cementoblast functions via Piezo1. Compressive force can activate Piezo, initiating downstream Ca^{2+}influx, HIF-1α signaling, and LMCD1, while inhibiting SP7, BMP2 and POSTN proteins. This regulation influences key cellular functions, including mineralization, vascularization, proliferation, and migration.*

9. Conclusions

This study investigated the impact of orthodontic compressive forces on immune cell responses within periodontal tissues and cementum metabolism, as well as the interplay between these processes. Our findings revealed three key insights:

Firstly, orthodontic compressive forces regulated macrophage immune responses by promoting H3 histone acetylation and reducing lamin A/C protein levels, thereby influencing the cellular immune environment. Secondly, compressive forces impaired cementoblasts function by activating the mechanosensitive receptor Piezo1, highlighting a direct effect on cementum-forming cells. Lastly, since cementoblasts primarily responded to mechanical forces rather than signals from macrophages, we propose that the primary pathological factor driving orthodontically induced inflammatory root resorption (OIIRR) is the mechanical force itself, rather than the secondary inflammation it induces.

This study comprehensively evaluated the effects of compressive forces on both cementoblasts and macrophages, providing detailed insights into three distinct intracellular mechanotransduction pathways. These findings significantly advance our understanding of OIIRR, a common orthodontic complication, and identified potential mechanotransduction mechanisms as therapeutic targets for the prevention of OIIRR and other mechanically induced conditions in the future.

10. Summary

This study analyzes the impacts of orthodontic compressive force on both innate immune responses and cementum homeostasis (Figure 22).

In macrophages, compressive force induces chromatin rearrangement, nuclear shrinkage, and polarization. Two distinct mechanotransduction pathways were identified:

1. Histone H3 hyperacetylation: This mediates M2 polarization during the late stage of the immune response.

2. Lamin A/C downregulation: Orthodontic compressive force transiently reduces lamin A/C levels, compromising the nuclear envelope and increasing nuclear permeability to YAP1. This facilitates enhanced force-induced cytokine expression and proliferative inhibition. Concurrently, it reduces force-induced IRF4 expression, DNA damage, and phagocytosis enhancement, likely due to LINC complex disruption. These opposing effects of lamin A/C deficiency jointly regulate cellular behavior under compressive force.

Furthermore, cementoblasts respond directly to compressive force but do not respond to macrophage-conditioned medium, suggesting that excessive orthodontic force, rather than macrophage activation, is the primary driver of OIIRR. Mechanistically, Piezo1 activation under force mediates enhanced hypoxia and suppressed mineralization in a Ca^{2+}-independent manner. Lastly, LMCD1 and POSTN were identified as downstream mediators of Piezo1, representing potential therapeutic targets for OIIRR.

11. Zusammenfassung

Im Rahmen dieser Studie wurden die Auswirkungen kieferorthopädischer Druckkräfte auf die angeborene Immunantwort und die Homöostase des Zements untersucht (Abbildung 22).

Bei Makrophagen löst Druckkraft eine Chromatin-Umstrukturierung, Schrumpfung des Zellkerns und Polarisierung der Makrophagen aus. Zwei verschiedene Mechano-Transduktionswege wurden identifiziert:

1. Hyperacetylierung von Histon H3: Dieser Vorgang vermittelt die M2-Polarisierung im Zuge der späten Phase der Immunantwort.

2. Herunterregulierung von Lamin A/C: Kieferorthopädische Druckkräfte reduzieren vorübergehend die Lamin-A/C-Spiegel, wodurch die Kernhülle beeinträchtigt und die nukleare Permeabilität für YAP1 erhöht wird. Dies fördert eine verstärkte, durch Kraft induzierte Zytokinexpression und hemmt die Proliferation. Gleichzeitig reduziert es die kraftinduzierte IRF4-Expression, DNA-Schäden und die Intensivierung der Phagozytose, was vermutlich auf eine Zersetzung des LINC-Komplexes zurückzuführen ist. Diese gegensätzlichen Effekte des Lamin-A/C-Mangels regulieren gemeinsam das Zellverhalten unter Druckkräften.

Darüber hinaus reagieren Zementoblasten direkt auf Druckkräfte, zeigen jedoch keine Reaktion auf Makrophagen-konditioniertes Medium, was darauf hinweist, dass übermäßige orthodontische Kräfte – und nicht die Aktivierung von Makrophagen – der primäre Auslöser der orthodontisch induzierten entzündlichen Wurzelresorption (OIIRR) sind. Mechanistisch vermittelt die Piezo1-Aktivierung unter Druck verstärkte Hypoxie und eine Ca^{2+}-unabhängige gehemmte Mineralisierung. Weiterhin wurden LMCD1 und POSTN als die nachgeschalteten Mediatoren von Piezo1 identifiziert. Diese stellen somit potenzielle therapeutische Ansätze für OIIRR dar.

12. References

1. Gao, Y., et al., *Immune System Acts on Orthodontic Tooth Movement: Cellular and Molecular Mechanisms.* BioMed Research International, 2022. **2022**(1): p. 9668610.
2. Yan, Y., et al., *T Cells Are Required for Orthodontic Tooth Movement.* J Dent Res, 2015. **94**(10): p. 1463-70.
3. Noda, K., et al., *Morphological changes in the rat periodontal ligament and its vascularity after experimental tooth movement using superelastic forces.* Eur J Orthod, 2009. **31**(1): p. 37-45.
4. Ciobotaru, C.D., et al., *Enhancement of Orthodontic Tooth Movement by Local Administration of Biofunctional Molecules: A Comprehensive Systematic Review.* Pharmaceutics, 2024. **16**(8).
5. Danz, J.C., et al., *Impact of Orthodontic Forces on Plasma Levels of Markers of Bone Turnover and Inflammation in a Rat Model of Buccal Expansion.* Front Physiol, 2021. **12**: p. 637606.
6. Li, Y., et al., *Biomechanical and biological responses of periodontium in orthodontic tooth movement: up-date in a new decade.* Int J Oral Sci, 2021. **13**(1): p. 20.
7. Yassir, Y.A., McIntyre, G.T., and Bearn, D.R., *Orthodontic treatment and root resorption: an overview of systematic reviews.* Euro J Orthod, 2021. **43**(4): p. 442-456.
8. Weiland, F., *Constant versus dissipating forces in orthodontics: the effect on initial tooth movement and root resorption.* Eur J Orthod, 2003. **25**(4): p. 335-42.
9. Samandara, A., et al., *Evaluation of orthodontically induced external root resorption following orthodontic treatment using cone beam computed tomography (CBCT): a systematic review and meta-analysis.* Eur J Orthod, 2019. **41**(1): p. 67-79.
10. Turkkahraman, H., et al., *Root resorption and ensuing cementum repair by Wnt/β-catenin dependent mechanism.* Am J Orthod Dentofacial Orthop, 2020. **158**(1): p. 16-27.
11. Patel, S. and Saberi, N., *The ins and outs of root resorption.* Br Dent J, 2018. **224**(9): p. 691-699.
12. He, D., et al., *Enhanced M1/M2 macrophage ratio promotes orthodontic root resorption.* J Dent Res, 2015. **94**(1): p. 129-39.
13. Dawood, H.M., et al., *Under pressure-mechanisms and risk factors for orthodontically induced inflammatory root resorption: a systematic review.* Eur J Orthod, 2023. **45**(5): p. 612-626.
14. Weltman, B., et al., *Root resorption associated with orthodontic tooth movement: A systematic review.* Am J Orthod Dentofacial Orthop, 2010. **137**(4): p. 462-476.
15. Yang, Y., et al., *Autophagy mediates cementoblast mineralization under compression through periostin/β-catenin axis.* J Cell Physiol, 2023. **238**(9): p. 2147-2160.
16. Yang, Y., et al., *Compressive force regulates cementoblast migration via downregulation of autophagy.* J Periodontol, 2021. **92**(11): p. 128-138.
17. Li, X., et al., *NLRP3-mediated periodontal ligament cell pyroptosis promotes root resorption.* J Clin Periodontol, 2024. **51**(4): p. 474-486.
18. Liu, H., et al., *Periodontal Ligament Cell Apoptosis Activates Lepr+ Osteoprogenitors in Orthodontics.* J Dent Res, 2024. **103**(9): p. 937-947.

19. Li, Q., et al., *Force-induced decline of FOXM1 in human periodontal ligament cells contributes to osteoclast differentiation.* Angle Orthod, 2019. **89**(5): p. 804-811.
20. Yan, J. and Horng, T., *Lipid Metabolism in Regulation of Macrophage Functions.* Trends in Cell Biol, 2020. **30**(12): p. 979-989.
21. Metchnikoff, E., *Immunity in infective diseases*. 1905: University Press.
22. Maruyama, K., Nemoto, E., and Yamada, S., *Mechanical regulation of macrophage function - cyclic tensile force inhibits NLRP3 inflammasome-dependent IL-1β secretion in murine macrophages.* Inflamm Regen, 2019. **39**: p. 3.
23. Xu, H., et al., *Mechanical force modulates macrophage proliferation via Piezo1-AKT-Cyclin D1 axis*. FASEB J, 2022. **36**(8): p. e22423.
24. Jain, N. and Vogel, V., *Spatial confinement downsizes the inflammatory response of macrophages*. Nat Mater, 2018. **17**(12): p. 1134-1144.
25. Atcha, H., et al., *Mechanically activated ion channel Piezo1 modulates macrophage polarization and stiffness sensing.* Nat Commun, 2021. **12**(1): p. 3256.
26. Alonso-Nocelo, M., et al., *Matrix stiffness and tumor-associated macrophages modulate epithelial to mesenchymal transition of human adenocarcinoma cells.* Biofabrication, 2018. **10**(3): p. 035004.
27. Song, K., et al., *Yes-Associated Protein in Kupffer Cells Enhances the Production of Proinflammatory Cytokines and Promotes the Development of Nonalcoholic Steatohepatitis*. Hepatology, 2020. **72**(1): p. 72-87.
28. Xu, H., et al., *CCR2(+) Macrophages Promote Orthodontic Tooth Movement and Alveolar Bone Remodeling.* Front Immunol, 2022. **13**: p. 835986.
29. Pu, P., et al., *Mechanical force induces macrophage-derived exosomal UCHL3 promoting bone marrow mesenchymal stem cell osteogenesis by targeting SMAD1.* J Nanobiotechnology, 2023. **21**(1): p. 88.
30. Tang, Y., et al., *Mechanosensitive Piezo1 protein as a novel regulator in macrophages and macrophage-mediated inflammatory diseases*. Front Immunol, 2023. **14**: p. 1149336.
31. Mukherjee, P., et al., *Role of mechanosensitive channels/receptors in atherosclerosis*. Am J Physiol Cell Physiol, 2022. **322**(5): p. C927-c938.
32. Lassus, J., et al., *Macrophage activation results in bone resorption.* Clin Orthop Relat Res, 1998(352): p. 7-15.
33. Yang, D. and Wan, Y., *Molecular determinants for the polarization of macrophage and osteoclast.* Semin Immunopathol, 2019. **41**(5): p. 551-563.
34. Wang, C., et al., *Macrophage Polarization and Its Role in Liver Disease.* Front Immunol, 2021. **12**: p. 803037.
35. Yunna, C., et al., *Macrophage M1/M2 polarization.* Eur J Pharmacol, 2020. **877**: p. 173090.
36. Mantovani, A., et al., *Macrophage plasticity and polarization in tissue repair and remodelling.* J Pathol, 2013. **229**(2): p. 176-85.
37. Shapouri-Moghaddam, A., et al., *Macrophage plasticity, polarization, and function in health and disease.* J Cell Physiol, 2018. **233**(9): p. 6425-6440.
38. Hu, K., et al., *Macrophage Polarization and the Regulation of Bone Immunity in Bone Homeostasis.* J Inflamm Res, 2023. **16**: p. 3563-3580.

39. Funes, S.C., et al., *Implications of macrophage polarization in autoimmunity.* Immunology, 2018. **154**(2): p. 186-195.
40. Mi, B., et al., *Osteoblast/Osteoclast and Immune Cocktail Therapy of an Exosome/Drug Delivery Multifunctional Hydrogel Accelerates Fracture Repair.* ACS Nano, 2022. **16**(1): p. 771-782.
41. Zhang, J., et al., *NLRP3 inflammasome mediates M1 macrophage polarization and IL-1β production in inflammatory root resorption.* J Clin Periodontol, 2020. **47**(4): p. 451-460.
42. Achari, A.E. and Jain, S.K., *Adiponectin, a Therapeutic Target for Obesity, Diabetes, and Endothelial Dysfunction.* Int J Mol Sci, 2017. **18**(6).
43. Xu, N., et al., *Adiponectin Ameliorates GMH-Induced Brain Injury by Regulating Microglia M1/M2 Polarization Via AdipoR1/APPL1/AMPK/PPARγ Signaling Pathway in Neonatal Rats.* Front Immunol, 2022. **13**: p. 873382.
44. Brezovec, N., et al., *Adiponectin Deregulation in Systemic Autoimmune Rheumatic Diseases.* Int J Mol Sci, 2021. **22**(8).
45. Haugen, S., et al., *Adiponectin prevents orthodontic tooth movement in rats.* Arch Oral Biol, 2017. **83**: p. 304-311.
46. Bosshardt, D.D., *Are Cementoblasts a Subpopulation of Osteoblasts or a Unique Phenotype?* J Dent Res, 2005. **84**(5): p. 390-406.
47. Chen, J.J., et al., *Altered expression of bone sialoproteins in vitamin D-deficient rBSP2.7Luc transgenic mice.* J Bone Miner Res, 1999. **14**(2): p. 221-9.
48. Iglesias-Linares, A. and Hartsfield, J.K., Jr., *Cellular and Molecular Pathways Leading to External Root Resorption.* J Dent Res, 2017. **96**(2): p. 145-152.
49. Hsia, C.R., Melters, D.P., and Dalal, Y., *The Force is Strong with This Epigenome: Chromatin Structure and Mechanobiology.* J Mol Biol, 2023. **435**(11): p. 168019.
50. Wang, N. and Suo, Z., *Long-distance propagation of forces in a cell.* Biochem Biophys Res Commun, 2005. **328**(4): p. 1133-8.
51. Zhang, D., et al., *Uniaxial Cyclic Stretching Promotes Chromatin Accessibility of Gene Loci Associated With Mesenchymal Stem Cells Morphogenesis and Osteogenesis.* Front Cell Dev Biol, 2021. **9**: p. 664545.
52. Williams, J.F., et al., *The condensation of HP1α/Swi6 imparts nuclear stiffness.* Cell Rep, 2024. **43**(7): p. 114373.
53. Maeshima, K., Tamura, S., and Shimamoto, Y., *Chromatin as a nuclear spring.* Biophys Physicobiol, 2018. **15**: p. 189-195.
54. Schneider, M.W.G., et al., *A mitotic chromatin phase transition prevents perforation by microtubules.* Nature, 2022. **609**(7925): p. 183-190.
55. Nava, M.M., et al., *Heterochromatin-Driven Nuclear Softening Protects the Genome against Mechanical Stress-Induced Damage.* Cell, 2020. **181**(4): p. 800-817.e22.
56. Millán-Zambrano, G., et al., *Histone post-translational modifications - cause and consequence of genome function.* Nat Rev Genet, 2022. **23**(9): p. 563-580.
57. Veerasubramanian, P.K., et al., *A Src-H3 acetylation signaling axis integrates macrophage mechanosensation with inflammatory response.* Biomaterials, 2021. **279**: p. 121236.
58. Danielsson, B.E., et al., *Nuclear lamina strain states revealed by intermolecular force*

biosensor. Nat Commun, 2023. **14**(1): p. 3867.
59. Alcorta-Sevillano, N., et al. *Crucial Role of Lamin A/C in the Migration and Differentiation of MSCs in Bone*. Cells, 2020. **9**, DOI: 10.3390/cells9061330.
60. Osmanagic-Myers, S. and Foisner, R., *The structural and gene expression hypotheses in laminopathic diseases-not so different after all.* Mol Biol Cell, 2019. **30**(15): p. 1786-1790.
61. Al-Saaidi, R. and Bross, P., *Do lamin A and lamin C have unique roles?* Chromosoma, 2015. **124**(1): p. 1-12.
62. Alcorta-Sevillano, N., et al., *Crucial Role of Lamin A/C in the Migration and Differentiation of MSCs in Bone.* Cells, 2020. **9**(6).
63. Swift, J., et al., *Nuclear lamin-A scales with tissue stiffness and enhances matrix-directed differentiation.* Science, 2013. **341**(6149): p. 1240104.
64. Zhang, B., et al., *The role of lamin A/C in mesenchymal stem cell differentiation.* J Physiol Biochem, 2019. **75**(1): p. 11-18.
65. Sapra, K.T., et al., *Nonlinear mechanics of lamin filaments and the meshwork topology build an emergent nuclear lamina.* Nat Commun, 2020. **11**(1): p. 6205.
66. Donnaloja, F., et al., *Lamin A/C Mechanotransduction in Laminopathies*. Cells, 2020. **9**(5).
67. Shin, J.Y. and Worman, H.J., *Molecular Pathology of Laminopathies.* Annu Rev Pathol, 2022. **17**: p. 159-180.
68. Pande, S. and Ghosh, D.K., *Nuclear proteostasis imbalance in laminopathy-associated premature aging diseases.* FASEB J, 2023. **37**(8): p. e23116.
69. Lityagina, O. and Dobreva, G., *The LINC Between Mechanical Forces and Chromatin.* Front Physiol, 2021. **12**: p. 710809.
70. Khilan, A.A., Al-Maslamani, N.A., and Horn, H.F., *Cell stretchers and the LINC complex in mechanotransduction.* Arch Biochem Biophys, 2021. **702**: p. 108829.
71. Sosa, B.A., et al., *LINC complexes form by binding of three KASH peptides to domain interfaces of trimeric SUN proteins.* Cell, 2012. **149**(5): p. 1035-47.
72. Gilbert, H.T.J., et al., *Nuclear decoupling is part of a rapid protein-level cellular response to high-intensity mechanical loading.* Nat Commun, 2019. **10**(1): p. 4149.
73. Omerbašić, D., et al., *ASICs and mammalian mechanoreceptor function.* Neuropharmacology, 2015. **94**: p. 80-86.
74. Chen, Y., et al., *Receptor-mediated cell mechanosensing*. Mol Biol Cell, 2017. **28**(23): p. 3134-3155.
75. Shin, J.B. and Gillespie, P.G., *Unraveling cadherin 23's role in development and mechanotransduction.* Proc Natl Acad Sci U S A, 2009. **106**(13): p. 4959-60.
76. Iliff, A.J. and Xu, X.Z.S., *A Mechanosensitive GPCR that Detects the Bloody Force.* Cell, 2018. **173**(3): p. 542-544.
77. Bloodgood, R.A., *Sensory reception is an attribute of both primary cilia and motile cilia.* J Cell Sci, 2010. **123**(Pt 4): p. 505-9.
78. Kefauver, J.M., Ward, A.B., and Patapoutian, A., *Discoveries in structure and physiology of mechanically activated ion channels.* Nature, 2020. **587**(7835): p. 567-576.
79. Coste, B., et al., *Piezo1 and Piezo2 are essential components of distinct mechanically activated cation channels*. Science, 2010. **330**(6000): p. 55-60.

80. Douguet, D., et al., *Piezo Ion Channels in Cardiovascular Mechanobiology.* Trends Pharmacol Sci, 2019. **40**(12): p. 956-970.
81. Bryniarska-Kubiak, N., Kubiak, A., and Basta-Kaim, A., *Mechanotransductive Receptor Piezo1 as a Promising Target in the Treatment of Neurological Diseases.* Curr Neuropharmacol, 2023. **21**(10): p. 2030-2035.
82. Moroni, M., et al., *Voltage gating of mechanosensitive PIEZO channels.* Nat Commun, 2018. **9**(1): p. 1096.
83. Wang, L., et al., *Mechanical sensing protein PIEZO1 regulates bone homeostasis via osteoblast-osteoclast crosstalk.* Nat Commun, 2020. **11**(1): p. 282.
84. Zhou, T., et al., *Piezo1/2 mediate mechanotransduction essential for bone formation through concerted activation of NFAT-YAP1-ß-catenin.* Elife, 2020. **9**.
85. Lukacs, L., et al., *The periodontal ligament, temperature-sensitive ion channels TRPV1-4, and the mechanosensitive ion channels Piezo1 and 2: A Nobel connection.* J Periodontal Res, 2023. **58**(4): p. 687-696.
86. Zhang, Y.Y., et al., *Cementogenesis is inhibited under a mechanical static compressive force via Piezo1.* Angle Orthod, 2017. **87**(4): p. 618-624.
87. D'Errico, J.A., et al., *Expression of bone associated markers by tooth root lining cells, in situ and in vitro.* Bone, 1997. **20**(2): p. 117-26.
88. Wang, Y., et al., *Orthodontic Compression Enhances Macrophage M2 Polarization via Histone H3 Hyperacetylation.* Int J Mol Sci, 2023. **24**(4).
89. Raices, M. and D'Angelo, M.A., *Analysis of Nuclear Pore Complex Permeability in Mammalian Cells and Isolated Nuclei Using Fluorescent Dextrans.* Methods Mol Biol, 2022. **2502**: p. 69-80.
90. Sympson, C.J. and Geoghegan, T.E., *Actin gene expression in murine erythroleukemia cells treated with cytochalasin D.* Exp Cell Res, 1990. **189**(1): p. 28-32.
91. Martinez, G., et al., *Cytochalasin D restores nuclear size acting on F-actin and IZUMO1 localization in low-quality spermatozoa.* Int J Biol Sci, 2023. **19**(7): p. 2234-2255.
92. Ramey-Ward, A.N., Su, H., and Salaita, K., *Mechanical Stimulation of Adhesion Receptors Using Light-Responsive Nanoparticle Actuators Enhances Myogenesis.* ACS Appl Mater Interfaces, 2020. **12**(32): p. 35903-35917.
93. Desideri, E., et al., *Impaired degradation of YAP1 and IL6ST by chaperone-mediated autophagy promotes proliferation and migration of normal and hepatocellular carcinoma cells.* Autophagy, 2023. **19**(1): p. 152-162.
94. Zhou, X., et al., *YAP Aggravates Inflammatory Bowel Disease by Regulating M1/M2 Macrophage Polarization and Gut Microbial Homeostasis.* Cell Rep, 2019. **27**(4): p. 1176-1189.e5.
95. Janota, C.S., Calero-Cuenca, F.J., and Gomes, E.R., *The role of the cell nucleus in mechanotransduction.* Curr Opin Cell Biol, 2020. **63**: p. 204-211.
96. Kuo, L.J. and Yang, L.X., *Gamma-H2AX - a novel biomarker for DNA double-strand breaks.* In Vivo, 2008. **22**(3): p. 305-9.
97. Huang, S.C., et al., *Metabolic Reprogramming Mediated by the mTORC2-IRF4 Signaling Axis Is Essential for Macrophage Alternative Activation.* Immunity, 2016. **45**(4): p. 817-830.

98. Satoh, T., et al., *The Jmjd3-Irf4 axis regulates M2 macrophage polarization and host responses against helminth infection.* Nat Immunol, 2010. **11**(10): p. 936-44.
99. Jia, Y., et al., *KPNA2 promotes angiogenesis by regulating STAT3 phosphorylation.* J Transl Med, 2022. **20**(1): p. 627.
100. Lai, A., et al., *Mechanosensing by Piezo1 and its implications for physiology and various pathologies.* Biol Rev Camb Philos Soc, 2022. **97**(2): p. 604-614.
101. Zhao, Q., et al., *Structure and mechanogating mechanism of the Piezo1 channel.* Nature, 2018. **554**(7693): p. 487-492.
102. Wang, S., et al., *Mechanical overloading induces GPX4-regulated chondrocyte ferroptosis in osteoarthritis via Piezo1 channel facilitated calcium influx.* J Adv Res, 2022. **41**: p. 63-75.
103. Endo, M., *Calcium ion as a second messenger with special reference to excitation-contraction coupling.* J Pharmacol Sci, 2006. **100**(5): p. 519-24.
104. Dorafshan, S., et al., *Periostin: biology and function in cancer.* Cancer Cell Int, 2022. **22**(1): p. 315.
105. Du, J. and Li, M., *Functions of Periostin in Dental Tissues and Its Role in Periodontal Tissue Regeneration.* Adv Exp Med Biol, 2019. **1132**: p. 63-72.
106. Zhu, B., et al., *LMCD1 promotes osteogenic differentiation of human bone marrow stem cells by regulating BMP signaling.* Cell Death Dis, 2019. **10**(9): p. 647.
107. Chang, C.Y., et al., *Somatic LMCD1 mutations promoted cell migration and tumor metastasis in hepatocellular carcinoma.* Oncogene, 2012. **31**(21): p. 2640-52.
108. McWhorter, F.Y., et al., *Modulation of macrophage phenotype by cell shape.* Proc Natl Acad Sci U S A, 2013. **110**(43): p. 17253-8.
109. Wosik, J., et al., *Magnetic Field Changes Macrophage Phenotype.* Biophys J, 2018. **114**(8): p. 2001-2013.
110. Stephens, A.D., et al., *Physicochemical mechanotransduction alters nuclear shape and mechanics via heterochromatin formation.* Mol Biol Cell, 2019. **30**(17): p. 2320-2330.
111. Morrison, O. and Thakur, J., *Molecular Complexes at Euchromatin, Heterochromatin and Centromeric Chromatin.* Int J Mol Sci, 2021. **22**(13).
112. Zhang, W., et al., *Aging stem cells. A Werner syndrome stem cell model unveils heterochromatin alterations as a driver of human aging.* Science, 2015. **348**(6239): p. 1160-3.
113. Olan, I., Handa, T., and Narita, M., *Beyond SAHF: An integrative view of chromatin compartmentalization during senescence.* Curr Opin Cell Biol, 2023. **83**: p. 102206.
114. Bi, S., et al., *SIRT7 antagonizes human stem cell aging as a heterochromatin stabilizer.* Protein Cell, 2020. **11**(7): p. 483-504.
115. Mohamad Kamal, N.S., et al., *Aging of the cells: Insight into cellular senescence and detection Methods.* Eur J Cell Biol, 2020. **99**(6): p. 151108.
116. Fang, X.Y., et al., *CXCL12/CXCR4 Mediates Orthodontic Root Resorption via Regulating the M1/M2 Ratio.* J Dent Res, 2022. **101**(5): p. 569-579.
117. Rath, M., et al., *Metabolism via Arginase or Nitric Oxide Synthase: Two Competing Arginine Pathways in Macrophages.* Front Immunol, 2014. **5**: p. 532.

118. Modolell, M., et al., *Reciprocal regulation of the nitric oxide synthase/arginase balance in mouse bone marrow-derived macrophages by TH1 and TH2 cytokines.* Eur J Immunol, 1995. **25**(4): p. 1101-4.
119. Muñoz, J., et al., *Macrophage Polarization and Osteoporosis: A Review.* Nutrients, 2020. **12**(10).
120. Oishi, Y. and Manabe, I., *Macrophages in inflammation, repair and regeneration.* Int Immunol, 2018. **30**(11): p. 511-528.
121. Murray, P.J. and Wynn, T.A., *Protective and pathogenic functions of macrophage subsets.* Nat Rev Immunol, 2011. **11**(11): p. 723-37.
122. Song, J., Choi, S.M., and Kim, B.C., *Adiponectin Regulates the Polarization and Function of Microglia via PPAR-γ Signaling Under Amyloid β Toxicity.* Front Cell Neurosci, 2017. **11**: p. 64.
123. Lovren, F., et al., *Adiponectin primes human monocytes into alternative anti-inflammatory M2 macrophages.* Am J Physiol Heart Circ Physiol, 2010. **299**(3): p. H656-63.
124. Mandal, P., et al., *Molecular mechanism for adiponectin-dependent M2 macrophage polarization: link between the metabolic and innate immune activity of full-length adiponectin.* J Biol Chem, 2011. **286**(15): p. 13460-9.
125. Wang, L., et al., *Adiponectin restrains ILC2 activation by AMPK-mediated feedback inhibition of IL-33 signaling.* J Exp Med, 2021. **218**(2).
126. Dikmen, K., et al., *Recombinant adiponectin inhibits inflammation processes via NF-kB pathway in acute pancreatitis.* Bratisl Lek Listy, 2018. **119**(10): p. 619-624.
127. Tannock, L.R., et al., *Serum amyloid A3 is a high density lipoprotein-associated acute-phase protein.* J Lipid Res, 2018. **59**(2): p. 339-347.
128. Kim, W.S., et al., *Apolipoprotein E inhibits osteoclast differentiation via regulation of c-Fos, NFATc1 and NF-κB.* Exp Cell Res, 2013. **319**(4): p. 436-46.
129. Lanfranco, M.F., et al., *Expression and secretion of apoE isoforms in astrocytes and microglia during inflammation.* Glia, 2021. **69**(6): p. 1478-1493.
130. Lakshmaiah, K.C., et al., *Epigenetic therapy of cancer with histone deacetylase inhibitors.* J Cancer Res Ther, 2014. **10**(3): p. 469-78.
131. Schuldt, L., et al., *Oleic acid-related anti-inflammatory effects in force-stressed PdL fibroblasts are mediated by H3 lysine acetylation associated with altered IL10 expression.* Epigenetics, 2022: p. 1-13.
132. Wang, N., et al., *The BET family in immunity and disease.* Signal Transduct Target Ther, 2021. **6**(1): p. 23.
133. Chambliss, A.B., et al., *The LINC-anchored actin cap connects the extracellular milieu to the nucleus for ultrafast mechanotransduction.* Sci Rep, 2013. **3**: p. 1087.
134. Fu, Y., et al., *Nanotube patterning reduces macrophage inflammatory response via nuclear mechanotransduction.* J Nanobiotechnology, 2023. **21**(1): p. 229.
135. Maremonti, M.I., et al., *Wide-range viscoelastic compression forces in microfluidics to probe cell-dependent nuclear structural and mechanobiological responses.* J R Soc Interface, 2022. **19**(189): p. 20210880.
136. Vivante, A., Shoval, I., and Garini, Y., *The Dynamics of Lamin a During the Cell Cycle.* Front

Mol Biosci, 2021. **8**: p. 705595.

137. Wang, Y., et al., *Postnatal development of mice with combined genetic depletions of lamin A/C, emerin and lamina-associated polypeptide 1.* Hum Mol Genet, 2019. **28**(15): p. 2486-2500.
138. Donnaloja, F., et al. *Lamin A/C Mechanotransduction in Laminopathies*. Cells, 2020. **9**, DOI: 10.3390/cells9051306.
139. Chen, L., et al., *Nucleoskeletal stiffness regulates stem cell migration and differentiation through lamin A/C.* J Cell Physiol, 2018. **233**(7): p. 5112-5118.
140. Kim, J.K., et al., *Nuclear lamin A/C harnesses the perinuclear apical actin cables to protect nuclear morphology.* Nat Commun, 2017. **8**(1): p. 2123.
141. Mitchell, M.J., et al., *Lamin A/C deficiency reduces circulating tumor cell resistance to fluid shear stress.* Am J Physiol Cell Physiol, 2015. **309**(11): p. C736-46.
142. Dasgupta, I. and McCollum, D., *Control of cellular responses to mechanical cues through YAP/TAZ regulation.* J Biol Chem, 2019. **294**(46): p. 17693-17706.
143. Elosegui-Artola, A., et al., *Force Triggers YAP Nuclear Entry by Regulating Transport across Nuclear Pores.* Cell, 2017. **171**(6): p. 1397-1410.e14.
144. Panciera, T., et al., *Mechanobiology of YAP and TAZ in physiology and disease.* Nat Rev Mol Cell Biol, 2017. **18**(12): p. 758-770.
145. Aragona, M., et al., *Mechanisms of stretch-mediated skin expansion at single-cell resolution.* Nature, 2020. **584**(7820): p. 268-273.
146. Zhou, X., et al., *Microenvironmental sensing by fibroblasts controls macrophage population size.* Proc Natl Acad Sci U S A, 2022. **119**(32): p. e2205360119.
147. Wang, S., et al., *CCM3 is a gatekeeper in focal adhesions regulating mechanotransduction and YAP/TAZ signalling.* Nat Cell Biol, 2021. **23**(7): p. 758-770.
148. Hasegawa, K., et al., *YAP signaling induces PIEZO1 to promote oral squamous cell carcinoma cell proliferation.* J Pathol, 2021. **253**(1): p. 80-93.
149. Yang, S., et al., *Emerging Roles of YAP/TAZ in Tooth and Surrounding: from Development to Regeneration.* Stem Cell Rev Rep, 2023. **19**(6): p. 1659-1675.
150. Elosegui-Artola, A., et al., *Force Triggers YAP Nuclear Entry by Regulating Transport across Nuclear Pores.* Cell, 2017. **171**(6): p. 1397-1410.e14.
151. Andreu, I., et al., *Understanding the role of mechanics in nucleocytoplasmic transport.* APL Bioeng, 2022. **6**(2): p. 020901.
152. Bell, E.S., et al., *Low lamin A levels enhance confined cell migration and metastatic capacity in breast cancer.* Oncogene, 2022. **41**(36): p. 4211-4230.
153. Kozono, T., et al., *Jaw1/LRMP has a role in maintaining nuclear shape via interaction with SUN proteins.* J Biochem, 2018. **164**(4): p. 303-311.
154. Guilluy, C., et al., *Isolated nuclei adapt to force and reveal a mechanotransduction pathway in the nucleus.* Nat Cell Biol, 2014. **16**(4): p. 376-81.
155. Liang, Y., et al., *Subcellular localization of SUN2 is regulated by lamin A and Rab5.* PLoS One, 2011. **6**(5): p. e20507.
156. Haque, F., et al., *Mammalian SUN protein interaction networks at the inner nuclear membrane and their role in laminopathy disease processes.* J Biol Chem, 2010. **285**(5): p.

3487-98.
157. Chiarini, F., et al., *Lamin A and the LINC complex act as potential tumor suppressors in Ewing Sarcoma.* Cell Death Dis, 2022. **13**(4): p. 346.
158. Mattioli, E., et al., *Prelamin A-mediated recruitment of SUN1 to the nuclear envelope directs nuclear positioning in human muscle.* Cell Death Differ, 2011. **18**(8): p. 1305-15.
159. Krshnan, L., et al., *Regulated degradation of the inner nuclear membrane protein SUN2 maintains nuclear envelope architecture and function.* eLife, 2022. **11**: p. e81573.
160. Amiad Pavlov, D., et al., *The LINC Complex Inhibits Excessive Chromatin Repression.* Cells, 2023. **12**(6).
161. Solis, A.G., et al., *Mechanosensation of cyclical force by PIEZO1 is essential for innate immunity.* Nature, 2019. **573**(7772): p. 69-74.
162. Yu, Y., et al., *Piezo1 regulates migration and invasion of breast cancer cells via modulating cell mechanobiological properties.* Acta Biochim Biophys Sin (Shanghai), 2021. **53**(1): p. 10-18.
163. Zhu, T., et al., *The mechanosensitive ion channel Piezo1 modulates the migration and immune response of microglia.* iScience, 2023. **26**(2): p. 105993.
164. Holt, J.R., et al., *Spatiotemporal dynamics of PIEZO1 localization controls keratinocyte migration during wound healing.* Elife, 2021. **10**.
165. Mukhopadhyay, A., et al., *trans-Endothelial neutrophil migration activates bactericidal function via Piezo1 mechanosensing.* Immunity, 2024. **57**(1): p. 52-67.e10.
166. Liu, C.S.C., et al., *Piezo1 mechanosensing regulates integrin-dependent chemotactic migration in human T cells.* Elife, 2024. **12**.
167. Lebon, D., et al., *PIEZO1 is essential for the survival and proliferation of acute myeloid leukemia cells.* Cancer Med, 2024. **13**(2): p. e6984.
168. He, J., et al., *Mechanical stretch promotes hypertrophic scar formation through mechanically activated cation channel Piezo1.* Cell Death Dis, 2021. **12**(3): p. 226.
169. Wan, Y., et al., *Mechanosensitive channel Piezo1 is an essential regulator in cell cycle progression of optic nerve head astrocytes.* Glia, 2023. **71**(5): p. 1233-1246.
170. Liu, Y., et al., *Mechanosensitive Piezo1 is crucial for periosteal stem cell-mediated fracture healing.* Int J Biol Sci, 2022. **18**(10): p. 3961-3980.
171. Li, M., et al., *Activation of Piezo1 contributes to matrix stiffness-induced angiogenesis in hepatocellular carcinoma.* Cancer Commun (Lond), 2022. **42**(11): p. 1162-1184.
172. Lhomme, A., et al., *Stretch-activated Piezo1 Channel in Endothelial Cells Relaxes Mouse Intrapulmonary Arteries.* Am J Respir Cell Mol Biol, 2019. **60**(6): p. 650-658.
173. Li, P.B., et al., *The mechanosensitive Piezo1 channel exacerbates myocardial ischaemia/reperfusion injury by activating caspase-8-mediated PANoptosis.* Int Immunopharmacol, 2024. **139**: p. 112664.
174. Shinge, S.A.U., et al., *Emerging Piezo1 signaling in inflammation and atherosclerosis; a potential therapeutic target.* Int J Biol Sci, 2022. **18**(3): p. 923-941.
175. Peng, Y., et al., *Type H blood vessels in bone modeling and remodeling.* Theranostics, 2020. **10**(1): p. 426-436.
176. García, J.R. and García, A.J., *Biomaterial-mediated strategies targeting vascularization for*

bone repair. Drug Deliv Transl Res, 2016. **6**(2): p. 77-95.
177. Mahapatra, C., et al., *Angiogenic stimulation strategies in bone tissue regeneration.* Tissue Cell, 2022. **79**: p. 101908.
178. Xiao, C., et al., *Association of high HIF-1α levels in serous periodontitis with external root resorption by the NFATc1 pathway.* J Mol Histol, 2020. **51**(6): p. 649-658.
179. Ullrich, N., et al., *The role of HIF-1α in nicotine-induced root and bone resorption during orthodontic tooth movement.* Eur J Orthod, 2021. **43**(5): p. 516-526.
180. Wu, Y., et al., *Response of immortalized murine cementoblast cells to hypoxia in vitro.* Arch Oral Biol, 2013. **58**(11): p. 1718-25.
181. Wang, H., et al., *PGC-1 alpha regulates mitochondrial biogenesis to ameliorate hypoxia-inhibited cementoblast mineralization.* Ann N Y Acad Sci, 2022. **1516**(1): p. 300-311.
182. Xu, L., et al., *L-arginine protects cementoblasts against hypoxia-induced apoptosis through Sirt1-enhanced autophagy.* J Periodontol, 2022. **93**(12): p. 1961-1973.
183. Li, S., et al., *The impact of Wnt signalling and hypoxia on osteogenic and cementogenic differentiation in human periodontal ligament cells.* Mol Med Rep, 2016. **14**(6): p. 4975-4982.
184. Kim, T.H., et al., *Osterix regulates tooth root formation in a site-specific manner.* J Dent Res, 2015. **94**(3): p. 430-8.
185. Feng, J.Q., Zhang, H., and Qin, C., *Letter to the Editor, "Osterix Regulates Tooth Root Formation in a Site-specific Manner".* J Dent Res, 2015. **94**(9): p. 1326.
186. Xiang, Z., et al., *Piezo1 channel exaggerates ferroptosis of nucleus pulposus cells by mediating mechanical stress-induced iron influx.* Bone Res, 2024. **12**(1): p. 20.
187. Ma, D., et al., *A novel role of periostin in postnatal tooth formation and mineralization.* J Biol Chem, 2011. **286**(6): p. 4302-9.
188. Wang, T., et al., *Aspirin targets P4HA2 through inhibiting NF-κB and LMCD1-AS1/let-7g to inhibit tumour growth and collagen deposition in hepatocellular carcinoma.* EBioMedicine, 2019. **45**: p. 168-180.
189. Ferreira, D.M.S., et al., *LIM and cysteine-rich domains 1 (LMCD1) regulates skeletal muscle hypertrophy, calcium handling, and force.* Skelet Muscle, 2019. **9**(1): p. 26.
190. Tang, Y., et al., *TGF-β1-mediated upregulation of LMCD1 drives corneal myofibroblast differentiation and corneal fibrosis.* Exp Eye Res, 2024. **249**: p. 110130.
191. Janjanam, J., et al., *LIM and cysteine-rich domains 1 is required for thrombin-induced smooth muscle cell proliferation and promotes atherogenesis.* J Biol Chem, 2018. **293**(9): p. 3088-3103.

13. Publications

May 2025	**Piezo1 Mediates Hypoxia and Mineralization in Cementoblasts.** **Wang Y**, Ruf S, Carsten S, Lei W, Groeger S. (Submitted to Journal of Dental Research)
Dec 2024	**The Dual Roles of Lamin A/C in Macrophage Mechanotransduction.** **Wang Y**, Ruf S, Wang L, Heimerl T, Bange G, Groeger S. **Cell Prolif.** doi: 10.1111/cpr.13794
Feb 2023	**Orthodontic Compression Enhances Macrophage M2 Polarization via Histone H3 Hyperacetylation.** **Wang Y**, Groeger S, Yong J, Ruf S. **Int J Mol Sci**. doi: 10.3390/ijms24043117.
Nov 2023	**Intentional replantation and dental autotransplantation of mandibular posterior teeth: Two case reports.** **Wang Y**, Hofmann M, Ruf S, Zhang J, Huang Q. **Medicine (Baltimore)**. doi: 10.1097/MD.0000000000035822.

14. Declaration

“I declare that I have completed this dissertation single-handedly without the unauthorized help of a second party and only with the assistance acknowledged therein. I have appropriately acknowledged and referenced all text passages that are derived literally from or are based on the content of published or unpublished work of others, and all information that relates to verbal communications. I have abided by the principles of good scientific conduct laid down in the charter of the Justus Liebig University of Giessen in carry out the investigations described in the dissertation.”

_____ _____

Place, Date Original Signature

Ehrenwörtliche Erklärung

„Hiermit erkläre ich, dass ich die vorliegende Arbeit selbständig und ohne unzulässigeHilfeoder Benutzung anderer als der angegebenen Hilfsmittel angefertigt habe. Alle Textstellen, die wörtlich oder sinngemäß aus veröffentlichten oder nichtveröffentlichten Schriftenentnommen sind, und alle Angaben, die auf mündlichen Auskünften beruhen, sind als solchekenntlich gemacht. Bei den von mir durchgeführten und in der Dissertation erwähntenUntersuchungen habe ich die Grundsätze guter wissenschaftlicher Praxis, wie sie inder „Satzung der Justus-Liebig-Universität Gießen zur Sicherung guter wissenschaftlicher Praxis"niedergelegt sind, eingehalten sowie ethische, datenschutzrechtliche und tierschutzrechtlicheGrundsätze befolgt. Ich versichere, dass Dritte von mir weder unmittelbar noch mittelbargeldwerte Leistungen für Arbeiten erhalten haben, die im Zusammenhang mit demInhalt dervorgelegten Dissertation stehen, und dass die vorgelegte Arbeit weder imInland nochimAusland in gleicher oder ähnlicher Form einer anderen Prüfungsbehörde zumZweckeinerPromotion oder eines anderen Prüfungsverfahrens vorgelegt wurde. Alles aus anderenQuellen und von anderen Personen übernommene Material, das in der Arbeit verwendet wurde oder auf das direkt Bezug genommen wird, wurde als solches kenntlich gemacht. Insbesondere wurden alle Personen genannt, die direkt und indirekt an der Entstehungdervorliegenden Arbeit beteiligt waren. Mit der Überprüfung meiner Arbeit durcheinePlagiatserkennungssoftware bzw. ein internetbasiertes Softwareprogrammerkläre ichmicheinverstanden."

_____ _____

Ort, Datum Unterschrift

15. Acknowledgement

I wish to express my deepest gratitude to my doctoral supervisor, **Prof. Dr. Sabine Ruf**, for her exceptional guidance, unwavering encouragement, and generous support throughout my PhD journey. Her expertise and mentorship have been instrumental to the successful completion of this research.

I am equally indebted to **PD, Dr. Sabine Groeger** and my co-supervisor, **Prof. Dr. Carsten Staszyk**, for their invaluable guidance and critical feedback. Their thoughtful advice and revisions have significantly enriched the quality of this dissertation.

My sincere thanks go to **Dr. Hernandez-Varas** and **Mrs. Kerstens** from the VIB BioImaging Core Leuven, as well as **Dr. Deckmann** and **Dr. Ai** from the Department of Anatomy at Justus-Liebig University of Giessen, for their expertise in laser confocal imaging. Their indispensable technical support greatly contributed to the imaging aspects of this research.

I also extend my gratitude to **Dr. Thomas Heimerl** and **Prof. Gert Bange** for their assistance with transmission electron microscopy, which provided critical insights into this study.

Furthermore, I would like to thank **Martin Speckmann** and **Gabriela Michel** from the Flow Cytometry Core Facility for their generous support with flow cytometry experiments and data analysis, which significantly enhanced the rigor and reliability of our results.

I am deeply thankful to my colleagues, particularly **Dr. Yuxi Zhou** and **Mr. Lei Wang**, for their collaboration, support, and encouragement during my doctoral studies.

I would also like to acknowledge the financial support provided by the **China Scholarship Council (CSC)** and **Forschungsgemeinschaft Dental e.V.**, which enabled me to dedicate myself fully to this research.

Finally, I wish to express my heartfelt appreciation to a remarkable individual from a different realm of science—the 20th-century American science fiction author, **Isaac Asimov**. The path of scientific research is long and arduous, often beset with the thorns of failure and frustration. From the shadows along the way, one may hear voices—some inviting rest, others urging retreat, and some, more insidiously, tempting us toward paths that descend into a hell shaped by the hands of the dishonest. In Asimov's writing shines the unwavering light of human reason, the determination to pursue truth, the courage to endure hardship, and a stark yet profound dissection of life's complexities. Though penned a century ago, his words pierced the veil of time to reach me in my darkest hours, offering the courage and strength to persist in the pursuit of truth.

This dissertation is the result of the collective contributions of many individuals and organizations, and I am profoundly grateful for their support.